UILU-ENG-92-2010

CIVIL ENGINEERING STUDIES

HYDRAULIC ENGINEERING SERIES NO. 42

ISSN: 0442-1744

SEDIMENT BARS IN STRAIGHT AND MEANDERING CHANNELS: EXPERIMENTAL STUDY ON THE RESONANCE PHENOMENON

By

YARKO NIÑO

and

MARCELO H. GARCIA

DEPARTMENT OF CIVIL ENGINEERING
UNIVERSITY OF ILLINOIS AT
URBANA-CHAMPAIGN
URBANA, ILLINOIS
AUGUST 1992

ABSTRACT

A study covering analytical, numerical and experimental aspects of the phenomena related to the formation and development of sediment bars in straight and meandering channels is reported. The emphasis of this research has been placed on laboratory observations with the goal of obtaining experimental evidence to verify specific aspects of recently developed analytical theories on the subject.

The analytical study consists in a revision of the linear theory for stability of alternate bars in a straight alluvial channel, with the objective of deriving relationships to estimate the conditions for the formation of alternate bars and their geometrical properties. In particular, the influence of using different resistance and bedload relationships on the results obtained through this analysis is explored.

The numerical study consists in the development of a simplified model for the two–dimensional flow and bed deformation in meandering channels, mainly with the aim of understanding the principal characteristics of the physical processes involved in this phenomenon.

The experimental study consists of a set of laboratory experiments conducted with the help of two tilting flumes that can recirculate sand–water mixtures located in the Hydrosystems Laboratory of the University of Illinois at Urbana–Champaign. These experiments involve the observation and measurement of alternate bars in straight as well as in meandering channels of different geometries. The laboratory observations are used to analyze recently developed linear and nonlinear theoretical models for the formation, geometrical properties, and migration characteristics of alternate bars. The theoretical predictions are found to be in good agreement with the observations of height, wavelength, and celerity of alternate bars. The theoretical conditions for which the suppression of migrating bars in meandering channels takes place, seem to agree qualitatively well with the experimental observations made in the laboratory.

ACKNOWLEDGMENTS

The authors wish to thank the support of the Civil Engineering Department of the University of Illinois in the form of a Research Assistantship, and the funding received from the Research Board of the University of Illinois. We also thank Mr. Nasir Gahni for his help during the experimental study. Finally the financial support provided to the first author by the Civil Engineering Department of the University of Chile and MIDEPLAN is gratefully acknowledged.

This report is based on the Master's Thesis of the first author, completed under the guidance of the second author.

TABLE OF CONTENTS

LIST OF TABLES

LIST OF FIGURES

1. INTRODUCTION

Under widely occurring circumstances flow in a straight alluvial channel with erodible bottom is unstable and various types of sediment waves may develop, depending on flow and sediment conditions. These wavy bed configurations can be classified into two categories (Kuroki and Kishi, 1985), such as: Bed Configurations of Micro–scale, characterized by ripples, dunes and antidunes, and Bed Configurations of Meso–scale, characterized by alternate bars and linguoidal bars or braids. While the former configurations have dominant influence on the hydraulic resistance to the flow, the latter have been usually related to the meandering of rivers.

The alternate bar configuration, which corresponds to the main subject of the research work reported herein, can be described as formed by migrating bedforms characterized by a sequence of steep consecutive diagonal fronts with deep pools at the downstream face and gentler riffles along the upstream face. The horizontal scale of the bedforms is typically of the order of several channel widths, while the vertical scale is of the order of the depth of flow. These alternate bars have been observed to form spontaneously under rather shallower water flows than the micro–scale configurations, even though these types of bedform may also coexist under certain flow conditions. Fig.1.1 shows a photograph of a typical bar unit, obtained in one of the laboratory experiments made as part of the present investigation, and also a schematic view of the meandering thalweg typical of this kind of bedforms.

The formation of alternate bars in straight channels has been the subject of several investigations in the last two decades (see River Meandering , Ikeda and Parker eds., 1989), for different purposes. From an engineering point of view, the zones of deposition associated with them may severely affect many aspects of river management, such as navigation, and operation of intake structures, among others. Likewise, the zones of scour interact with river banks inducing bank erosion and variation of channel alignment, and also with structures such as bridge piers, river protection works, and others, inducing the risk of failure of those structures.

From a more mechanistic point of view, alternate bars have been studied with the purpose of improving the level of understanding of river morphology. This motivation comes from the idea that alternate bars, giving rise to a sinuous migrating thalweg within the initially straight banks, might somehow evolve into meanders provided channels banks be also erodible. In other words, the formation of alternate bars would imply incipient meandering, (Tubino and Seminara, 1990). This idea, which has been supported by both laboratory (see for example Anderson et al., 1975, and Fujita and Muramoto, 1982) and field observations

(see for example Fig.1.2, in which an artificially straightened reach of Los Angeles river evolved into a meandering flow during the flood of 1938), is the basis for most of the present analytical research on the river meandering phenomenon.

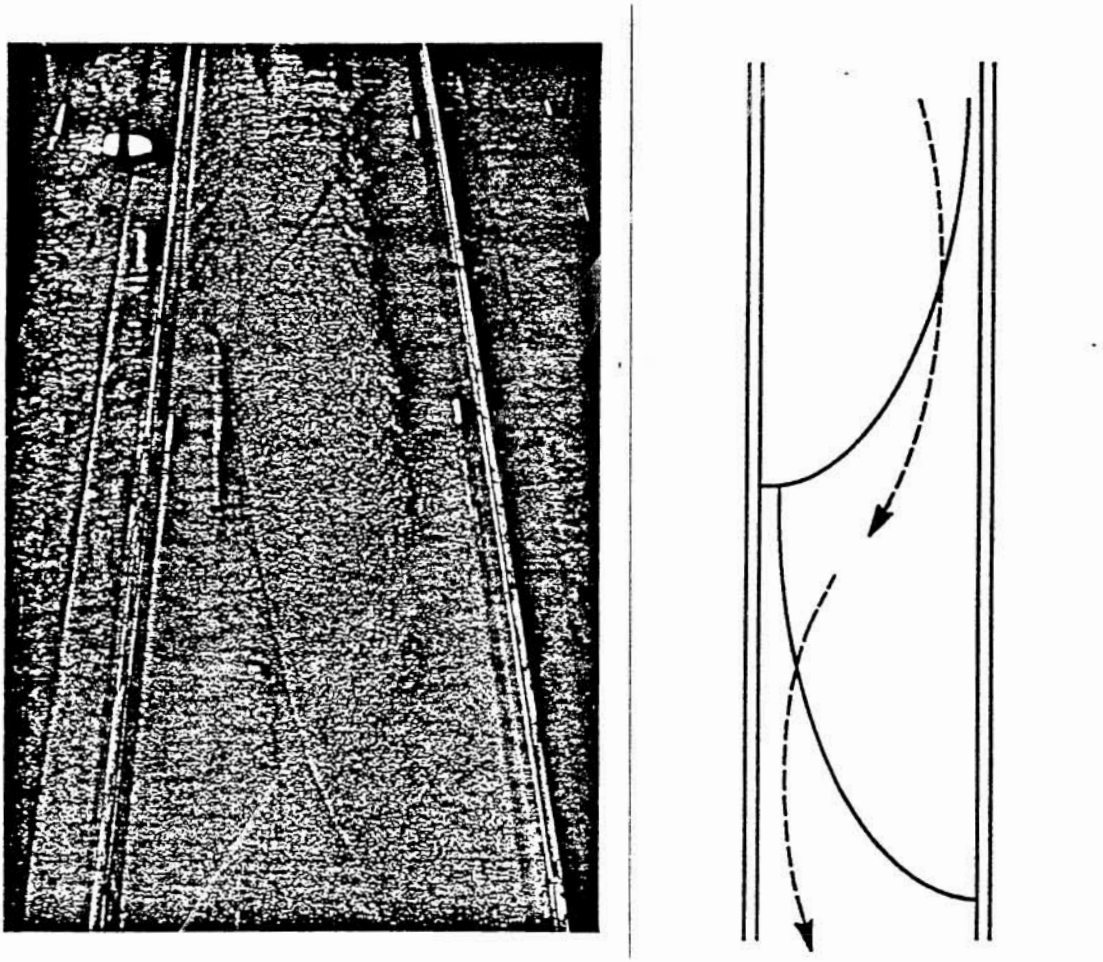

Fig.1.1 Photograph of a Bar Front and Scheme Showing the Meandering Thalweg.

Recent analytical theories developed mainly by Professor Seminara's group in Italy and Professor Parker's group at the University of Minnesota (see River Meandering, Ikeda and Parker eds., 1989), have contributed to attain a consistent level of understanding on the various phenomena involved in the initial process of meander formation. The so called 'resonance theory' of river meandering, which constitutes the basis for such understanding, was first developed by Blondeaux and Seminara (1985) and later verified by Parker and Johannesson (1989). This theory predicts that if the wavelength of an incipient meandering channel corresponds to the wavelength of a natural alternate bar mode characterized by

vanishing rate of growth and migration speed, then a resonant phenomenon occurs, in which a sharp increase in the flow and bed topography response is obtained. Under such conditions, the migrating alternate bars lock into place with the point bars formed in the channel bends, giving rise to a steady bed deformation which promotes the bank erosion process and thus the meander amplification.

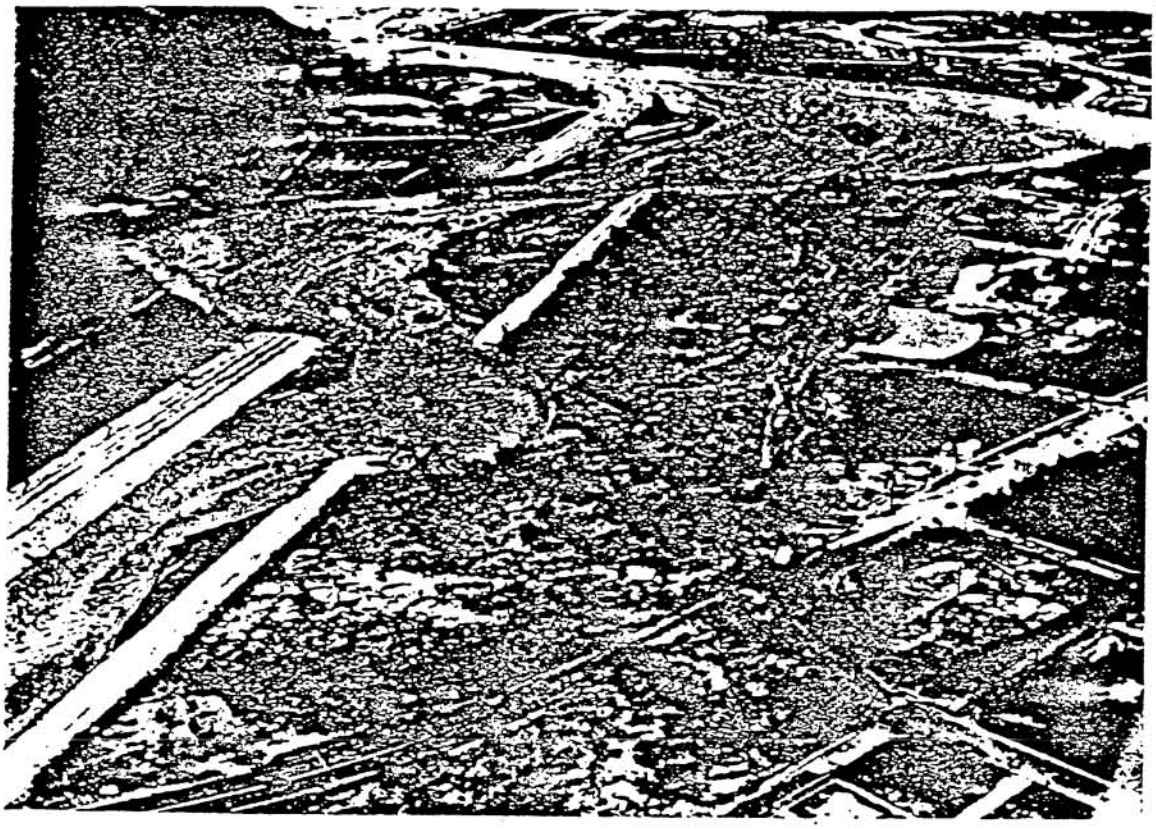

Fig.1.2 Los Angeles River in Flooding of 1938.

Even though recent attempts to verify the Resonance theory through carefully designed laboratory experiments have been successful to some extent (Colombini et al. 1990), still remain several aspects of the theory that need to be further investigated empirically. In particular, the interactions between alternate migrating bars and fixed point bars formed in channel bends and the conditions for the suppression of the former, which were studied analytically by Tubino and Seminara (1990), represent a subject that requires further

experimental research, being the study of Kinoshita and Miwa (1974) the only experimental precedent available.

According to what has been exposed above, the present investigation has been aimed at providing experimental evidence that allows for a verification of specific aspects of recently developed analytical theories on the alternate bar and meander phenomena. Given this objective, a set of laboratory experiments has been conducted with the help of two tilting flumes that can recirculate sand–water mixtures in the Hydrosystems Laboratory of the University of Illinois at Urbana–Champaign. A channel with vertical walls, having a movable bed consisting of sand of 0.5 mm of diameter, and a width of 0.4 m, was inserted inside the wider tilting flumes. Different platforms were tested ranging from a straight, 15 m long channel, to three different meandering channels having a length of approximately 25 m. Two different curvatures and two wavelengths were used for the meandering channels, which were modeled as simple sine waves. Both the influence of the channel width to depth of flow ratio and the slope on the bed deformation were investigated, and variables such as bar height, wavelength, and celerity were computed from the data collected. For the meandering channels, the location of maximum scour and the conditions for the suppression of migrating bars were also documented. The experimental conditions for the set of experiments described above were carefully selected as to match the analytical conditions under which the theories to be tested were derived, and also to cover the ranges within which the different processes to be studied experimentally should occur as predicted by those theories.

Finally, the motivation for the experimental work reported herein comes also from the perception that it is necessary not only the development of new and more sophisticated analytical theories, but also of laboratory and field evidence to truly advance the present frontier of knowledge of a such a fascinating subject as river mechanics.

2. LITERATURE REVIEW

2.1 Generalities

The most recent 'state of the art' reference on the alternate bar and river meandering phenomena corresponds to the AGU publication: River Meandering, edited by Ikeda and Parker (1989). This monograph is a collection of papers on different aspects related to the formation and development of alternate bars and river meanders, approached from mathematical, numerical and experimental points of view. Among those aspects, the one with which this research is mainly concerned is the so called 'resonance phenomenon' in meandering channels. The papers by Johannesson and Parker (1989), Parker and Johannesson (1989) and Seminara and Tubino (1989a) in that monograph, therefore, constituted the first motivation for the research work reported herein.

As it is pointed out by Seminara and Tubino (1989a), the level of understanding of the river meandering problem and related phenomena has evolved in the last two decades, from a state of a mainly descriptive empirical knowledge to the gradual development of analytical models. Theoretical attempts to give a mechanistic explanation of fluvial meandering concentrated first in the analysis of the alternate bar phenomenon. The works by Callander (1969), Hansen (1967), Hayashi (1970), Sukegawa (1971), Engelund and Skovgaard (1973), Parker (1976) and Fredsøe (1978), constitute examples of increasingly refined linear stability theories aimed at explaining the basic mechanism underlying the process of formation of the alternate bar structure, and to predict the threshold conditions for such process as well as the wavelength and speed of the unstable configurations obtained through stability analysis. The basic idea behind those theories is the recognition that under certain flow conditions, a flat bed of non-cohesive sediment may loose stability due to a spatial perturbation characterized by a growing amplitude and a downstream migration speed, whose lengthscale is of the order of several channel widths. The bed perturbations tend to form an alternating sequence of deep and shallow reaches, in which the flow develops a sinuous thalweg. Because of this pattern, the alternate bar mode of instability was interpreted as the precursor of meandering (Seminara and Tubino, 1989a).

A different approach to the meandering problem was undertaken by Ikeda, Parker and Sawai (1981), who associated the meander formation with a planimetric instability triggered by bank erosion due to secondary flow induced by channel sinuosity. The basic idea behind the so called 'bend theory', is the recognition that under certain flow conditions a flat bed of non-cohesive sediment may loose stability to a perturbed configuration of the channel axis. The analysis of Ikeda et al. (1981) led to the conclusion that the wavelength of the

meandering perturbations obtained, is close to that predicted by the 'bar theory' for the migrating alternate bar structures. This was taken as supporting the idea that the initial instability leading to the alternate bar formation would proceed into the planimetric instability leading to the meander formation. The 'bend theory' by itself, however, is not able to explain the mechanism by which relatively fast migrating alternate bars would trigger the development of the much slower process of bank erosion on which the planimetric instability depends.

Blondeaux and Seminara (1985), a few years later, unified the bar and bend theories. By analyzing the dispersion relationship of the Bar theory, they found a class of bar perturbations characterized by nearly vanishing growth rate and migration speed. This class of perturbations, however, does not correspond to a natural response of the bed in a straight channel configuration. Nevertheless, when the forcing effect of curvature of the channel axis is taken into account, it was found that the bed response corresponds exactly to the quasi–nonmigrating, quasi–nonamplifying bars, thus leading to a quasi–resonance phenomenon. The wavelengths selected by the resonance mechanism were found to be about three times larger than those predicted by the Bar theory, and in agreement with laboratory and field observations. The Resonance theory, therefore, provides the mechanism by which initially migrating bars can reduce their speed as a response to the curvature of the channel axis, in order to approach the time scale needed by the bank erosion process leading to the growth and development of meanders.

The resonance phenomenon discovered by Blondeaux and Seminara was also confirmed by Parker and Johannesson (1989), through a linear analysis which differs slightly from the previous one. Parker and Johannesson also related the resonance phenomenon to the 'overdeepening' effect discovered by Struiksma et al. (1985), according to which pronounced outside scour may be observed at the entrance of a bend contiguous to a straight reach upstream.

Even though the Resonance theory seems to provide satisfactory explanation to the meander problem, it is only valid under a number of assumptions, namely, uniform sediment, steady flow, no transport in suspension, etc., which are closer to laboratory conditions than to an actual river situation. Moreover, the linear models of Blondeaux and Seminara (1985) or Parker and Johannesson (1989), break down in the vicinity of the resonance conditions, since the expansions utilized by the models are not longer valid in that region. This limitation, as it is pointed out by Tubino and Seminara (1990), may be overcome by the development of nonlinear theories of resonance. Also, linear theories do not account for the coexistence

of migrating and fixed bars, a situation that has been observed in laboratory experiments by Gottlieb (1976) and Kinoshita and Miwa (1974).

Tubino and Seminara (1990), using a weakly nonlinear approach developed a theory that accounts for the coexistence of migrating and fixed bars, and predicts curvature and flow conditions under which the migrating, also called free, bars are suppressed, giving place to the existence of only fixed, also called forced, bars in the meandering channel. The conditions for maximum suppression of the free bars were found to coincide with the resonance conditions, and to occur for rather small values of the curvature of the channel.

More recently, Tubino (1991) developed a theory on the growth of alternate bars in unsteady flow, thus moving towards a modeling of the finite amplitude of alternate bars which is closer to the the actual river conditions than the first steady flow analysis made by Colombini, Seminara and Tubino (1987).

According to Seminara and Tubino (1989b), a consistent picture of the various phenomena involved in the initial process of meander formation in alluvial channels can be derived from the theories described above. An originally straight channel with a non–cohesive, uniform sediment bed, subject to a steady flow may undergo an instability process under proper conditions, which leads to the formation of migrating perturbations, alternate free bars, in a relatively short time scale. These bars reach a finite amplitude through a process that can be described by the theory of Colombini et al (1987). On a larger scale of time, the channel widens and undergoes a second instability process, which corresponds to the planimetric one. As the sinuosity of the channel develops the resonance phenomenon as described by Blondeaux and Seminara (1985) or Parker and Johannesson (1989) and the interactions between free and forced bars as described by Tubino and Seminara (1990), result in the suppression of the migrating perturbations, leaving only forced bars to induce bank erosion which in the end leads to the meander growth.

Even though numerous experimental studies on meandering and related phenomena have been made in the past, see for example Kinoshita (1957), Ikeda (1973), Kinoshita and Miwa (1974), Hooke (1975), Gottlieb (1976), Fujita and Muramoto (1982, 1985), etc., the validation of the theoretical findings described above through the existing experimental data is not possible since they refer to different experimental conditions and are not systematic. Colombini, Tubino and Whiting (1990) made a set of experiments carefully designed as to provide the data that would allow such validation. They built a series of meandering channels of sinusoidal shape and fixed walls, using different wavelenghts and identical maximum curvature in a range that cover the resonant conditions as predicted by the theories described above. In particular they selected a curvature large enough as to preclude the coexistence

of free and forced bars but at the same time small enough as to satisfy the conditions for which the theories were derived. Their main conclusion is that the experimental observations strongly support the idea that the resonance does not operate in the form predicted by the linear analysis. Rather than exhibiting a sharp peak within the resonant range, the bed response was found to follow a more smoothed trend, which still exhibits a maximum for values of meander wavelength which are typically smaller than those predicted by the linear theory.

The study of Colombini et al. was the first attempt to validate the Resonance theory through experiments, however, it did not cover some aspects of the theory that still remain to be further investigated in the laboratory. In particular, the phenomenon of coexistence of free and forced bars and the conditions for the suppression of the former appear to be an interesting topic, of which the only experimental precedent available in the literature corresponds to the qualitative observations made by Kinoshita and Miwa (1974).

The research work reported herein has been aimed as to provide experimental evidence to validate some aspects of the analytical models described above, specially those that have not been investigated in previous laboratory studies. Experimental conditions were selected as to cover the resonance range, as well as to allow for the coexistence of free and forced bars and the suppression of the former. The results obtained in the present investigation, therefore, should add elements that help to improve the existing theoretical models, thus improving the present level of understanding of the meander problem and related phenomena.

2.2 Bar Theory

The problem of alternate bar formation in straight alluvial channels has been the subject of numerous theoretical analyses, and can be considered as qualitatively solved after Fredsøe (1978). Nevertheless, more recent analyses like the ones by Kuroki and Kishi (1985) and Blondeaux and Seminara (1985), have improved some specific aspects of that model.

Basically, the theory consists in the use of the shallow water wave equations in two dimensions coupled with a continuity equation for the sediment. Linearizing the equations while assuming that the quasi-steady approximation is valid, and adding small double-periodic perturbations to the mean values of the flow and bed variables, a dispersion relationship is obtained, which relates the wavelength, celerity and growth rate of the perturbations, to flow and sediment parameters.

By specifying perturbations with different modes in the transverse direction a phase diagram can be obtained, which allows to separate regions in which a) no bars are present (even though ripples, dunes, antidunes, etc., can exist); b) alternate bars are present; or c)

braids and multiple rows bars are present. A diagram like this, given by Kuroki and Kishi (1985), is presented in Fig.2.1, which specifies the bed regime as a function of the dimensionless bottom shear stress, θ, the slope of the channel, S, and the ratio between channel width, $2B^*$, and depth of flow D^*.

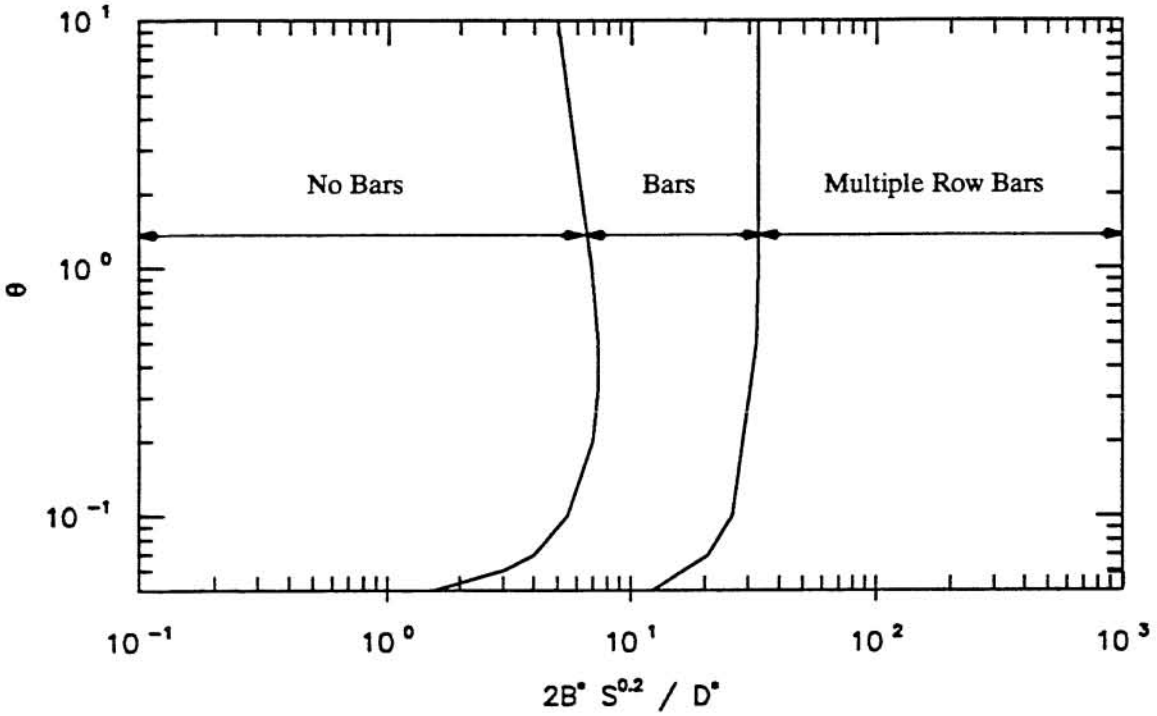

Fig. 2.1 Kuroki and Kishi's Regime Criteria for Meso-scale Configurations.

When the alternate bar mode is selected, the dispersion relationship allows to build a neutral curve as a function of the wavenumber and channel width to flow depth ratio, which corresponds to perturbations with zero rate of growth. This curve typically exhibits a minimum, which is found to correspond to critical or threshold conditions for the formation of alternate bars. For values of the wavenumber or the width to depth ratio larger than the critical ones, the rate of growth is positive, implying that any perturbation is going to grow exponentially in time. Examples of these curves can be found in Colombini et al. (1987), Parker and Johannesson (1989), Seminara and Tubino (1989), and in Fig.3.2 of the next chapter. Also, this analysis is presented in more detail in Chapter 3, exploring the effects that the use of different resistance and bed-load relationships may have over the results obtained.

One of the shortcomings of the linear theory is that it predicts an exponential growth of the unstable perturbations, therefore no finite equilibrium amplitude of the bars can be deduced from this analysis. On the other hand, it has been found experimentally that under

steady flow conditions alternate bars do eventually reach an equilibrium amplitude, which is of the order of the flow depth. Ikeda (1984), developed relationships aimed at predicting the equilibrium amplitude and also the wavelength of alternate bars, based on his own set of experimental data, as well as on an extensive number of other Japanese authors data.

Colombini et al. (1987) developed a weakly nonlinear analysis that allows to predict a finite amplitude of the alternate bars in a straight alluvial channel. This kind of analysis typically leads to the development of an amplitude equation, which as the time tends to $-\infty$ predicts an exponential growth of the amplitude, in agreement with the linear theory, but as the time tends to $+\infty$ it predicts that the amplitude tends asymptotically to an equilibrium value. The theory of Colombini et al. provides a simple equation for the equilibrium amplitude of the alternate bars as a function of a small parameter ϵ, which is defined as $\epsilon=(\beta-\beta_c)/\beta_c$ (where β is the ratio between half the channel width and the flow depth, and β_c is the critical value of β for the formation of alternate bars). The equilibrium amplitude in that equation is also a function of the bottom shear stress and the sediment size to flow depth ratio. This theoretical dependency of the bar finite amplitude on the bottom shear stress is important, because it was not taken into account by the experimental relationships of Ikeda (1984). The equilibrium amplitudes predicted by this theory are valid only for small values of the parameter ϵ, nevertheless, a comparison of these results with experimental data showed a good agreement between them, even beyond the expected limits of validity of the analysis.

2.3 Resonance

As it was pointed out before, the linear stability analysis for alternate bars provides relationships for the rate of growth and celerity of the perturbations as functions of the wavenumber and width to depth ratio, and also of the bottom shear stress and sediment size to flow depth ratio. If curves representing zero rate of growth and zero celerity of the perturbations are plotted as functions of the wave number and the parameter β defined above, two characteristic points are found. The first one corresponds to the minimum of the zero rate of growth curve, which as was explained before, is related to the critical conditions for the formation of alternate bars and also defines the value of the most probable bar wavelength selected in a straight channel configuration. This point is located in the region of positive celerity, implying that any unstable perturbation of the alternate bar type in a straight channel is going to migrate in the downstream direction. The second point corresponds to the intersection of the neutral curves, and therefore represents a perturbation of vanishing rate of growth and celerity, which being one of the possible natural responses of the flow and bed topography does not develop 'spontaneously' in a straight channel

configuration. An example of these curves is presented in Fig.3.2 in the next chapter, and can also be found in Parker and Johannesson (1989).

Blondeaux and Seminara (1985), discovered that as the forcing effect of the curvature of the channel axis is taken into account, the response of the linearized system exhibits a sharp peak for meander wavenumbers in a range of values that coincides with the range of bar wavenumbers for the quasi-nonmigrating, quasi-nonamplifying perturbations. Therefore, if the wavenumber of the meandering channel falls within the latter range, the alternate flow and bed pattern originated by curvature reinforces a natural tendency of the system for steady perturbations, which leads to a quasi-resonance phenomenon that tends to maximize bend erosion and thus meander amplification. The wavelengths of the steady 'forced' perturbations selected by the resonance mechanism were found to be on the order of three times larger than the wavelengths of the 'free' alternate bars selected by the Bar theory. A comparison of the meander wavenumbers predicted by the Resonance theory with experimental data and with values predicted for alternate bars showed that the observed wavenumbers are in better agreement with the values predicted by the Resonance theory than with those characteristic of alternate bars, which appears to support the idea that a 'bend' rather than a 'bar' mechanism prevails in the selection of the incipient meander wavelength.

Parker and Johannesson (1989), by means of a slightly different approach confirmed the Resonance theory first proposed by Blondeaux and Seminara. In particular they derived a simplified linear theory which, however, seems to retain most of the essential features exhibited by the complete theory. Parker and Johannesson proposed simple relationships that allow to predict the resonance condition given the width to depth ratio, the bottom shear stress and the sediment size to depth ratio. Figures showing these relationships are presented in the next chapter.

As it is pointed out by Blondeaux and Seminara (1985) and also by Tubino and Seminara (1990) the perturbation scheme used by the linear theories described above breaks down in the vicinity of the resonance range because the asymptotic expansions utilized to linearize the system of equations are not longer valid in that range. Colombini et al. (1990) commenting on recent findings of Professor Seminara's group in Italy, explain that a nonlinear analysis of the resonance conditions showed that within the resonance range nonlinear effects are able to smooth out the infinite peak of the linear solution and shift the maximum response, associated with maximum bend growth, towards smaller values of the meander wavelength. This seems to be confirmed by the experiments made by Colombini et al. as already mentioned.

Furthermore, the linear theories are not able to describe the coexistence of migrating free bars and fixed forced bars, which, however, has been reported as possible in laboratory experiments. The interactions between these free and forced bars appear to be responsible for some nonlinear effects that affect the bed topography in sinuous channels, and has been analyzed by means of a weakly nonlinear theory by Tubino and Seminara (1990), as discussed below.

2.4 Interactions Between Free and Forced Bars

The coexistence of migrating and fixed bars in a meandering channel has been observed in laboratory experiments by Kinoshita and Miwa (1974), Gottlieb (1976) and Fujita and Muramoto (1982). However, the most interesting of these studies from the point of view of the interactions between free and forced bars is the one conducted by Kinoshita and Miwa. These Japanese researchers made an extensive set of experiments using a 13 cm wide meandering channel covered by a mobile bed of coal with a mean diameter of 1.7 mm. The meandering channel was modeled as a set of straight segments forming an angle α to each other, such that the resulting wavelength was either equal to, or a fraction of, the free bars which had been previously found to form in a straight channel with identical flow and sediment characteristics. Two different regimes were detected depending on whether the value of α was greater or lower than a critical value α_c, which was found to be in the range of 20° to 40°, and to depend on the meander wavelength. For $\alpha < \alpha_c$, migrating alternate bars coexist with point bars formed in the channel bends. As the bars migrate downstream different states can be observed, in which the alternate bar train is in phase with, or in opposition to the meandering tendency of the channel. In particular it was observed that whenever the alternate bar train is out of phase with respect to the meandering of the channel, the meandering tendency of the flow tends to weaken and bars tend to flatten out. For $\alpha > \alpha_c$, free bars cease migrating.

The results obtained in their experiments allowed Kinoshita and Miwa to build a curve relating the critical angle α_c with the meander wavelength to channel width ratio. Such curve is presented in Fig.2.2. Kinoshita and Miwa explained their results from a rather geometrical point of view, stating that for the suppression of migrating bars it is necessary for the channel curvature to be large enough so as to allow the thread of highest flow velocity, which corresponds also to the zone of highest sediment transport, to strike the opposite bank before another change of direction of the channel axis. It is also necessary the presence of subsequent changes of direction, one for each bar, in order that every bar in the channel is subjected to a similar stabilizing influence that promotes the stability of the entire train.

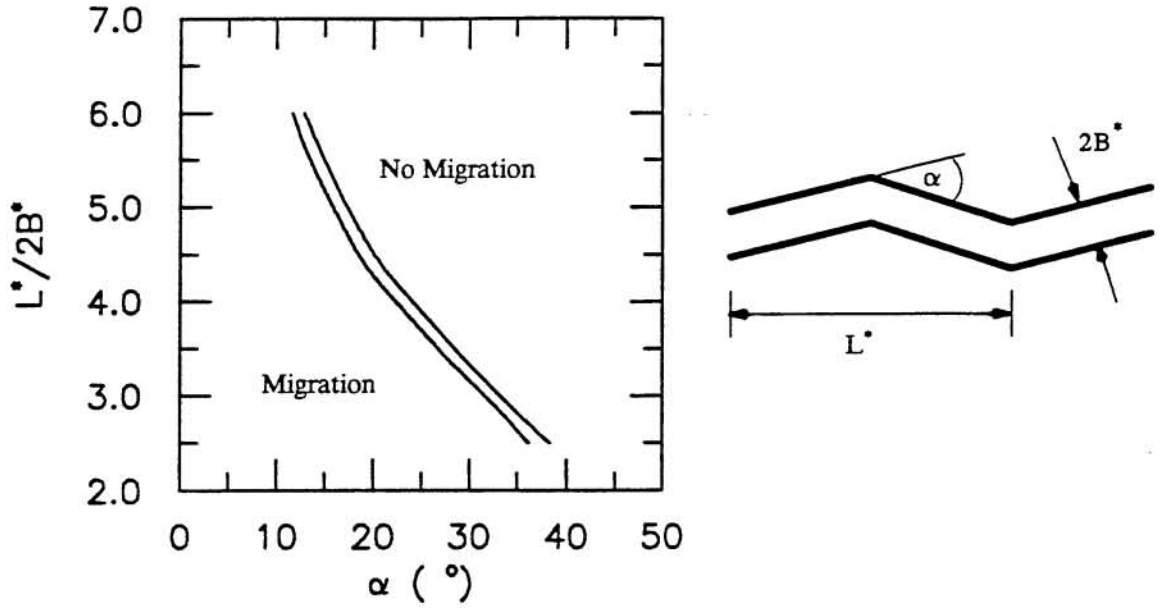

Fig. 2.2 Kinoshita and Miwa's Critical Meander Angle for the Suppression of Migrating Bars.

Tubino and Seminara (1990), interpreted Kinoshita and Miwa's results from a different point of view. For them, those results suggest that it is the interaction between the migrating free and steady forced bars which is responsible for the suppression of the former perturbations, and furthermore, for suppression to occur, the amplitude of forced bars, which increases with α, must exceed a threshold value dependent on the meander wavelength. According to these authors a theoretical interpretation of this process requires a finite amplitude representation not only of free bars, which was already obtained by Colombini et al. (1987) as a function of the small parameter ϵ defined before, but also of forced bars, which should be expressed in terms of some small parameter ν measuring curvature effects.

Tubino and Seminara (1990), developed a weakly–nonlinear theory to analyze the interactions between free and forced bars. In particular they derived an amplitude equation which allow to identify different regimes for the equilibrium solution of the free and forced perturbations. Two critical values of the small parameter ν, defined as the ratio between half the channel width and twice the minimum radius of curvature of the channel (or half the maximum curvature), were found : ν_{c1} and ν_{c2}. The following regimes appear to be possible: i) If $\nu_{c1} < \nu_{c2}$, free bars are damped and slowed down for $\nu < \nu_{c1}$, and are suppressed for $\nu > \nu_{c1}$.. ii) If $\nu_{c1} > \nu_{c2}$, free bars are damped and slowed down but migrate downstream for $\nu < \nu_{c2}$, are damped and migrate upstream (though possibly at a very low rate) for $\nu_{c2} < \nu < \nu_{c1}$, and are suppressed for $\nu > \nu_{c1}$. According to these criteria, suppression of migrating bars can be

expected in a meandering channel provided its curvature ν is greater than the critical value ν_{c1}. The theory provides a simply expression for ν_{c1}, as a function of the small parameter ϵ defined before: $\nu_{c1} = k_{c1}\, \epsilon^{1/2} = k_{c1}\, ((\beta-\beta_c)/\beta_c)^{1/2}$, where the parameter k_{c1} is a function of the ratio between the meander wavelength and the critical wavelength of the alternate bars as obtained from the neutral curve, the bottom shear stress, and the sediment size to flow depth ratio, and can be obtained from Fig.9 in Tubino and Seminara's paper. The dependence of ν_{c1} on β as predicted by the above formula is fairly strong but could not be detected by Kinoshita and Miwa who designed their experiments so that β was held constant. No simple expression is provided for ν_{c2}.

According to the results obtained by Tubino and Seminara, the minimum conditions for the suppression of migrating bars are attained within the resonant wavenumber range of Blondeaux and Seminara (1985), which is not unexpected, since close to resonance the forced bar exhibits a peak which implies that lower sinuosities are sufficient to damp free bars. A comparison of these results with Kinoshita and Miwa's observations, showed a favorable agreement, which was taken as a confirmation of the physical ideas underlying the theory.

3. LINEAR ANALYSIS OF STABILITY PROBLEM

3.1 Introduction

In what follows a revision of the linear theory for stability of alternate bars in a straight alluvial channel as derived by Blondeaux and Seminara (1985) and Colombini et al. (1987) is made. The critical or threshold conditions for the formation of alternate bars are derived in terms of the wavelength, channel width to depth of flow ratio, and celerity of the unstable perturbations. The behavior of the critical values of such variables is obtained as a function of the bottom shear stress and the sediment size to depth of flow ratio. In particular, the influence of using different resistance and bedload relationships on the results obtained through this analysis is explored.

Likewise, the analysis is extended as to obtain graphical relationships for the resonant conditions as described in the preceding chapter. A comparison of this conditions with the predictive relationships derived by Parker and Johannesson (1989) is also made.

3.2 Linear Stability Theory

The following derivation is adapted from the papers by Blondeaux and Seminara (1985) and Colombini et al. (1987). Their analysis is extended with the aim of exploring the effects that the use of different resistance and bedload relationships has on the results obtained.

The flow in a straight alluvial channel having a constant width $2B^*$ and non-erodible banks covered by a non-cohesive sediment bed is considered. The width of the channel is taken as large enough for the flow to be modelled as two-dimensional. Therefore, the flow is described everywhere except for the layers adjacent to the walls where vertical velocities cannot be neglected. Even though only depth-averaged values of the transverse velocity are considered, account is taken of the influence that the secondary flow has on sediment transport. Fig. 3.1 shows a sketch of the channel under consideration in which variables utilized in the analysis presented below are defined. In that figure, a bed deformation of the alternate bar type is assumed and the wavelength L^* of the bedform is also defined.

The analysis of Colombini et al. utilizes the St. Venant equations for shallow water flow in a straight channel, assuming the quasi-steady approximation to be valid for a slowly varying erodible bottom, coupled with the Exner equation for continuity of sediment, assuming only bedload mode of sediment transport. These equations are written in the following dimensionless form.

$$V\frac{\partial U}{\partial n} + U\frac{\partial U}{\partial s} = -\frac{\partial H}{\partial s} - \frac{\beta\,\tau_s}{D} \qquad (3.1a)$$

$$V\frac{\partial V}{\partial n} + U\frac{\partial V}{\partial s} = -\frac{\partial H}{\partial n} - \frac{\beta\,\tau_n}{D} \qquad (3.1b)$$

$$\frac{\partial(V\,D)}{\partial n} + \frac{\partial(U\,D)}{\partial s} = 0 \qquad (3.1c)$$

$$\frac{\partial(F_0^2\,H - D)}{\partial t} + Q_0\left[\frac{\partial Q_n}{\partial n} + \frac{\partial Q_s}{\partial s}\right] = 0 \qquad (3.1d)$$

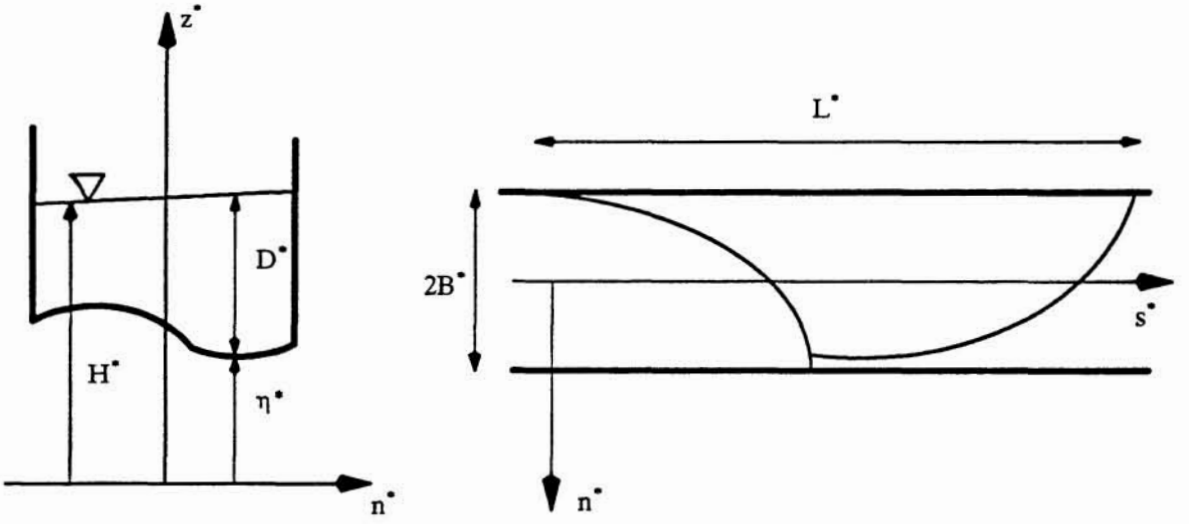

Fig.3.1 Sketch of the Channel and Definition of Variables.

In (3.1), (U,V) are the dimensionless depth–averaged velocity components in the axial and transverse directions, respectively, τ_s and τ_n are the dimensionless bottom shear stresses, H is the dimensionless water surface elevation, D is the dimensionless local depth, Q_s and Q_n are the dimensionless volumetric sediment flow rate per unit width components in the axial and transverse directions, respectively, and F_0 is the unperturbed Froude number of the flow. Also, Q_0 is the ratio between the scale of sediment discharge and the flow rate and β is the channel width to depth of flow ratio, given by:

$$Q_0 = \frac{d_s^*\,[\,(\varrho_s/\varrho - 1)\,g\,d_s^*\,]^{\frac{1}{2}}}{(1-p)\,D_0^*\,U_0^*} \quad , \quad \beta = \frac{B^*}{D_0^*} \qquad (3.2a, b)$$

where ρ_s and d_s^* are the density and diameter of the uniform sediment, ρ is the water density, g is the gravitational acceleration, and p denotes sediment porosity. Likewise, U_0^* and D_0^*

are average velocity and depth for the uniform unperturbed flow, respectively. In (3.1) the variables have been made dimensionless in the form:

$$(U^*, V^*) = U_0^* (U, V) \quad , \quad (H^*, D^*) = D_0^* (F_0^2 H, D) \qquad (3.3a, b)$$

$$(s^*, n^*) = B^* (s, n) \quad , \quad (\tau_s^*, \tau_n^*) = \varrho U_0^{*2} (\tau_s, \tau_n) \qquad (3.3c, d)$$

$$(Q_s^*, Q_n^*) = d_s^* [(\varrho_s/\varrho - 1) g d_s^*]^{\frac{1}{2}} (Q_s, Q_n) \quad , \quad t^* = \frac{B^*}{U_0^*} t \qquad (3.3e, f)$$

In order to close the system of equations formed by (3.1), both resistance and sediment transport relationships are needed. Let express the bottom shear stress vector T in terms of a friction coefficient C defined by the relationship:

$$T = (\tau_s , \tau_n) = (U, V) (U^2 + V^2)^{\frac{1}{2}} C \qquad (3.4)$$

The dependence of C on flow parameters is not known for general flow conditions as those defined by alternate bars, however, since the flow to be studied is only slightly perturbed from the case of steady flow in straight channels, the friction coefficient C is evaluated using the Engelund–Hansen resistance equation, for the appropriate bed regime, as follows:

Flat Bed :

$$C^{-\frac{1}{2}} = 6 + 2.5 \ln (\frac{D}{2.5 d_s}) \qquad (3.5a)$$

Dune–covered Bed :

$$(\frac{\theta}{\theta' C})^{\frac{1}{2}} = 6 + 2.5 \ln (\frac{\theta' D}{2.5 \theta d_s}) \qquad (3.5b)$$

$$\theta' = 0.06 + 0.4 \theta^2 \quad , \quad \theta = \frac{\tau_0^*}{(\varrho_s - \varrho) g d_s^*} \qquad (3.5c)$$

In (3.5), θ is the Shields parameter defined in terms of the unperturbed bottom shear stress τ_0^* and θ' is the fraction of θ associated with grain resistance. Also, d_s is a dimensionless sediment diameter defined as $d_s = d_s^* / D_0^*$.

The sediment transport is assumed to be mainly in the bedload mode. Special attention is paid to the modeling of the effect that the secondary flow and transverse bed slope exert on the direction and intensity of the bedload motion. The model of Parker (1984) based on previous work by Engelund (1981), is used, for which:

$$Q = (Q_s , Q_n) = (\cos\delta , \sin\delta) \Phi \qquad (3.6a)$$

$$\sin\delta = V (U^2 + V^2)^{-\frac{1}{2}} - \frac{r}{\beta \theta^{\frac{1}{2}}} \frac{\partial (F_0^2 - D)}{\partial n} \qquad (3.6b)$$

where, Φ corresponds to a function describing the bedload transport in the unperturbed uniform flow and δ denotes the angle between the particle velocity and the axial direction.

Also, the value of the parameter r in (3.6b) is taken as 0.3 following the arguments given by Colombini et al.

Two different bedload relationships are used to evaluate Φ, namely, Meyer–Peter and Muller and Engelund–Hansen formulas.

Meyer-Peter and Muller :
$$\Phi = 8 \, (\, \theta - \theta_{cr} \,)^{\frac{3}{2}} \quad , \quad \theta_{cr} = 0.047 \tag{3.7a}$$

Engelund–Hansen :
$$\Phi = \frac{0.05}{C} \, \theta^{\frac{5}{2}} \tag{3.7b}$$

The linear theory analyzes the conditions under which the unperturbed uniform flow loses stability to small double periodic perturbations, in the s and n directions. The following linearization of flow parameters is performed, where A represents a small parameter.

$$(U , V , D , H) = (1 , 0 , 1 , H_0) + A \, (U_1 , V_1 , D_1 , H_1) \tag{3.8a}$$

$$(\tau_s , \tau_n , Q_s , Q_n) = (C_0 , 0 , \Phi_0 , 0) + A \, (\tau_{s1} , \tau_{n1} , Q_{s1} , Q_{n1}) \tag{3.8b}$$

In (3.8), C_0 and Φ_0 denote the friction coefficient and bedload transport of the unperturbed uniform flow, respectively. By substituting (3.8) into the system of equations (3.1) and performing a linearization, the following homogeneous differential problem is obtained,

$$\frac{\partial U_1}{\partial s} + \frac{\partial H_1}{\partial s} + \beta \, (\, \tau_{s1} - D_1 \, C_0 \,) = 0 \tag{3.9a}$$

$$\frac{\partial V_1}{\partial s} + \frac{\partial H_1}{\partial n} + \beta \, \tau_{n1} = 0 \tag{3.9b}$$

$$\frac{\partial U_1}{\partial s} + \frac{\partial V_1}{\partial n} + \frac{\partial D_1}{\partial s} = 0 \tag{3.9c}$$

$$F_0^2 \, \frac{\partial H_1}{\partial t} - \frac{\partial D_1}{\partial t} + Q_0 \, [\, \frac{\partial Q_{n1}}{\partial n} + \frac{\partial Q_{s1}}{\partial s} \,] = 0 \tag{3.9d}$$

where, τ_{s1}, τ_{n1}, Q_{s1} and Q_{n1} are expressed in the form:

$$\tau_{s1} = C_0 \, (\, s_1 \, U_1 + s_2 \, D_1 \,) \quad , \quad \tau_{n1} = C_0 \, V_1 \tag{3.10a}$$

$$Q_{s1} = \Phi_0 \, (\, f_1 \, U_1 + f_2 \, D_1 \,) \quad , \quad Q_{n1} = \Phi_0 \, (\, V_1 - R \, (\, F_0^2 \, \frac{\partial H_1}{\partial n} - \frac{\partial D_1}{\partial n} \,)) \tag{3.10b}$$

with,

$$s_1 = 2 \, (\, 1 - c_T \,)^{-1} \quad , \quad s_2 = c_D \, (\, 1 - c_T \,)^{-1} \tag{3.11a}$$

$$f_1 = 2 \, \Phi_T \, (\, 1 - c_T \,)^{-1} \quad , \quad f_2 = \Phi_D + c_D \, \Phi_T \, (\, 1 - c_T \,)^{-1} \quad , \quad R = \frac{r}{\beta \, \theta_0^{\frac{1}{2}}} \tag{3.11b}$$

In (3.11), θ_0 is the Shields parameter of the unperturbed uniform flow, and c_T, c_D, Φ_T and Φ_D are defined as:

$$c_D = \frac{1}{C_0}\frac{\partial C}{\partial D}\bigg|_{D_0} \quad , \quad c_T = \frac{\theta_0}{C_0}\frac{\partial C}{\partial \theta}\bigg|_{\theta_0} \quad , \quad \Phi_D = \frac{1}{\Phi_0}\frac{\partial \Phi}{\partial D}\bigg|_{D_0} \quad , \quad \Phi_T = \frac{\theta_0}{\Phi_0}\frac{\partial \Phi}{\partial \theta}\bigg|_{\theta_0} \qquad (3.12)$$

and can be evaluated from the relationships (3.5) and (3.7).

Now, the perturbed quantities are assumed to be represented in wave form by a double periodic translating sine function of exponentially variable amplitude. The wavelength of the perturbation in the transverse direction is assumed to correspond to twice the channel width, thus selecting perturbations of the alternate bar type. Note that selecting smaller wavelengths in the transverse direction, perturbations of the multiple row bar type can be analyzed in the same fashion. The perturbation can be written as:

$$(U_1, D_1, H_1, V_1) = \exp (\Omega t) (S(n) u_1 , S(n) d_1 , S(n) h_1 , C(n) v_1) E(s,t) + c.c \qquad (3.13)$$

where, c.c denotes complex conjugate, and Ω the growth rate of the perturbation. S(n), C(n) and E(s,t) are defined in the following form:

$$S(n) = \sin (\frac{1}{2} \pi n) \quad , \quad C(n) = \cos (\frac{1}{2} \pi n) \qquad (3.14a, b)$$

$$E(s,t) = \exp (i (\lambda s - \omega t)) \qquad (3.14c)$$

where λ and ω are the wavenumber in the axial direction and angular frequency of the perturbations respectively. Substituting (3.13) and (3.14) into (3.9) and (3.10), the following linear homogeneous algebraic system is obtained:

$$a_{i1} u_1 + a_{i2} v_1 + a_{i3} h_1 + a_{i4} d_1 = 0 \quad , \quad (i = 1,2,3,4) \qquad (3.15)$$

with,

$$a_{11} = (i \lambda + \beta C_0 s_1) \quad , \quad a_{12} = 0 \quad , \quad a_{13} = i \lambda \quad , \quad a_{14} = \beta C_0 (s_2 - 1) \qquad (3.16a)$$

$$a_{21} = 0 \quad , \quad a_{22} = i \lambda + \beta C_0 \quad , \quad a_{23} = \frac{\pi}{2} \quad , \quad a_{24} = 0 \qquad (3.16b)$$

$$a_{31} = i \lambda \quad , \quad a_{32} = -\frac{\pi}{2} \quad , \quad a_{33} = 0 \quad , \quad a_{34} = i \lambda \qquad (3.16c)$$

$$a_{41} = i \lambda Q_0 \Phi_0 f_1 \quad , \quad a_{42} = - Q_0 \Phi_0 \frac{\pi}{2} \quad , \quad a_{43} = F_0^2 (Q_0 \Phi_0 \frac{\pi^2}{4} R + \Omega - i \omega) \qquad (3.16d)$$

$$a_{44} = Q_0 \Phi_0 (i \lambda f_2 - \frac{\pi^2}{4} R) - \Omega + i \omega \qquad (3.16e)$$

The homogeneous algebraic system (3.15) has a non trivial solution only if the determinant of the matrix formed by the coefficients a_{ij} is zero. This condition defines the following dispersion relationship:

$$\frac{(\Omega - i\,\omega)}{Q_0\,\Phi_0} = -\frac{A_1\,\lambda^4 + i\,A_2\,\lambda^3 + A_3\,\lambda^2 + i\,A_4\,\lambda + A_5}{B_0 + i\,B_1\,\lambda + B_2\,\lambda^2 + i\,B_3\,\lambda^3} \qquad (3.17)$$

where,

$$A_1 = (f_1 - f_2) \quad , \quad A_2 = \frac{\pi^2}{4}\frac{R'}{\beta}(F_0^2 - 1) + (f_2 - f_1)\,C_0\,\beta \qquad (3.18a, b)$$

$$A_3 = \frac{\pi^2}{4}(1 - f_2 - C_0\,R' - F_0^2\,C_0\,R'\,(s_2 - s_1 - 2)) \qquad (3.18c)$$

$$A_4 = \frac{\pi^2}{4}((F_0^2\,C_0^2\,R' + C_0)(s_2 - s_1 - 1)\,\beta - \frac{\pi^2}{4}\frac{R'}{\beta} - C_0\,(f_1\,(s_2 - 1) - s_1\,f_2)\,\beta) \qquad (3.18d)$$

$$A_5 = -\left(\frac{\pi^2}{4}\right)^2 C_0\,s_1\,R' \qquad (3.18e)$$

and

$$B_0 = -\frac{\pi^2}{4}\,C_0\,s_1\,\beta \quad , \quad B_1 = F_0^2\,C_0^2\,(s_2 - s_1 - 1)\,\beta^2 - \frac{\pi^2}{4} \qquad (3.19a, b)$$

$$B_2 = C_0\,\beta\,(F_0^2\,(s_1 - s_2 + 2) - 1) \quad , \quad B_3 = (F_0^2 - 1) \qquad (3.19c, d)$$

with

$$R' = \frac{r}{\theta_0^{\frac{1}{2}}}$$

From (3.17) relationships expressing the growth rate and angular frequency of the perturbations are obtained as follows:

$$\Omega = -Q_0\,\Phi_0\,\frac{(A_1\,\lambda^4 + A_3\,\lambda^2 + A_5)(B_0 + B_2\,\lambda^2) + (A_2\,\lambda^3 + A_4\,\lambda)(B_1\,\lambda + B_3\,\lambda^3)}{(B_0 + B_2\,\lambda^2)^2 + (B_1\,\lambda + B_3\,\lambda^3)^2} \qquad (3.20)$$

$$\omega = Q_0\,\Phi_0\,\frac{(A_2\,\lambda^3 + A_4\,\lambda)(B_0 + B_2\,\lambda^2) - (A_1\,\lambda^4 + A_3\,\lambda^2 + A_5)(B_1\,\lambda + B_3\,\lambda^3)}{(B_0 + B_2\,\lambda^2)^2 + (B_1\,\lambda + B_3\,\lambda^3)^2} \qquad (3.21)$$

It can be concluded from the preceding set of equations, that Ω and ω depend only on four parameters, namely, λ, β, θ_0 and d_s, since s_1, s_2, f_1, f_2, F_0, C_0, Φ_0 and Q_0 are functions of θ_0 and d_s only. Therefore, given fixed values of θ_0 and d_s, (3.20) and (3.21) define parametric relationships for β as a function of λ, depending on the values of Ω and ω. In particular, by setting $\Omega = 0$ and $\omega = 0$ in those equations, two different neutral curves are obtained in the plane (λ, β), for which the growth rate and angular frequency of the perturbations vanish.

An example of those neutral curves is presented in Fig. 3.2, for the following conditions: $\theta_0 = 0.3$; $d_s = 0.01$; Meyer–Peter and Muller bedload relationship (3.7a), and the

flat bed Engelund–Hansen resistance equation (3.5a). This corresponds to the same example presented by Colombini et al. (1987) and also by Parker and Johannesson (1989). In that figure, any point located inside the growth rate neutral curve ($\Omega = 0$) has a positive rate of growth and therefore corresponds to an unstable perturbation. Likewise, any point located to the right of the angular frequency neutral curve ($\omega = 0$) has a positive angular frequency and therefore corresponds to a perturbation that migrates in the downstream direction.

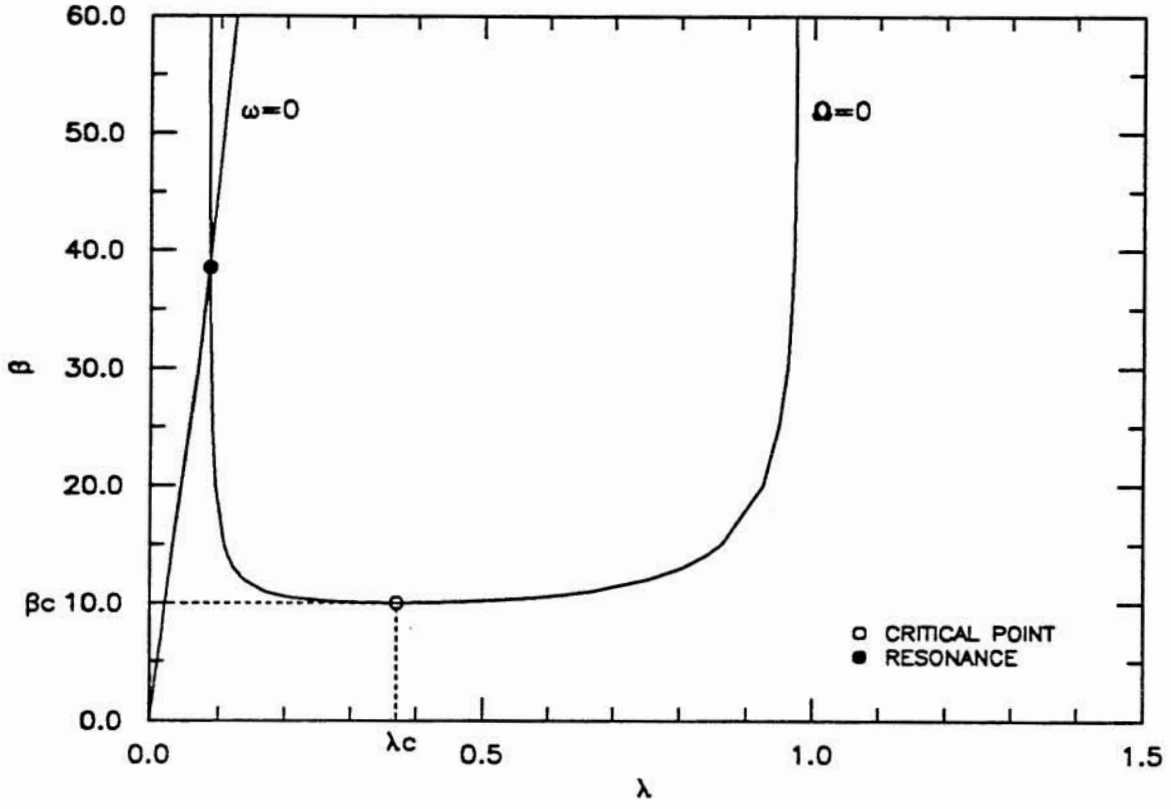

Fig.3.2 Neutral Curves for Alternate Bars–Linear Theory ($\theta_0 = 0.3$; $d_s = 0.01$).

Also, in Fig. 3.2 two characteristic points are distinguished. The first one corresponds to the minimum of the growth rate neutral curve, which as was discussed in the preceding chapter defines the critical or threshold conditions for the formation of alternate bars. The second point corresponds to the intersection of both neutral curves, defining a perturbation of vanishing rate of growth and angular frequency, which as was also discussed in Chapter 2, corresponds to perturbations of the resonant type, provided the channel is a meandering channel of the adequate wavelength. This last characteristic point is not a possible response of the system if the channel is straight, therefore incipient perturbations of the alternate bar

type have always a positive angular frequency, or in other words, they migrate in the downstream direction.

In what follows, graphical relationships are derived relating the values of λ, β and ω of incipient alternate bars at the critical point, as functions of θ_0 and d_s.

3.3 Critical Conditions for the Formation of Alternate Bars

By setting $\Omega = 0$ in (3.20), the following equation is obtained, which for fixed values of θ_0 and d_s allows to compute the growth-rate neutral curve in the plane (λ, β).

$$a_3 \lambda^6 + a_2 \lambda^4 + a_1 \lambda^2 + a_0 = 0 \qquad (3.22)$$

where,

$$a_0 = A_5 B_0 \quad , \quad a_1 = A_3 B_0 + A_5 B_2 + A_4 B_1 \qquad (3.23a, b)$$

$$a_2 = A_1 B_0 + A_3 B_2 + A_2 B_1 + A_4 B_3 \quad , \quad a_3 = A_1 B_2 + A_2 B_3 \qquad (3.23c, d)$$

This neutral curve has a minimum, as can be observed in the example of Fig. 3.2, which defines the critical values λ_c and β_c for incipient alternate bars. By substituting λ_c and β_c in (3.21) the corresponding value ω_c is obtained, which as λ_c and β_c depends not only on the values of θ_c and d_s, but also on the bedload and resistance equations selected. Three different combinations of the equations (3.5) and (3.7) are used in what follows with the aim of analyzing the effect of different resistance and bedload equations on the threshold conditions for the formation of alternate bars.

By combining the Meyer-Peter and Muller bedload equation (3.7a) with the flat-bed Engelund-Hansen resistance relationship (3.5a), the following expressions for the parameters s_1, s_2, f_1 and f_2 are obtained:

$$s_1 = 2 \quad , \quad s_2 = -5\, C_0^{\frac{1}{2}} \quad , \quad f_1 = \frac{3\,\theta_0}{\theta_0 - \theta_{cr}} \quad , \quad f_2 = -7.5\, \frac{C_0^{\frac{1}{2}}\,\theta_0}{\theta_0 - \theta_{cr}} \qquad (3.24a\text{-}d)$$

With these relationships, the values of β_c and λ_c are computed from (3.22) as functions of θ_0 and d_s, using the definitions (3.18), (3.19) and (3.23). The results obtained are presented in Figs. 3.3 and 3.4, respectively.

By combining the Engelund-Hansen bedload equation (3.7b) with the flat-bed Engelund-Hansen resistance relationship (3.5a), s_1, s_2, f_1 and f_2 can be expressed as:

$$s_1 = 2 \quad , \quad s_2 = -5\, C_0^{\frac{1}{2}} \quad , \quad f_1 = 5 \quad , \quad f_2 = -7.5\, C_0^{\frac{1}{2}} \qquad (3.25a\text{-}d)$$

As before, with these expressions the values of β_c and λ_c are computed from (3.22) as functions of θ_0 and d_s, using the definitions (3.18), (3.19) and (3.23). The results obtained are presented in Figs. 3.5 and 3.6, respectively.

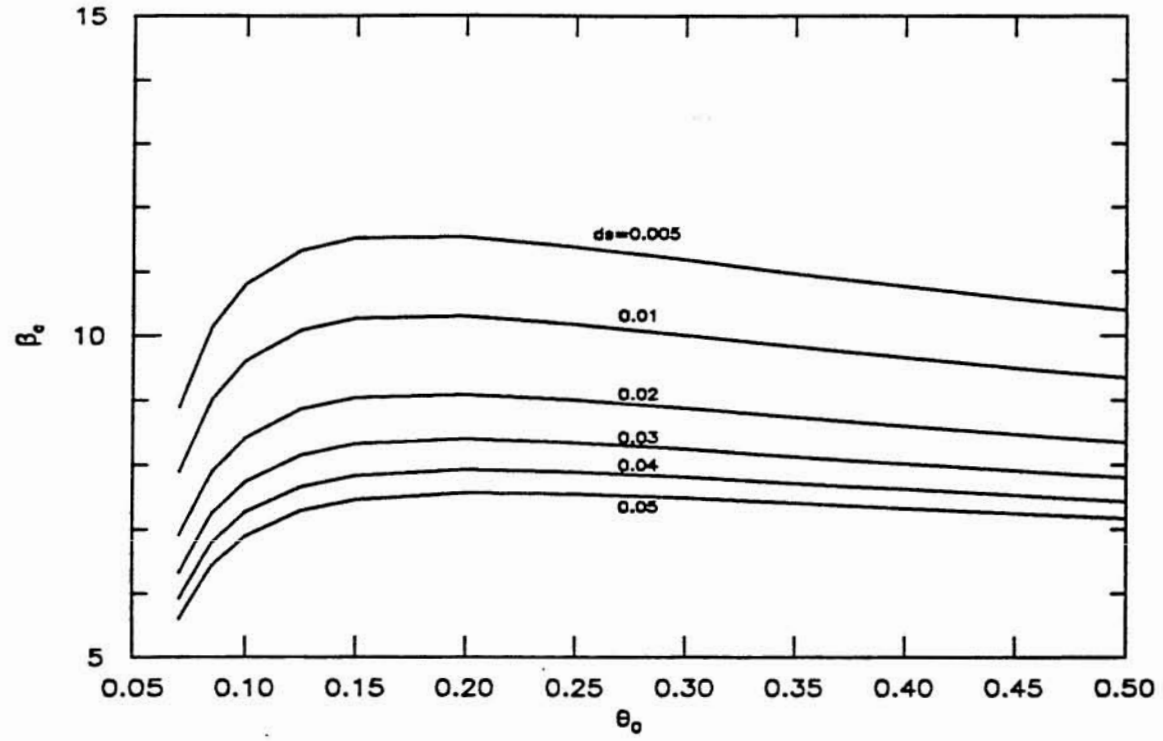

Fig.3.3 β_c as a function of θ_0 and d_s. Linear Theory. Meyer-Peter and Muller Bedload Relationship; Flat-bed Engelund-Hansen Resistance Equation.

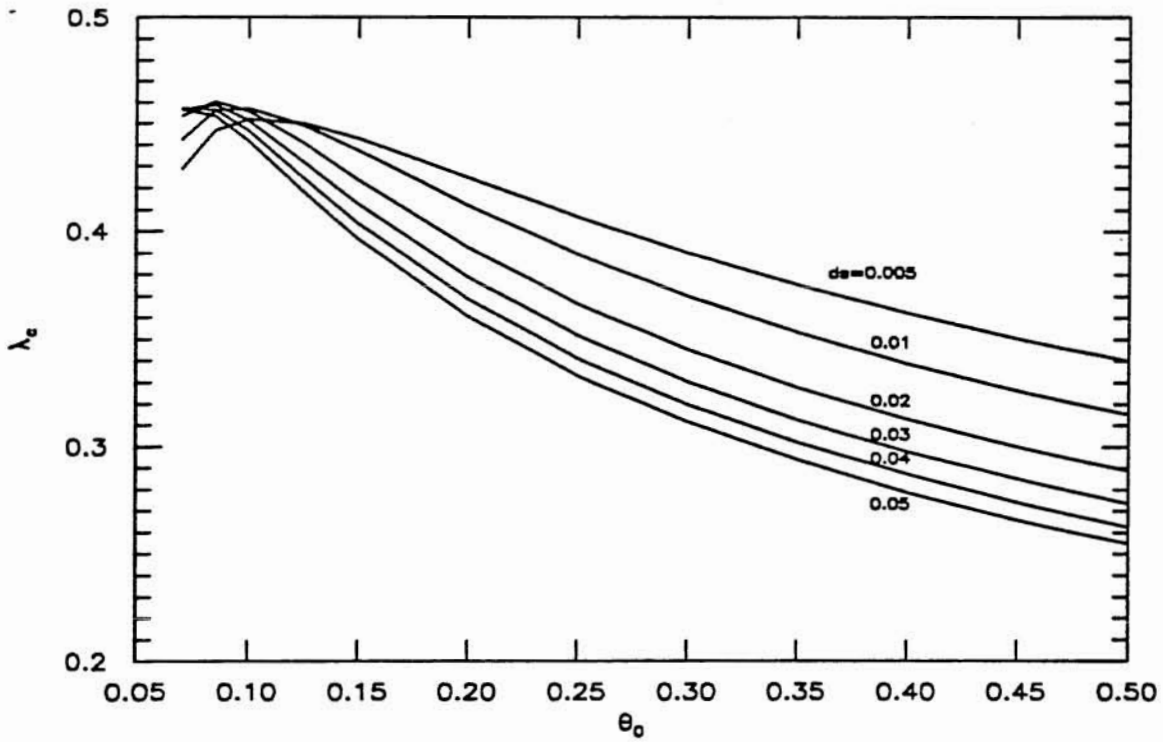

Fig.3.4 λ_c as a function of θ_0 and d_s. Linear Theory. Meyer-Peter and Muller Bedload Relationship; Flat-bed Engelund-Hansen Resistance Equation.

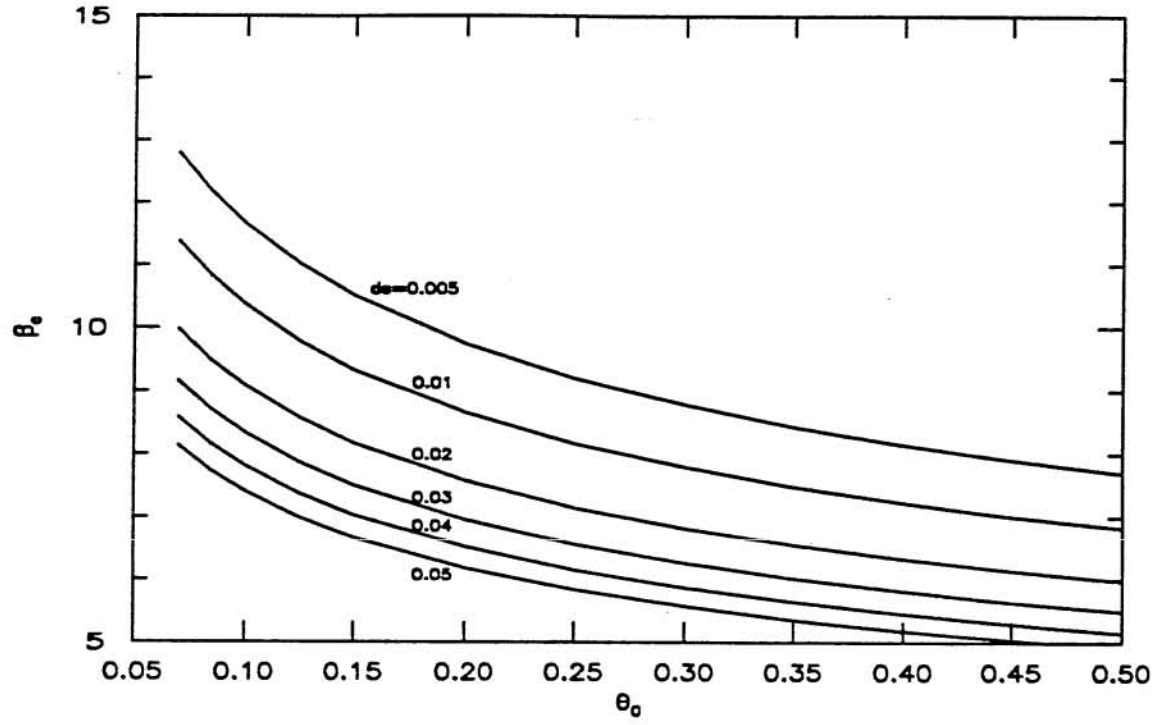

Fig.3.5 β_c as a function of θ_0 and d_s. Linear Theory. Engelund–Hansen Bedload Relationship; Flat–bed Engelund–Hansen Resistance Equation.

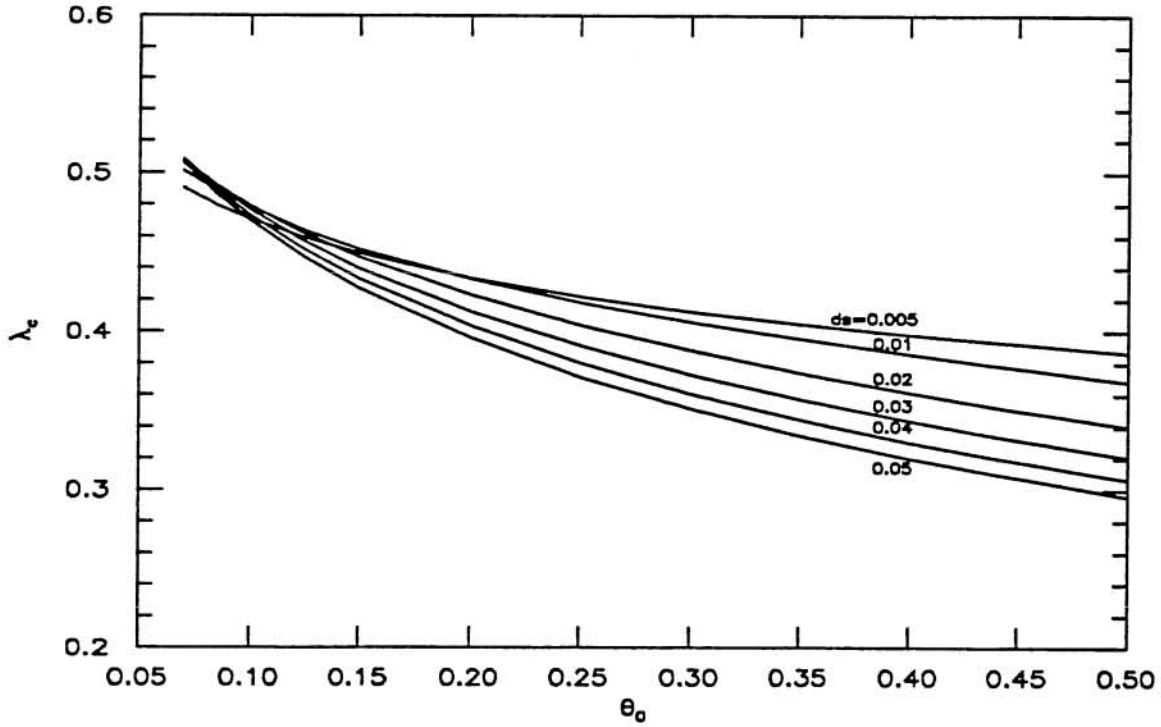

Fig.3.6 λ_c as a function of θ_0 and d_s. Linear Theory. Engelund–Hansen Bedload Relationship; Flat–bed Engelund–Hansen Resistance Equation.

By combining the Engelund–Hansen bedload relationship (3.7b) with the Engelund–Hansen resistance equation for dune–covered beds (3.5b), s_1, s_2, f_1 and f_2 can be expressed as:

$$s_1 = 2\,(1-c_T)^{-1} \quad , \quad s_2 = c_D\,(1-c_T)^{-1} \quad , \quad f_1 = (5-2\,c_T)\,(1-c_T)^{-1} \qquad (3.26a\text{–}c)$$

$$f_2 = c_D\,((2.5-c_T)\,(1-c_T)^{-1}-1) \qquad (3.26d)$$

where,

$$c_D = -5\,\left(\frac{\theta_0'}{\theta_0}\,C_0\right)^{\frac{1}{2}} \quad , \quad c_T = \frac{\left(\frac{0.06}{\theta_0}-0.4\,\theta_0\right)}{\left(\frac{0.06}{\theta_0}+0.4\,\theta_0\right)}\left(1+5\left(\frac{\theta_0'}{\theta_0}\,C_0\right)^{\frac{1}{2}}\right) \qquad (3.27a, b)$$

$$\left(\frac{\theta_0'}{\theta_0}\,C_0\right)^{\frac{1}{2}} = \left[\,6+2.5\,\ln\left(\left(\frac{0.06}{\theta_0}+0.4\,\theta_0\right)\frac{1}{2.5\,d_s}\right)\right]^{-1} \qquad (3.27c)$$

Again, with these relationships, the values of β_c and λ_c are computed from (3.22) as functions of θ_0 and d_s, using the definitions (3.18), (3.19) and (3.23). The results obtained are presented in Figs. 3.7 and 3.8, respectively.

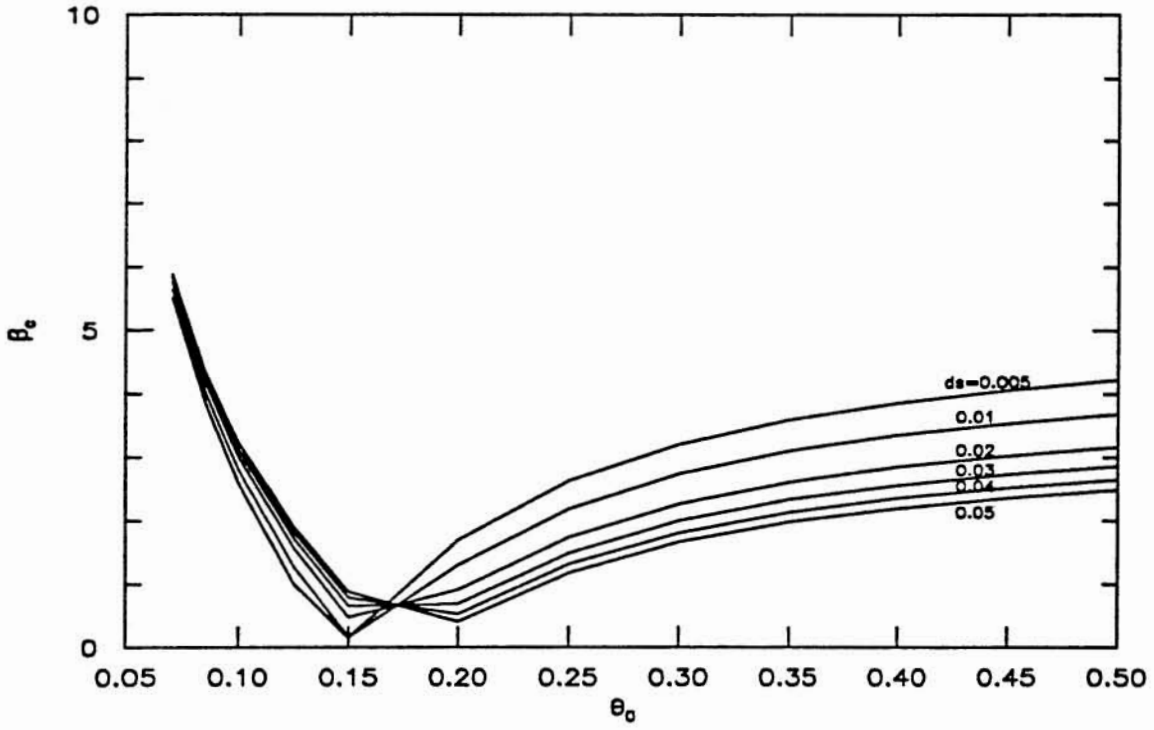

Fig.3.7 β_c as a function of θ_0 and d_s. Linear Theory. Engelund–Hansen Bedload Relationship; Dune–bed Engelund–Hansen Resistance Equation.

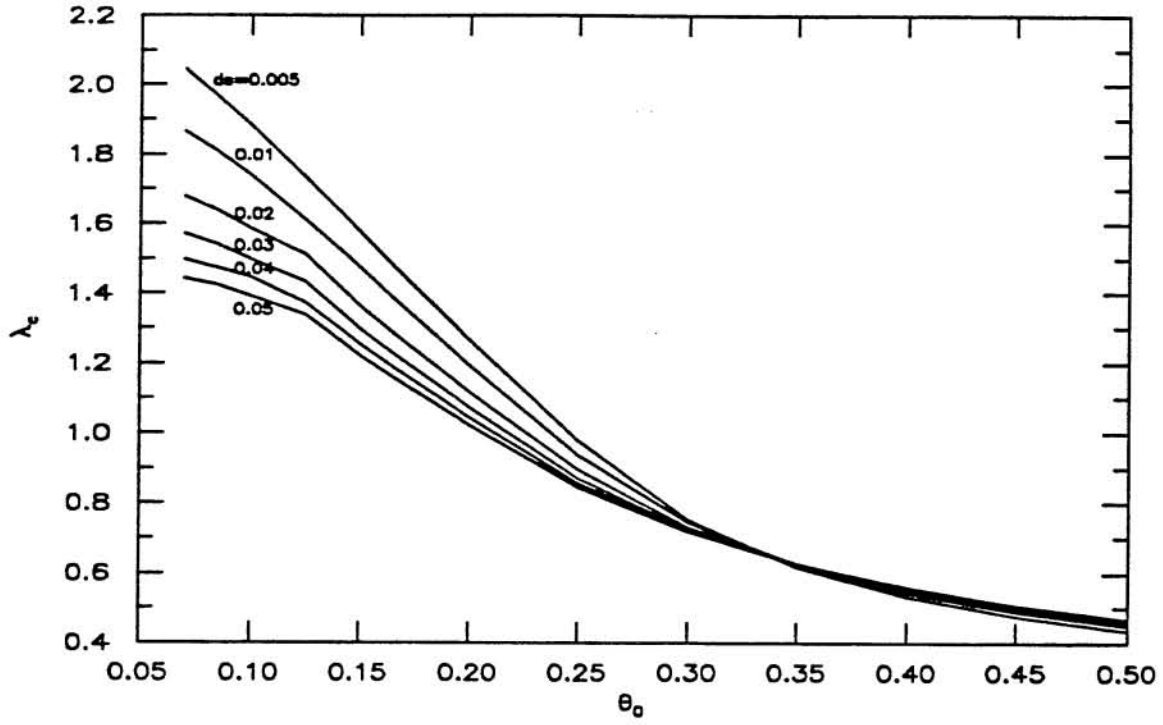

Fig.3.8 λ_c as a function of θ_0 and d_s. Linear Theory. Engelund–Hansen Bedload Relationship; Dune–bed Engelund–Hansen Resistance Equation.

As it can be concluded from Figs. 3.3 to 3.8, the use of different resistance and bedload relationships has important influence on the results obtained for β_c and λ_c, as predicted by the linear theory. Comparing Figs. 3.3 and 3.5, it is clear that the bedload equation selected has major incidence not only on the values but also on the behavior of β_c as a function of θ_0, specially for values of this parameter lower than 0.20. In fact, while for the Meyer–Peter and Muller formula β_c increases with θ_0 in that range, for the flat–bed Engelund–Hansen equation that behavior is exactly the opposite. On the other hand, from Figs. 3.4 and 3.6, it can be noticed that the critical wavenumber λ_c is less sensible to the bedload equation selected than β_c, showing a slightly different behavior in one case or the other. This behavior, however, becomes more markedly different in the range $\theta_0 < 0.10$. Comparing Figs. 3.5, 3.6, 3.7 and 3.8, it can be concluded that the hydraulic resistance to the flow also has major influence on the results obtained for β_c and λ_c, as it is reflected by the use of a flat–bed or a dune–bed resistance equation. In general terms, much lower values of β_c are obtained for the dune–bed formula than for the flat–bed equation, while much larger values of λ_c result from the use of the dune–bed equation than from the use of the flat–bed formula.

In order to get an idea of the order of magnitude of the migration speed of the incipient alternate bar perturbations, the critical angular frequency ω_c was computed by

replacing the values of β_c and λ_c, as functions of θ_0 and d_s, into 3.21. The Engelund–Hansen bedload formula and the flat-bed Engelund–Hansen resistance equation were used in the computation. The results obtained are presented in Fig. 3.9.

Finally, with the aim of obtaining graphical relationships that allow an easy comparison with the experimental results obtained in the present research, the values of the celerity c_c^* and wavelength L_c^* of the alternate bars at the critical point, computed as:

$$c_c^* = U_0^* \frac{\omega_c}{\lambda_c} \quad , \quad L_c^* = B \frac{2\pi}{\lambda_c} \qquad (3.28a, b)$$

are presented in Figs. 3.10 and 3.11 respectively. In preparing those figures, the Engelund–Hansen bedload formula and the flat-bed Engelund–Hansen resistance relationship were used.

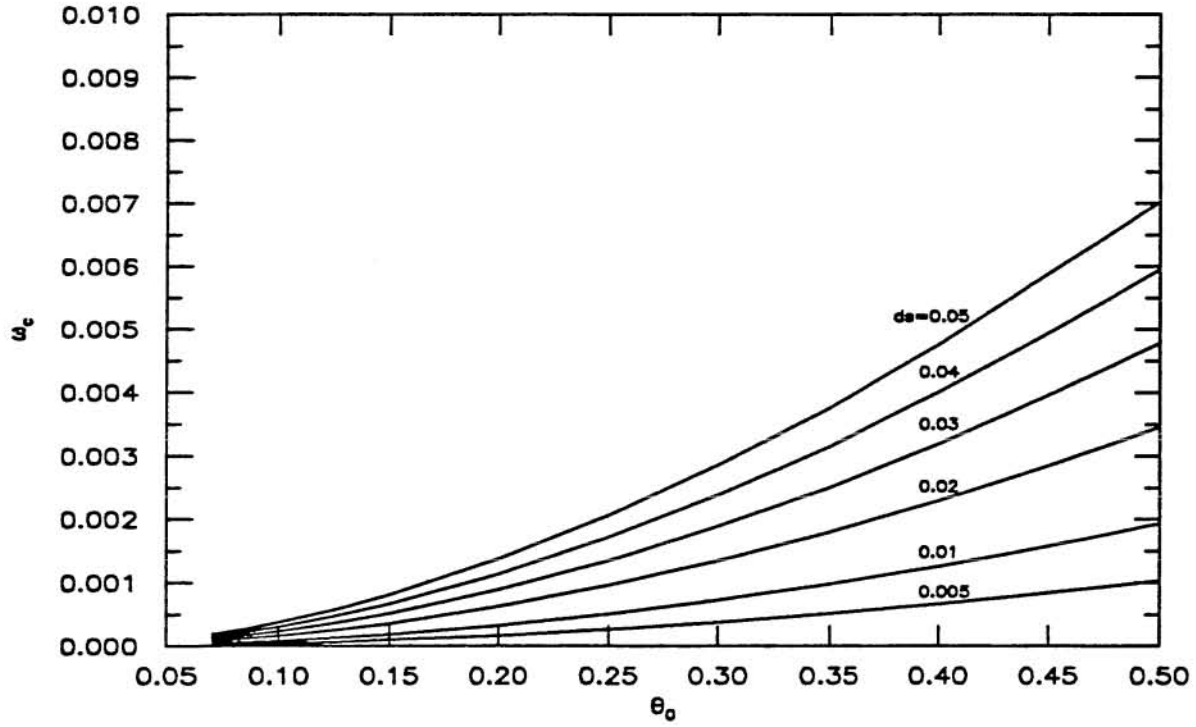

Fig.3.9 ω_c as a function of θ_0 and d_s. Linear Theory. Engelund–Hansen Bedload Relationship; Flat-bed Engelund–Hansen Resistance Equation.

3.4 Resonance Conditions

In what follows, an analysis similar to that presented in the preceding section is developed with the aim of obtaining graphical relationships for the conditions associated with the resonance phenomenon as described in Chapter 2.

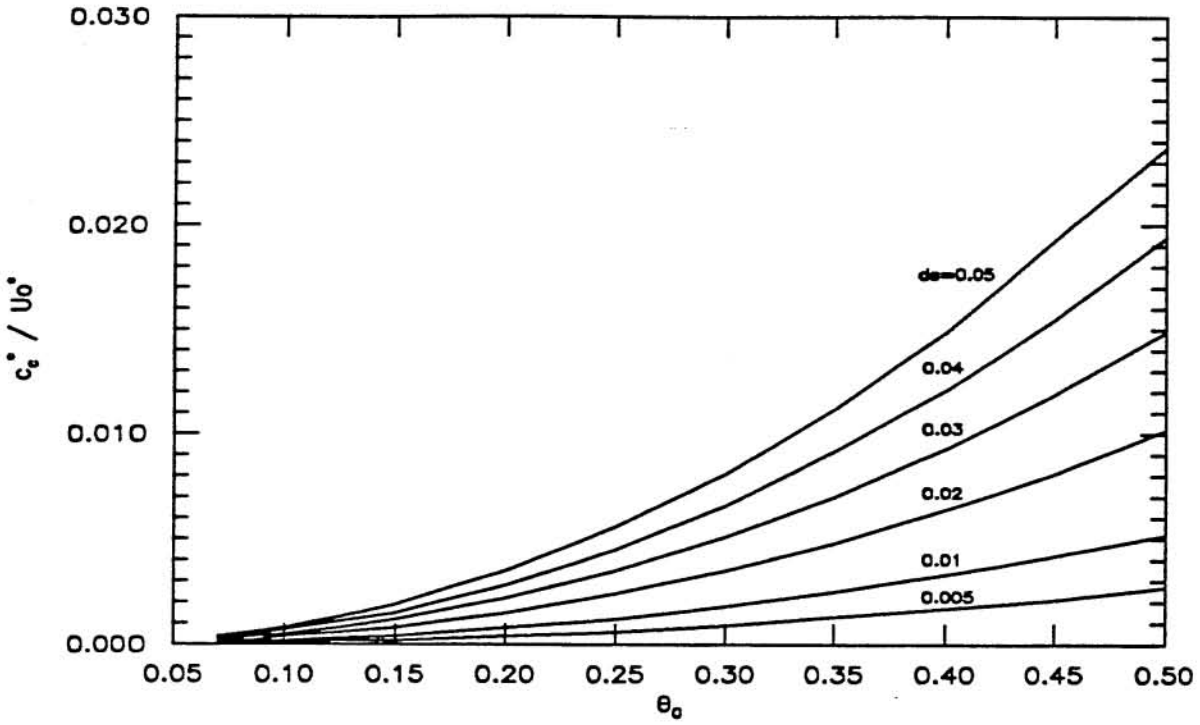

Fig.3.10 c_c^*/U_0^* as a function of θ_0 and d_s. Linear Theory. Engelund–Hansen Bedload Relationship; Flat–bed Engelund–Hansen Resistance Equation.

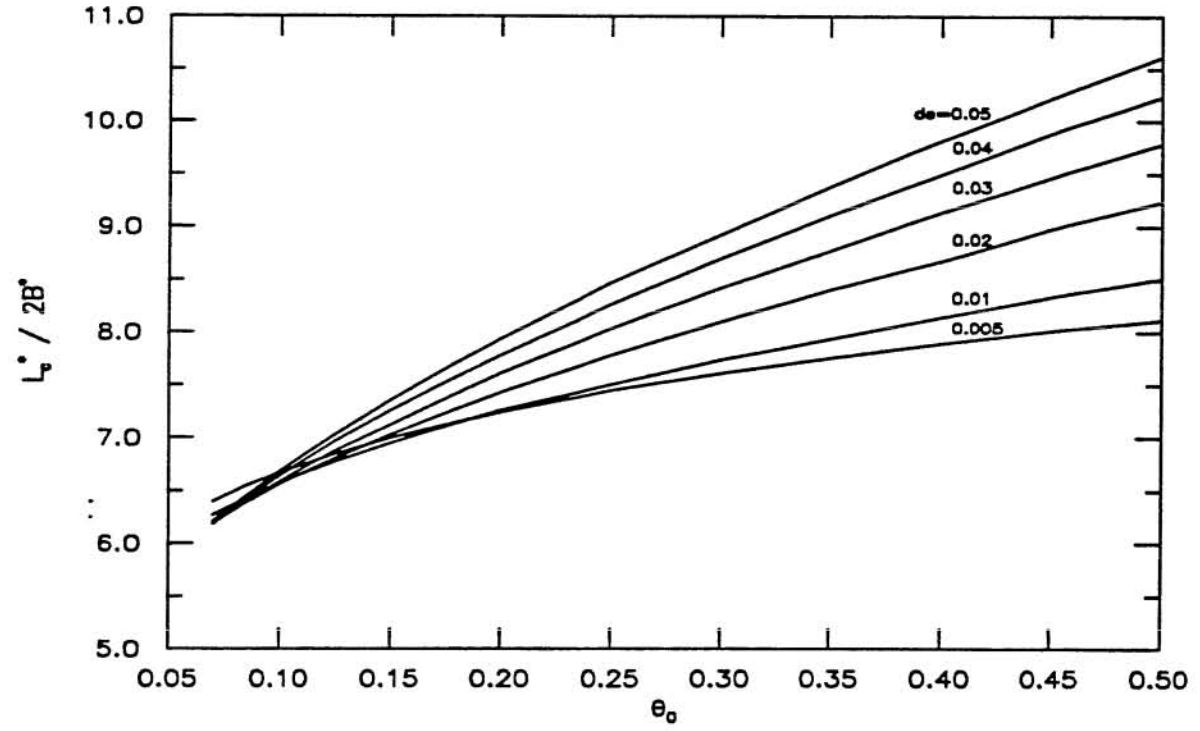

Fig.3.11 $L_c^*/2B^*$ as a function of θ_0 and d_s. Linear Theory. Engelund–Hansen Bedload Relationship; Flat–bed Engelund–Hansen Resistance Equation.

As it can be observed in Fig. 3.2, one of the possible responses of the flow–sediment system to the linear stability analysis performed in 3.2, corresponds to perturbations of zero rate of growth and zero migration speed. These perturbations however do not develop naturally in a straight channel, since in that situation the most probable perturbations to develop correspond to those associated with the critical point analyzed in 3.3 (Blondeaux and Seminara, 1985). Nevertheless, if the channel is not straight but has a small sinuosity, such that its wavenumber falls within the range of the vanishing rate of growth and celerity perturbations, then according to the analysis of Blondeaux and seminara (1985), the forcing effect of the curvature of the channel axis does select such kind of perturbations, thus leading to the resonance phenomenon discussed in Chapter 2.

By setting $\omega = 0$ in (3.21), the following equation is obtained, which for fixed values of θ_0 and d_s allows to compute the angular frequency neutral curve in the plane (λ, β).

$$a_3' \lambda^6 + a_2' \lambda^4 + a_1' \lambda^2 + a_0' = 0 \qquad (3.29)$$

where,

$$a_0' = A_5 B_1 - A_4 B_0 \quad , \quad a_1' = A_3 B_1 + A_5 B_3 - A_2 B_0 - A_4 B_2 \qquad (3.30a, b)$$

$$a_2' = A_1 B_1 + A_3 B_3 - A_2 B_2 \quad , \quad a_3' = A_1 B_3 \qquad (3.30c, d)$$

If the system of equations formed by (3.29) and (3.22) is solved simultaneously, then the resonant point (λ_R, β_R) is obtained, for which $\omega = \Omega = 0$. This resonant point, as the critical point derived in 3.3, is a function of θ_0 and d_s and also of the bedload and resistance equations used in its derivation.

Figs. 3.12 to 3.15 present the results for λ_R and β_R, obtained by solving the system formed by (3.29) and (3.22). In those figures the resonant variables are plotted as functions of θ_0 and d_s. Figs. 3.12 and 3.13 show the results corresponding to the use of the Meyer–Peter and Muller bedload formula (3.7a) and the flat–bed Engelund–Hansen resistance equation (3.5a). Likewise, Figs. 3.14 and 3.15 present the results corresponding to the use of the Engelund–Hansen bedload relationship (3.7b) and the flat–bed Engelund–Hansen resistance equation (3.5a).

As can be observed in those figures, the bedload equation utilized in the analysis plays an important role in the results obtained for the resonant values of β. While Meyer–Peter and Muller formula gives values of β_R in the range 10–100, Engelund–Hansen relationship generates values of that parameter in the range 7–16. This extremely different range of values is not so unexpected, since as can be observed in the example of Fig. 3.2, the slope of the neutral curve $\Omega = 0$ in the resonant zone is very steep, and therefore any small variation in

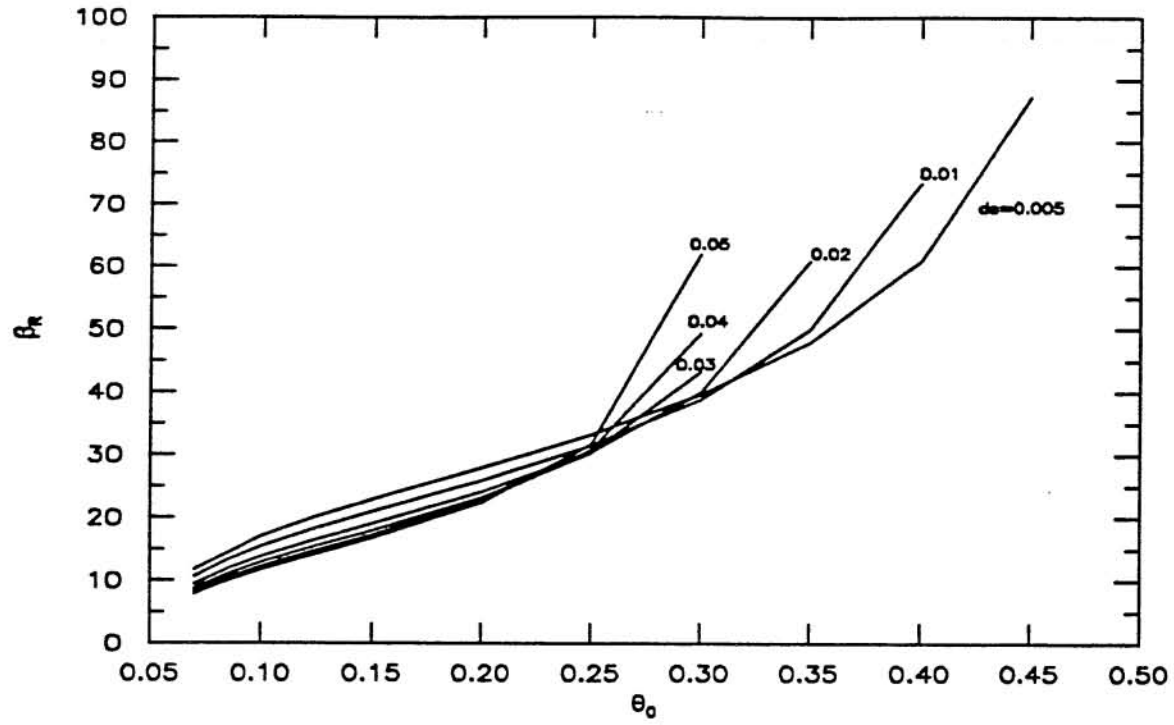

Fig.3.12 β_R as a function of θ_0 and d_s. Linear Theory. Meyer-Peter and Muller Bedload Relationship; Flat-bed Engelund-Hansen Resistance Equation.

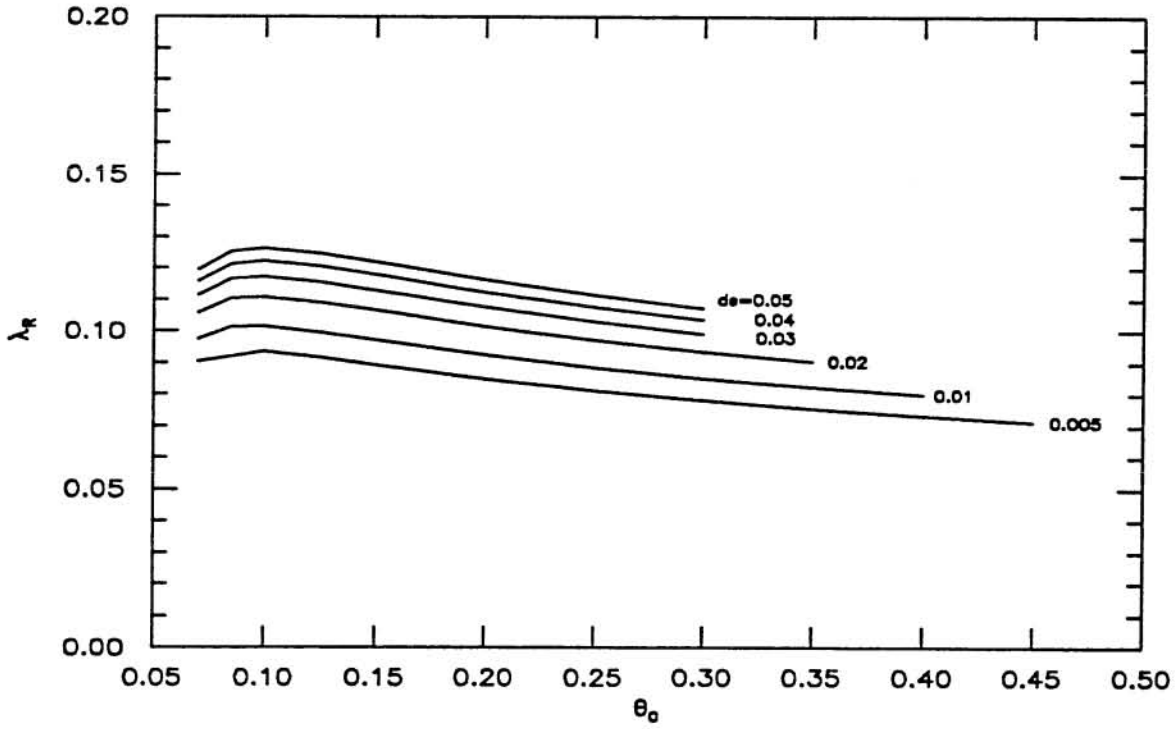

Fig.3.13 λ_R as a function of θ_0 and d_s. Linear Theory. Meyer-Peter and Muller Bedload Relationship; Flat-bed Engelund-Hansen Resistance Equation.

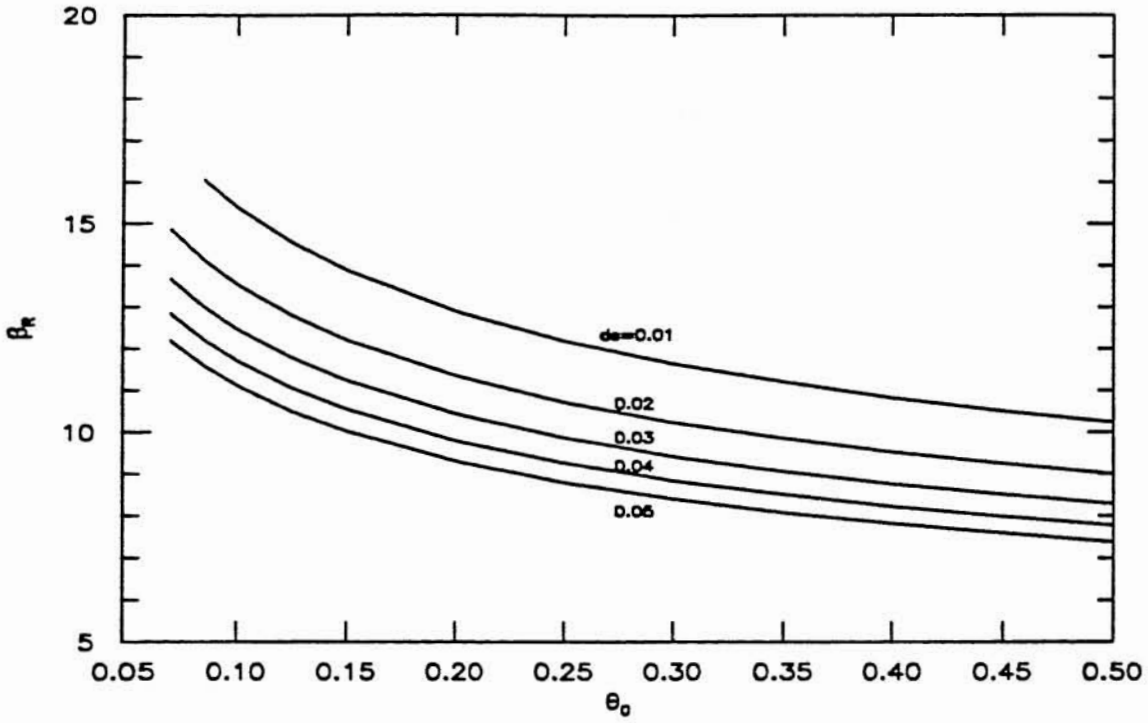

Fig.3.14 β_R as a function of θ_0 and d_s. Linear Theory. Engelund–Hansen Bedload Relationship; Flat–bed Engelund–Hansen Resistance Equation.

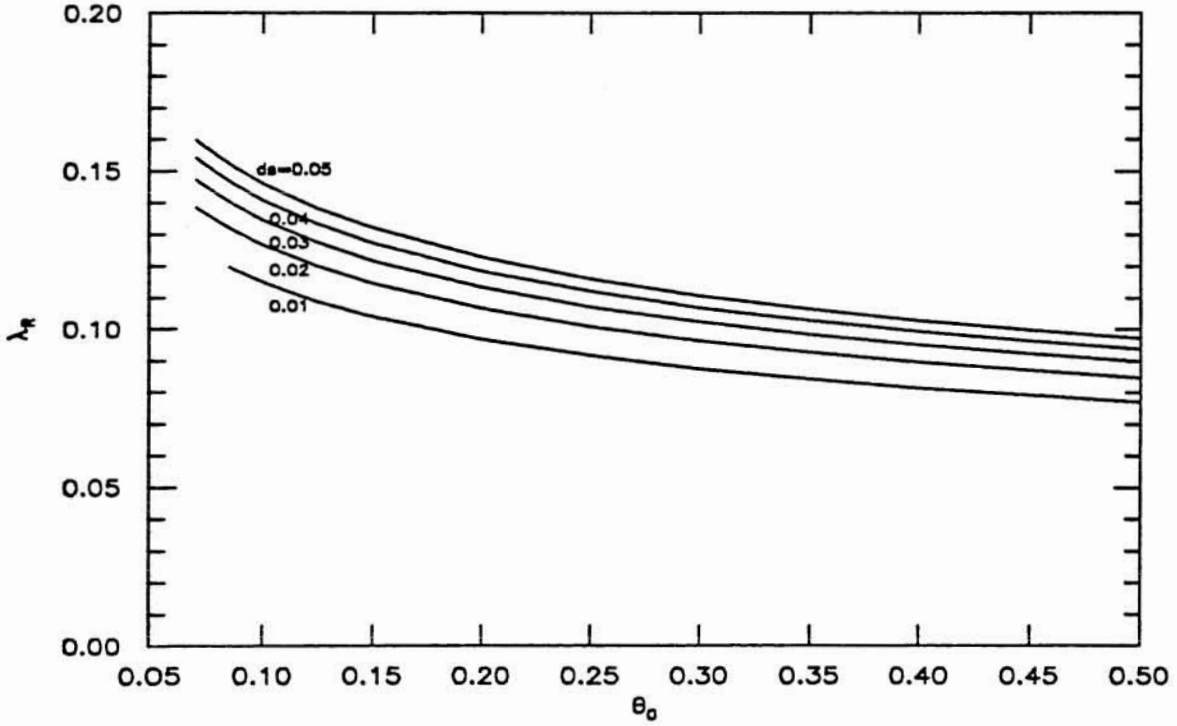

Fig.3.15 λ_R as a function of θ_0 and d_s. Linear Theory. Engelund–Hansen Bedload Relationship; Flat–bed Engelund–Hansen Resistance Equation.

the neutral curve $\omega = 0$, can lead to extremely different values of β_R. On the other hand, Figs. 3.13 and 3.15 show that the bedload equation utilized in the analysis affects only slightly the results obtained for the resonant wavenumber λ_R, which in both of the analyzed cases is in the range 0.10–0.15. By comparing this range with the range of values of the critical wavenumber λ_c as obtained in Figs. 3.4 and 3.6 for flat–bed conditions: 0.3–0.5, it can be concluded that the resonant wavelength, which is associated with incipient meandering wavelength after Blondeaux and Seminara (1985), is two to three times larger than the wavelength of incipient alternate bars.

As was mentioned in Chapter 2, Parker and Johannesson (1989) derived explicit predictive relationships for the resonant conditions of alternate bars, which however are not expressed in terms of (λ_R, β_R). In the following, their conditions are translated to the nomenclature utilized in the analysis presented above, in order to allow an easy comparison of the results.

The linear analysis of Parker and Johannesson (1989) leading to the resonant conditions for alternate bars is basically the same as that derived herein, however differences in treating the governing equations and in the simplifications introduced make both approaches slightly different. Using the Engelund–Hansen bedload formula and the Engelund–Hansen resistance equation for flat–bed conditions, the resonant values of β and λ, as predicted by Parker and Johannesson (1989), can be written as:

$$\beta_R = 6.41 \ln \left(\frac{5.5}{d_s} \right) \left[\left(\frac{\theta_0}{\theta_{cr}} \right)^{\frac{1}{2}} \frac{\left(0.5 \frac{\theta_0}{\theta_{cr}} + 1 \right)}{\left(\frac{\theta_0}{\theta_{cr}} - 1 \right)} \right]^{-\frac{1}{2}} \qquad (3.31a)$$

$$\lambda_R = 1.45 \left(\frac{\theta_0}{\theta_{cr}} \right)^{-\frac{1}{4}} \left(\ln \left(\frac{5.5}{d_s} \right) \right)^{-1} \qquad (3.31b)$$

Figs. 3.16 and 3.17 show β_R and λ_R given by (3.31), plotted as functions of θ_0 and d_s. In those figures a constant value of $\theta_{cr} = 0.05$ was used in order to avoid the introduction of an independent expression for this parameter.

As it can be observed in Figs. 3.16 and 3.17, the values of β_R and λ_R predicted by the theory of Parker and Johannesson are larger than those presented in Figs. 3.14 and 3.15 for the same bedload and resistance equations. Typically, values of β_R predicted by Parker and Johannesson are in the range 15–30, which correspond to about twice the magnitude of the values obtained in the present analysis. Likewise, the values of λ_R predicted by Parker and Johannesson are in the range 0.15–0.30, which also correspond to about twice the magnitude of the values obtained in the present analysis. As it was pointed out before, the resonant

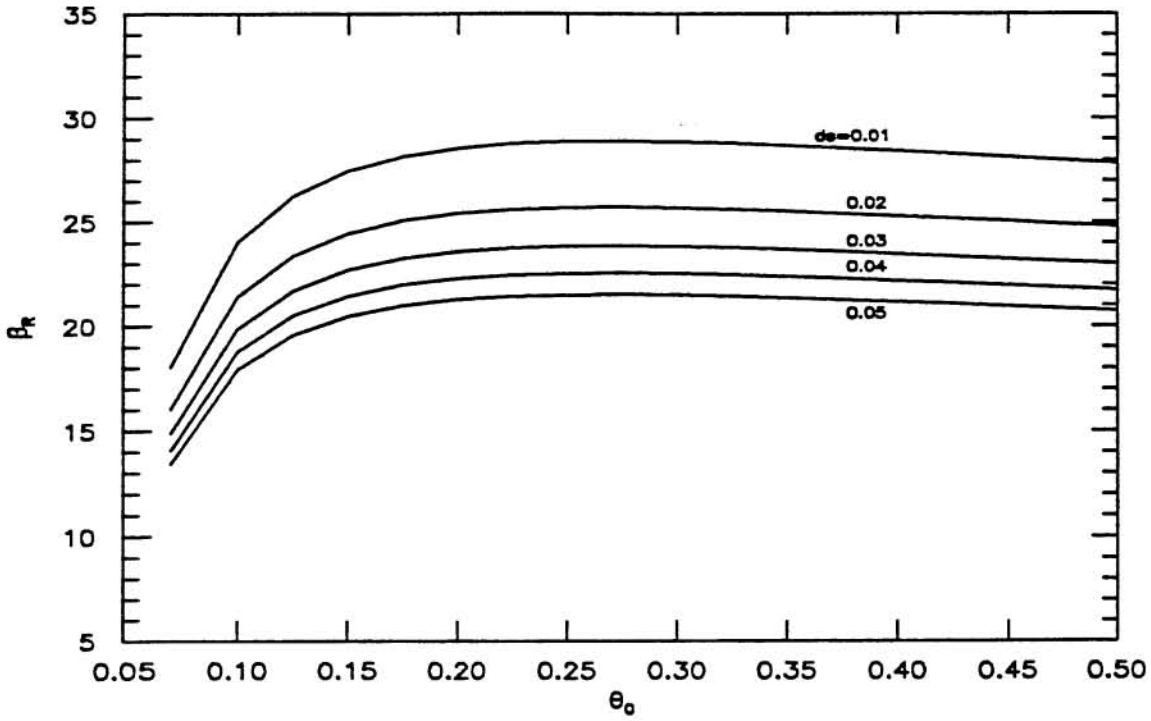

Fig.3.16 β_R as a function of θ_0 and d_s. Parker and Johannesson Theory. Engelund–Hansen Bedload Relationship; Flat–bed Engelund–Hansen Resistance Equation.

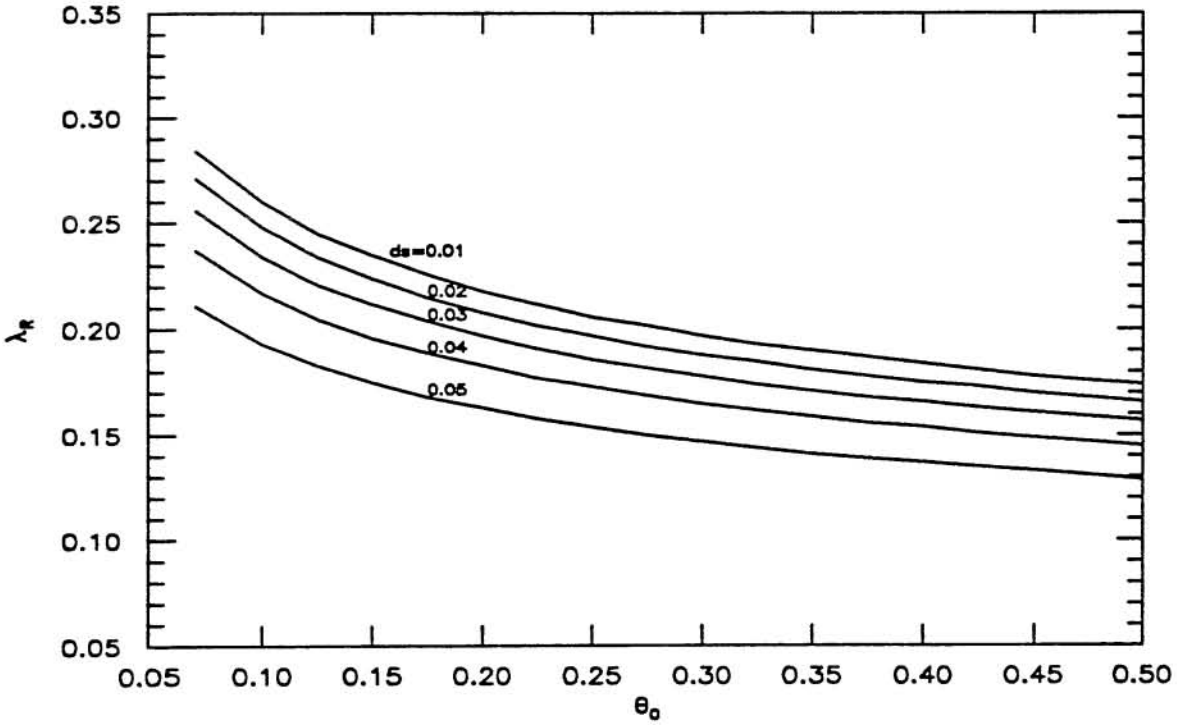

Fig.3.17 λ_R as a function of θ_0 and d_s. Parker and Johannesson Theory. Engelund–Hansen Bedload Relationship; Flat–bed Engelund–Hansen Resistance Equation.

wavenumbers obtained in the present analysis are in the range 0.10–0.15, which led to the conclusion that the resonant wavelength is of the order of two to three times the wavelength of incipient alternate bars. Following the analysis of Parker and Johannesson, that conclusion is relatively well supported, as the resonant wavelengths obtained through this analysis are still of the order of two times the wavelength of incipient alternate bars.

4. NUMERICAL MODEL FOR FLOW AND BED DEFORMATION IN MEANDERING CHANNELS

4.1 Introduction

In the present chapter some numerical results obtained with a simplified two–dimensional numerical model for the flow and bed deformation in meandering channels, are presented. The numerical model was developed based on models available in the literature, particularly on that of Shimizu and Itakura (1989a). The main objective of the application of the model is two fold. In the first place it will help to understand the principal characteristics of the physical processes involved. In the second place, it will provide an opportunity to evaluate how well does the set of governing equations commonly used in analytical and numerical studies of flow and bed deformation in meandering channels do in the modeling of such phenomena, by providing numerical data to be compared with the experimental results obtained in the present research.

4.2 Governing Equations

Different sets of governing equations have been used in analytical and numerical studies on the modeling of flow and bed deformation in meandering channels (see for example River Meandering, Ikeda and Parker eds., 1989), however the most successful attempts have considered at least the use of momentum equations in axial and transverse directions coupled with continuity equations for both water and sediment, making use of the quasi–steady approximation for a slowly varying erodible bottom. In general, the assumption that the channel width and radius of curvature are large compared to the flow depth is valid, which allows to neglect vertical components of velocity and also to consider the hydrostatic pressure distribution as valid. These assumptions, clearly break down in the vicinity of the channel banks, however these defects are local in nature and have a small effect on the overall flow pattern. Accordingly, most of the studies use vertically–averaged equations (Smith and McLean, 1984; Blondeaux and Seminara, 1985; Shimizu and Itakura, 1989a), even though the use of the non–averaged form for some of the governing equations has also been considered in the literature (Parker and Johannesson, 1989; Nelson and Smith, 1989). Since the use of vertically–averaged equations precludes the adequate modeling of the transverse sediment transport, some of the studies revised have included explicitly the effect that the component of secondary flow with zero vertical average has on the direction and intensity of the bedload motion. The models of Parker (1984) and Hasewaga (1981) are typically used with this purpose (Blondeaux and Seminara, 1985; Shimizu and Itakura, 1989a; Parker and Johannesson, 1989).

The channel under consideration has a constant width 2B, non-erodible banks, non-cohesive uniform sediment bed, and a variable curvature along its axis. Most of the models revised utilize intrinsic coordinates (s,n) to express the governing equations, where s denotes the axial coordinate, usually measured along the centerline of the channel, and n denotes the transverse coordinate. Some of the models express the governing equations in terms of the local value of the radius of curvature r, although most of them use the centerline value of this parameter, R, usually written in terms of the centerline curvature C, where $C = 1/R$. Fig. 4.1 shows a scheme of the channel, defining the system of coordinates and other variables used in the analysis.

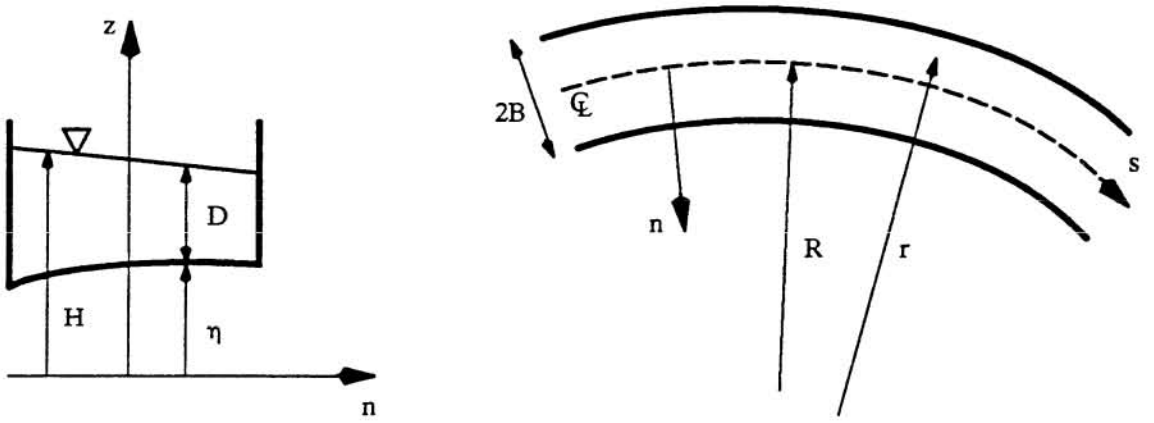

Fig. 4.1 Scheme of the Channel and Definition of Variables.

Of the models revised, the numerical model of Shimizu and Itakura (1989a) is the one that makes use of the most complete form of the two-dimensional depth-averaged set of governing equations. This set of equations is written as:

$$U \frac{\partial U}{\partial s} + V \frac{\partial U}{\partial n} + \frac{U V}{r} = - g \frac{\partial H}{\partial s} - \frac{\tau_s}{\varrho D} + 2 \frac{\partial}{\partial s} \left(\epsilon \frac{\partial U}{\partial s} \right) + \frac{\partial}{\partial n} \left(\epsilon \frac{\partial U}{\partial n} \right) \qquad (4.1a)$$

$$U \frac{\partial V}{\partial s} + V \frac{\partial V}{\partial n} - \frac{U^2}{r} = - g \frac{\partial H}{\partial n} - \frac{\tau_n}{\varrho D} + \frac{\partial}{\partial s} \left(\epsilon \frac{\partial V}{\partial s} \right) + 2 \frac{\partial}{\partial n} \left(\epsilon \frac{\partial V}{\partial n} \right) \qquad (4.1b)$$

$$\frac{\partial (U D)}{\partial s} + \frac{1}{r} \frac{\partial (r V D)}{\partial n} = 0 \qquad (4.1c)$$

$$\frac{\partial \eta}{\partial t} + \frac{1}{1-p} \left(\frac{\partial Q_s}{\partial s} + \frac{1}{r} \frac{\partial (r Q_n)}{\partial n} \right) = 0 \qquad (4.1d)$$

where, (U,V) are the depth averaged velocity components in s and n directions respectively, τ_s and τ_n are the bottom shear stresses, H is the water surface elevation, D is the local flow depth, Q_s and Q_n are the volumetric sediment flow rate per unit width components which are assumed to correspond mainly to bedload transport, ρ is the water density, g is the gravitational acceleration, p is the sediment porosity, r is the local radius of curvature and ϵ is a depth–averaged diffusion coefficient for fully turbulent flow.

As it is pointed out by Shimizu and Itakura, the diffusion terms are accounted for in their model because of numerical stability reasons, and not due to their actual physical importance. If $\epsilon = 0$ in (4.1), then the set of equations used by Blondeaux and Seminara (1985) in their analytical study is obtained. Parker and Johannesson (1989), also in a theoretical analysis, used a set of equations similar to (4.1), however they derived a non–depth–averaged version of the transverse momentum equation (4.1b). Smith and McLean (1984) also assumed $\epsilon = 0$, however they did not take into account the bed variation in their analysis, thus neglecting the sediment continuity equation (4.1d). These authors also derived a simplified form for the transverse momentum equation based on order of magnitude considerations.

Neglecting ϵ in (4.1) and expressing the equations in terms of the centerline curvature C, the following system of equations is found:

$$U \frac{\partial U}{\partial s} + V \frac{\partial U}{\partial n} + \frac{C}{(1 + n\,C)}\, U\,V = -\,g \frac{\partial H}{\partial s} - \frac{\tau_s}{\rho\, D} \tag{4.2a}$$

$$U \frac{\partial V}{\partial s} + V \frac{\partial V}{\partial n} - \frac{C}{(1 + n\,C)}\, U^2 = -\,g \frac{\partial H}{\partial n} - \frac{\tau_n}{\rho\, D} \tag{4.2b}$$

$$\frac{\partial (U\,D)}{\partial s} + \frac{1}{(1 + n\,C)} \frac{\partial ((1 + n\,C)\,V\,D)}{\partial n} = 0 \tag{4.2c}$$

$$\frac{\partial \eta}{\partial t} + \frac{1}{1-p} \left(\frac{\partial Q_s}{\partial s} + \frac{1}{(1 + n\,C)} \frac{\partial ((1 + n\,C)\,Q_n)}{\partial n} \right) = 0 \tag{4.2d}$$

where s denotes the local value of the axial coordinate and not the value associated with the centerline of the channel. Smith and McLean (1984) (see also Dietrich and Whiting, 1989 and Nelson and Smith, 1989) using scaling arguments showed that (4.2b) can be reduced to:

$$\frac{C}{(1 + n\,C)}\, U^2 = g \frac{\partial H}{\partial n} \tag{4.3}$$

equation which has also been used by Shimizu and Itakura (1989b).

From Fig. 4.1, the following relationships can be derived:

$$\frac{\partial H}{\partial s} = \frac{\partial D}{\partial s} + \frac{\partial \eta}{\partial s} \quad , \quad \frac{\partial H}{\partial n} = \frac{\partial D}{\partial n} + \frac{\partial \eta}{\partial n} \qquad (4.4a, b)$$

where η denotes bed elevation. This variable can be expressed in terms of the mean slope of the channel such that:

$$\eta = \eta_0 - S_0\, s + \eta' \qquad (4.5a)$$

$$\frac{\partial \eta}{\partial s} = -S_0 + \frac{\partial \eta'}{\partial s} \quad , \quad \frac{\partial \eta}{\partial n} = \frac{\partial \eta'}{\partial n} \quad , \quad \frac{\partial \eta}{\partial t} = \frac{\partial \eta'}{\partial t} \qquad (4.5b\text{–}d)$$

where η_0 denotes the value of the mean bed elevation at $s=0$, S_0 is the slope of the channel and η' denotes the local deviation of the bed elevation with respect to the mean value defined by the slope of the channel. Fig. 4.2 shows a sketch for the definition of these variables.

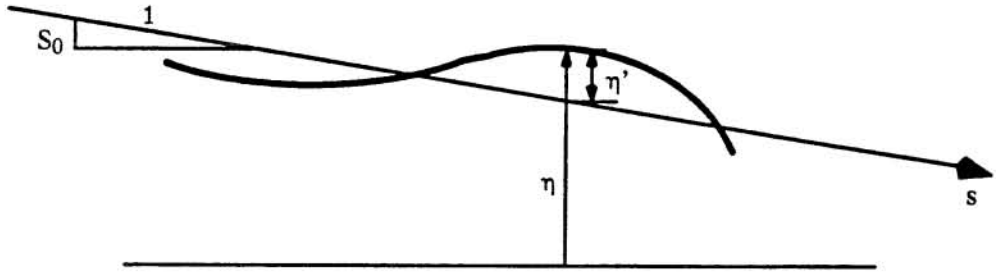

Fig. 4.2 Sketch for the Definition of Variables.

Using relations (4.5) and expressing momentum equations in flux form, which is useful for the development of the numerical scheme presented in the next section, the system (4.2) can be rewritten as follows:

$$\frac{\partial (U^2 D)}{\partial s} + \frac{1}{(1+n\,C)} \frac{\partial ((1+n\,C)\,U\,V\,D)}{\partial n} = -g\,D\left(\frac{\partial D}{\partial s} - S_0 + \frac{\partial \eta'}{\partial s}\right) - \frac{\tau_s}{\varrho} \qquad (4.6a)$$

$$\frac{\partial (UVD)}{\partial s} + \frac{1}{(1+n\,C)} \frac{\partial ((1+n\,C)\,V^2 D)}{\partial n} - \frac{C}{(1+n\,C)} (U^2 D) = -g\left(\frac{\partial D}{\partial n} + \frac{\partial \eta'}{\partial n}\right) - \frac{\tau_n}{\varrho} \qquad (4.6b)$$

$$\frac{\partial (U D)}{\partial s} + \frac{1}{(1+n\,C)} \frac{\partial ((1+n\,C)\,V D)}{\partial n} = 0 \qquad (4.6c)$$

$$\frac{\partial \eta'}{\partial t} + \frac{1}{1-p}\left(\frac{\partial Q_s}{\partial s} + \frac{1}{(1+n\,C)} \frac{\partial ((1+n\,C)\,Q_n)}{\partial n}\right) = 0 \qquad (4.6d)$$

Following Smith and McLean (1984), (4.2b) can be reduced to:

$$\frac{C}{(1+nC)}U^2 = g\left(\frac{\partial D}{\partial n} + \frac{\partial \eta'}{\partial n}\right) \qquad (4.7)$$

In order to close the set of governing equations in any of the forms written above, resistance and bedload relationships are needed to express bottom shear stresses and the components of sediment transport rate as functions of flow and sediment parameters. Following Shimizu and Itakura (1989a), Manning's equation is used in what follows as resistance relation, assuming the wide channel approximation to be valid, such that:

$$\frac{\tau_s}{\varrho} = \frac{g\, n_m^{\,2}}{D^{\frac{1}{3}}} U\left(U^2+V^2\right)^{\frac{1}{2}} \quad , \quad \frac{\tau_n}{\varrho} = \frac{g\, n_m^{\,2}}{D^{\frac{1}{3}}} V\left(U^2+V^2\right)^{\frac{1}{2}} \qquad (4.8a, b)$$

where n_m denotes Manning's coefficient. This coefficient is calibrated using the experimental data collected in the experimental study made as part of the present research, thus reducing the sources of error introduced by the selection of the resistance relationship.

To model the sediment transport rate in the axial direction, Q_s, the Engelund–Hansen bedload formula is used, which as will be discussed in following chapters represents adequately the sediment transport measured in the experiments made as part of the present research. This formula is written as:

$$Q_s = \left(\left(\frac{\varrho_s - \varrho}{\varrho}\right) g\, d_s^3\right)^{\frac{1}{2}} \Phi \qquad (4.9)$$

with Φ given by:

$$\Phi = \frac{0.05}{C_0}\theta^{2.5} \quad , \quad C_0 = \left(6 + \ln\left(\frac{D}{2.5\, d_s}\right)\right)^{-2} \quad , \quad \theta = \frac{\tau_s}{(\varrho_s - \varrho)\, g\, d_s} \qquad (4.10a\text{–}c)$$

where ρ_s and d_s denote density and diameter of the uniform sediment, C_0 is a friction coefficient and θ represents the Shields parameter.

The modeling of the transverse sediment transport is perhaps the most crucial point in the whole analysis of bed deformation in meandering channels. Since only the depth–averaged value of the transverse velocity is considered in the governing equations special attention is given to introduce explicitly the effect of the secondary flow with zero depth–average in the model for the lateral sediment transport component. Also, this variable is affected by the component of gravity due to the transverse slope of the bed developed because of the curvature of the channel axis. In general both aspects discussed above have been modeled by different authors by using the equation developed by Parker (1984) based on previous work by Engelund (1981) or the one derived by Hasewaga (1981), (see Blondeaux

and Seminara, 1985; Parker and Johannesson, 1989 and Shimizu and Itakura, 1989a). The version of Parker's equation used herein is written as:

$$\frac{Q_n}{Q_s} = \frac{V}{U} - 7\frac{C}{(1+nC)}D - \frac{r}{\theta^{\frac{1}{2}}}\frac{\partial \eta'}{\partial n} \qquad (4.11)$$

where r is a coefficient which has been given different values by different authors. For instance, the following values has been used in the literature: 0.30 (Blondeaux and Seminara, 1985), 0.37 (Shimizu and Itakura, 1989a), 0.60 (Parker and Johannesson, 1989). In the numerical model derived herein, this coefficient will be taken as a parameter.

4.3 Numerical Scheme

In deriving the numerical scheme, the set of governing equations (4.6) is utilized, in which the transverse momentum equation (4.6b) is replaced by its simplified version (4.7). This system poses a boundary value problem for the flow variables (U,V,D) and an initial value problem for the bed deformation η'. This is because the quasi-steady approximation has been used, which assumes that the time scale of the flow response to bed changes is much smaller than the time scale of those changes. In other words the momentum and water continuity equations are solved for (U,V,D) each time step assuming the bed is fixed, and then the sediment continuity equation is used to carry on the bed deformation in time using the values of the flow parameters just computed.

Herein, the set of governing equations is solved using an explicit finite difference scheme, such that U is obtained from the axial momentum equation (4.6a), D is computed from the transverse momentum equation (4.7) starting from the centerline value, which is adjusted such that the water discharge is constant along the channel, and V is solved from water continuity equation (4.6c). With flow parameters known, η' is solved at each time step, also explicitly, from sediment continuity equation (4.6d).

Only one wavelength of the meandering channel is considered in the numerical modeling. As initial conditions, uniform flow and flat bed ($\eta' = 0$) are assumed in the whole channel length. Likewise, at each time step periodic boundary conditions are applied for flow parameters and bed deformation. The computation is carried on until the bed deformation reaches an equilibrium in time.

In what follows, the discretization of the governing equations is presented.

4.3.2 Discretization of Axial Momentum Equation

Equation (4.6a) is discretized using the staggered grid shown in Fig. 4.3. Following Patankar (1980), an upwind scheme is utilized to compute the fluxes in axial and transverse

directions and the source term represented by the right hand size of the equation is linearized as a function of U. τ_s is expressed in terms of flow parameters by using (4.8).

The finite difference form of the axial momentum equation can be written as:

$$K_1\, U_{ij} = K_2\, U_{ij-1} + K_3\, U_{i+1j} + K_4\, U_{i-1j} + K_5 + K_6\, (D_{ij-1} - D_{ij}) \qquad (4.12)$$

where,

$$K_2 = F_w \quad , \quad K_3 = \| -F_s\, ,\, 0 \| \quad , \quad K_4 = \| F_n\, ,\, 0 \| \quad , \quad K_5 = \mathbf{B} \quad , \quad K_6 = \mathbf{A} \qquad (4.13a\text{-}e)$$

$$K_1 = K_2 + K_3 + K_4 + \mathbf{C} \qquad (4.13f)$$

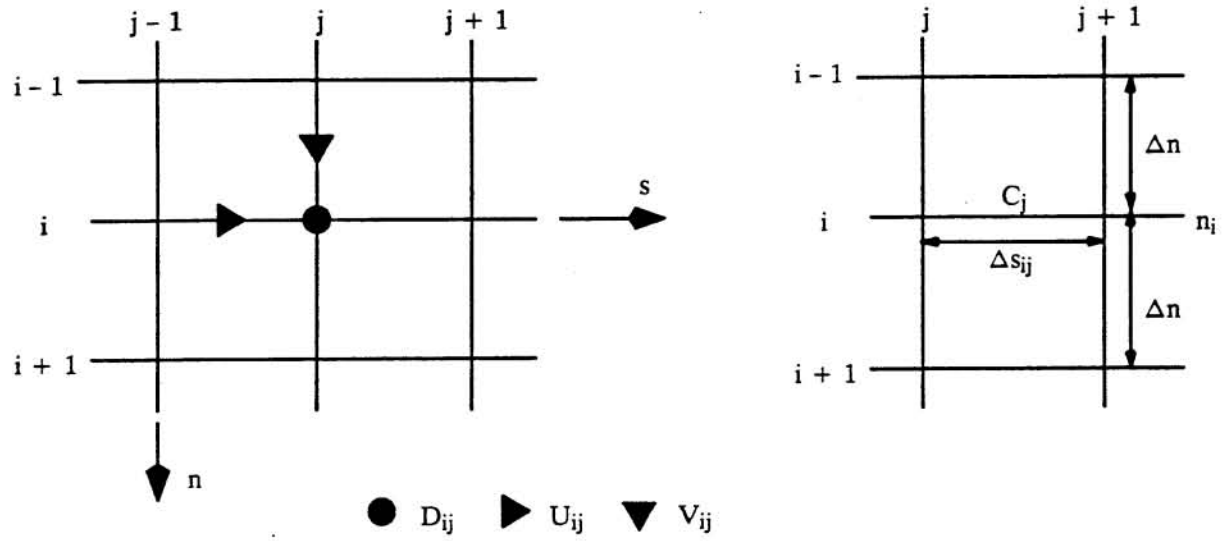

Fig. 4.3 Staggered Grid used by the Numerical Scheme.

and,

$$F_w = 2\, U_{ij}\, U_{ij-1}\, (U_{ij} + U_{ij-1})^{-1}\, \Delta n\, D_{ij-1} \qquad (4.14a)$$

$$F_s = \frac{V_{i+1j}\, V_{i+1j-1}}{(V_{i+1j} + V_{i+1j-1})}\, (\Delta s_{ij-1} + \Delta s_{i+1j-1})\, \frac{(D_{ij} + D_{ij-1} + D_{i+1j} + D_{i+1j-1})}{4} \qquad (4.14b)$$

$$F_n = \frac{V_{ij}\, V_{ij-1}}{(V_{ij} + V_{ij-1})}\, (\Delta s_{i-1j-1} + \Delta s_{ij-1})\, \frac{(D_{ij} + D_{ij-1} + D_{i-1j} + D_{i-1j-1})}{4} \qquad (4.14c)$$

$$\mathbf{A} = g\, \Delta n\, h_* \qquad (4.14d)$$

$$\mathbf{B} = g\, S_0\, \Delta s_{ij-1}\, \Delta n\, D_* + g\, \frac{n_m^{\,2}}{D_*^{\frac{1}{3}}}\, \frac{U_*^{\,3}\, \Delta s_{ij-1}\, \Delta n}{(U_*^{\,2} + V_*^{\,2})^{\frac{1}{2}}} - (\eta'_{ij} - \eta'_{ij-1})\, g\, \Delta n\, D_* \qquad (4.14e)$$

$$\mathbf{C} = g \frac{n_m^{\,2}}{D_*^{\frac{1}{3}}} \Delta s_{ij-1} \Delta n \qquad (4.14f)$$

$$D_* = \frac{1}{2} (D_{ij} + D_{ij-1}) \quad , \quad U_* = U_{ij} \quad , \quad V_* = \frac{1}{4} (V_{ij-1} + V_{ij} + V_{i+1j-1} + V_{i+1j}) \qquad (4.14g\text{-}i)$$

with ‖ a , b ‖, in (4.13), denoting the maximum value between a and b.

4.3.2 Discretization of Transverse Momentum Equation

Using the staggered grid of Fig.4.3, the finite difference form of (4.7) can be written as:

$$D_{i-1j} = D_{ij} + (\eta'_{ij} - \eta'_{i-1j}) - \frac{C_* \Delta n}{g (1 + n_{*1} C_*)} \left(\frac{U_{ij} + U_{ij+1} + U_{i-1j} + U_{i-1j+1}}{4} \right)^2 \qquad (4.15a)$$

$$D_{i+1j} = D_{ij} + (\eta'_{ij} - \eta'_{i+1j}) + \frac{C_* \Delta n}{g (1 + n_{*2} C_*)} \left(\frac{U_{ij} + U_{ij+1} + U_{i+1j} + U_{i+1j+1}}{4} \right)^2 \qquad (4.15b)$$

with,

$$C_* = \frac{1}{2} (C_j + C_{j-1}) \quad , \quad n_{*1} = \frac{1}{2} (n_i + n_{i-1}) \quad , \quad n_{*2} = \frac{1}{2} (n_i + n_{i+1}) \qquad (4.16a\text{-}c)$$

where (4.15a) is used to compute values from the centerline to the left bank and (4.15b) is used to compute values from the centerline to the right bank.

4.3.3 Discretization of Water Continuity Equation

Based in the same staggered grid of Fig. 4.3, the finite difference form of the water continuity equation (4.6c) is written as follows:

$$V_{i+1j} = \frac{\mathbf{B}'}{\mathbf{A}'} V_{ij} + \frac{\mathbf{C}'}{\mathbf{A}'} U_{ij} - \frac{\mathbf{D}'}{\mathbf{A}'} U_{ij+1} \qquad (4.17)$$

where,

$$\mathbf{A}' = \frac{1}{4} (D_{ij} + D_{i+1j}) (\Delta s_{i+1j-1} + \Delta s_{i+1j} + \Delta s_{ij-1} + \Delta s_{ij}) \qquad (4.18a)$$

$$\mathbf{B}' = \frac{1}{4} (D_{ij} + D_{i-1j}) (\Delta s_{ij-1} + \Delta s_{ij} + \Delta s_{i-1j-1} + \Delta s_{i-1j}) \qquad (4.18b)$$

$$\mathbf{C}' = (D_{ij} + D_{ij-1}) \Delta n \qquad (4.18c)$$

$$\mathbf{D}' = (D_{ij} + D_{ij+1}) \Delta n \qquad (4.18d)$$

In computing the transverse velocity V from (4.17), the impermeability of channel walls to lateral water flow is imposed as an extra boundary condition.

4.3.4 Discretization of Sediment Continuity Equation

Sediment continuity equation (4.6d) is discretized using the staggered grid shown in Fig. 4.4. This equation is written in finite difference form as follows:

$$\eta'^{\,n+1}_{ij} = \eta'^{\,n}_{ij} - \frac{\Delta t}{(1-p)\,\Delta s_{\bullet}\,\Delta n}\left[\Delta n\,(Q_s{}^{n}_{ij+1} - Q_s{}^{n}_{ij}) + (\Delta s_{\bullet 1}\,Q_n{}^{n}_{i+1j} - \Delta s_{\bullet 2}\,Q_n{}^{n}_{ij})\right] \qquad (4.19)$$

with,

$$\Delta s_{\bullet} = \frac{1}{2}\,(\Delta s_{ij} + \Delta s_{ij-1}) \qquad (4.20a)$$

$$\Delta s_{\bullet 1} = \frac{1}{4}\,(\Delta s_{ij} + \Delta s_{i+1j} + \Delta s_{ij-1} + \Delta s_{i+1j-1}) \qquad (4.20b)$$

$$\Delta s_{\bullet 2} = \frac{1}{4}\,(\Delta s_{ij} + \Delta s_{i-1j} + \Delta s_{ij-1} + \Delta s_{i-1j-1}) \qquad (4.20c)$$

where the superscripts n and n+1 in (4.19) denote time level. In solving (4.19), the impermeability of channel walls to transverse sediment transport is imposed as an extra boundary condition. The values of the sediment transport rate components Q_s and Q_n are evaluated using equations (4.9), (4.10) and (4.11) presented above.

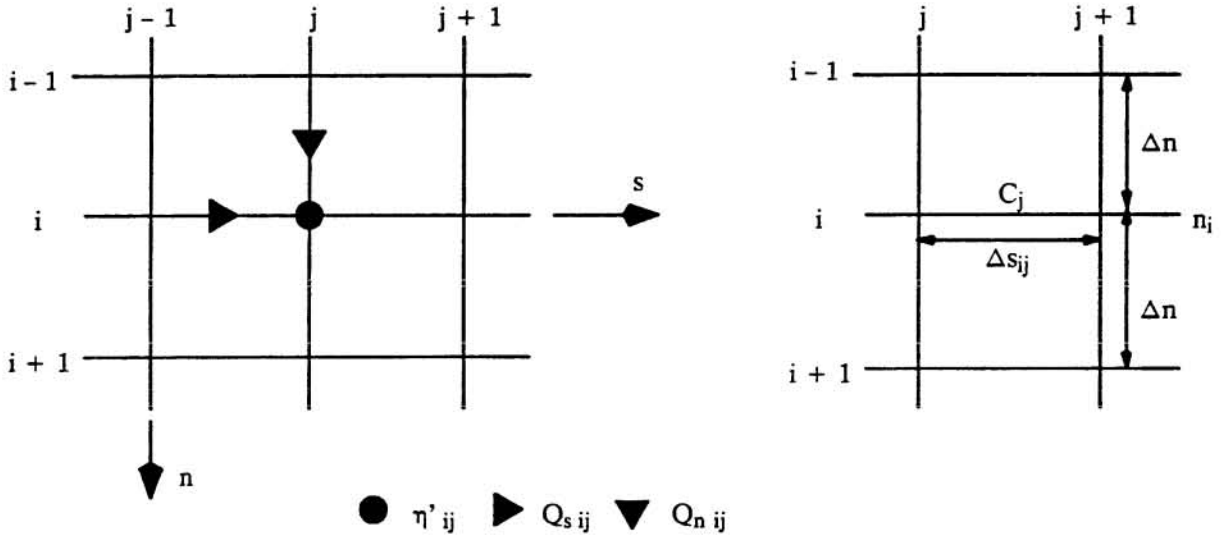

Fig. 4.4 Staggered Grid used by the Numerical Scheme.

4.4 Numerical Simulation of Flow in Curved Channel

With the objective of checking the reliability of the numerical model described above in the simulation of two-dimensional flow in curved channels with fixed bed, a comparison between the results obtained from the application of the model with the classic experimental results of Rozovskii (1957) is presented next.

The experimental setup corresponds to a fixed bed rectangular channel having a width of 0.8 m and describing a 180° curve with a radius of curvature of 0.8 m. The water discharge is 12.3 l/s and the slope of the channel is zero. Fig. 4.5 presents the numerical results for the velocity distribution along the channel axis at different cross sections obtained for values of $\Delta x = 0.25$ m and $\Delta y = 0.1$ m, together with the corresponding experimental measurements made by Rozovskii. Fig. 4.6 shows the numerical results obtained in terms of the values of water depth along three different axis along the channel, namely left wall, centerline and right wall, plotted together with the corresponding experimental results of Rozovskii.

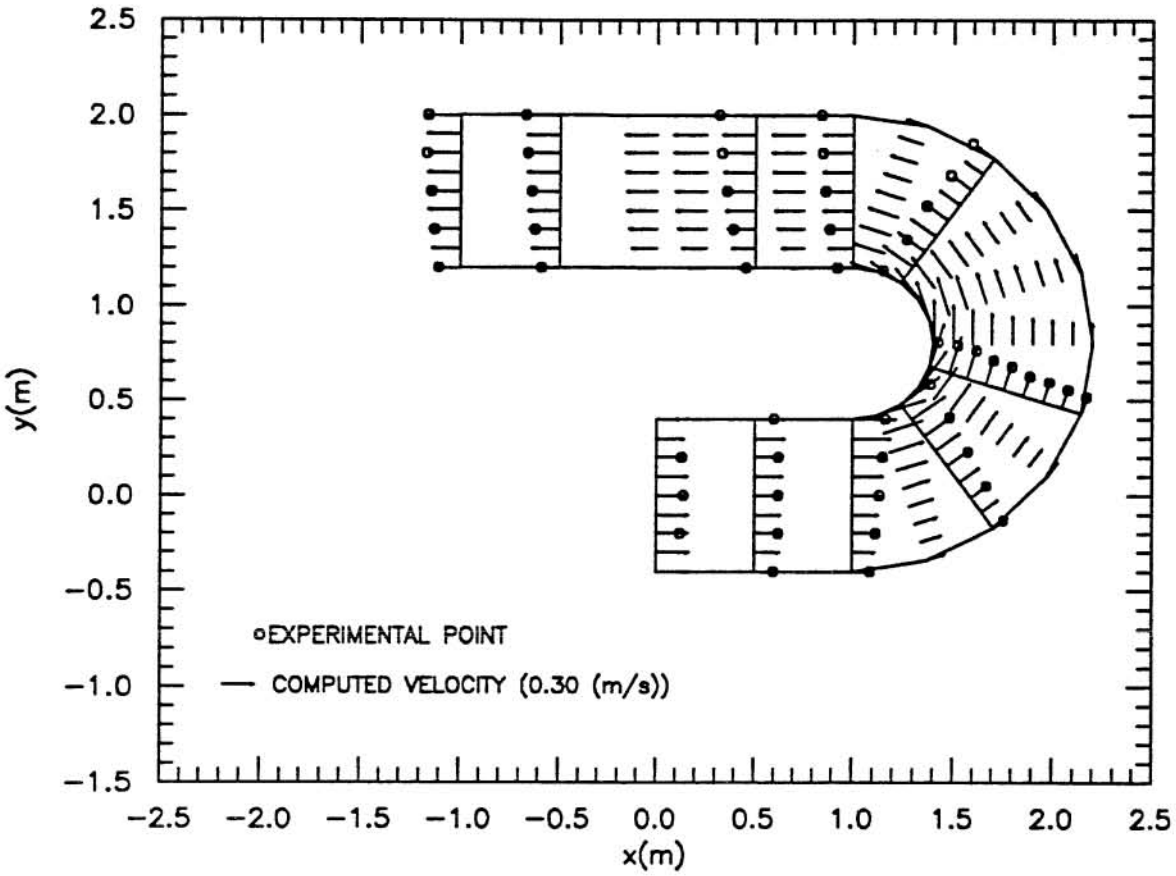

Fig. 4.5 Numerical Results for Flow in Curved Channel. Comparison with Rozovskii's Experiment.

A general good agreement between simulated and observed velocity distributions is apparent from Fig. 4.5. Maximum differences are observed for the velocities at the inner wall in the zone of the curve, which tend to be overestimated by the numerical model. In spite of those differences, the simplified model utilized in the simulation appears to reproduce adequately the general tendencies of the observed velocity distribution, such as the lag in the response to the forcing effect of the curvature. From Fig. 4.6, it can be concluded that the

model also reproduces adequately the water depth variation along the centerline and right wall of the channel, however it does not predict accurately the water depths along the left wall of the channel. In fact, the model tends to overestimate the depression of the water surface in the inner part of the curve thus generating smaller values of the flow depth in that zone than those observed in the experiments. This defect can be attributed to the use of the simplified form of the transverse momentum equation (4.7), which is valid for small channel curvatures, such as those of incipient meanders in alluvial channels. From this point of view, Rozovskii's experiment constitutes a severe test to the numerical model developed herein. As a matter of fact, the dimensionless curvature parameter ν, defined as $\nu = C_{max}B/2$, takes the value $\nu = 0.25$ for Rozovskii's experiment, while for incipient meanders this parameter usually takes values in the range $\nu < 0.05$ (Colombini et al., 1990).

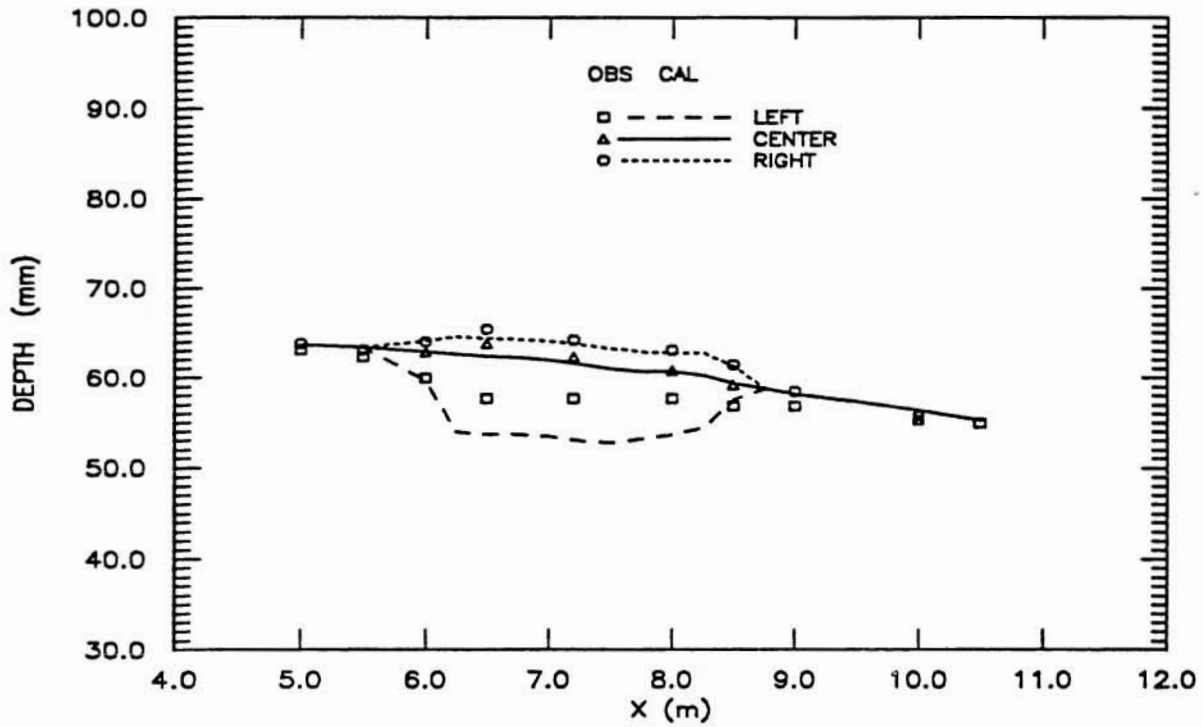

Fig. 4.6 Numerical Results for Flow in Curved Channel. Comparison with Rozovskii's Experiment.

From the results presented above, it can be expected that for small values of ν, such as those characteristic of incipient meanders, the curvature by itself does not perturb the flow field sensibly from the uniform flow conditions. Nevertheless, as it has been observed in experimental and analytical studies, that perturbation appears to be large enough as to trigger the bed deformation process, which, as a feedback, becomes the main agent driving the flow field deformation in those channels.

4.5 Numerical Simulation of Flow and Bed Deformation in Meandering Channels

In this section some numerical results obtained from the application of the model to the simulation of flow and bed deformation in meandering channels are presented. One meandering channel configuration and different flow conditions are used in the simulation, such that all parameters are set as to reproduce corresponding experimental conditions fixed in the laboratory experiments made as part of the research work reported herein. In this fashion an easy comparison between numerical and experimental results is possible, although such comparison will be presented in following chapters. Herein, just the main characteristics of the flow and bed responses as predicted by the numerical model are presented.

As it is pointed out by Johannesson and Parker (1987), Langbein and Leopold (1966) showed that the geometry of natural meanders often closely resembles a sine-generated curve. Such curve has been used subsequently in numerous analytical and experimental studies modeling meandering channels. In the present analysis, however, just a purely sinusoidal channel axis is used, since such geometry was used, for simplicity, to build the channels utilized in the laboratory experiments made as part of the present investigation. The equation for the channel axis is expressed in cartesian coordinates as:

$$y = a\,B\,\sin\left(\lambda\,\frac{x}{B}\right) \qquad (4.21)$$

with,

$$a = \frac{a_*}{B} \quad , \quad \lambda = \frac{2\,\pi\,B}{L_m} \qquad (4.22a, b)$$

where a_* denotes the maximum amplitude of the channel centerline and L_m represents the meander wavelength measured along the x axis. For this channel the curvature C can be written as a function of x in the form:

$$C = a\,\frac{\lambda^2}{B}\,\sin\left(\lambda\,\frac{x}{B}\right)\left(1 + a^2\,\lambda^2\,\cos^2\left(\lambda\,\frac{x}{B}\right)\right)^{-\frac{3}{2}} \qquad (4.23)$$

from where the maximum curvature of the channel axis can be expressed in dimensionless form as:

$$\nu = C_{max}\,\frac{B}{2} = \frac{a\,\lambda^2}{2} \qquad (4.24)$$

As it is deduced from the set of equations presented above, the geometry of the meandering channel is totally described by the parameters B, λ and ν. In the applications selected herein, the meandering channel denoted as Channel 1 in the experimental work reported in following chapters is utilized, whose values of λ and ν are presented in Table 4.1.

The channel has a width $2B = 0.4$ m, a slope $S_0 = 0.005$ and is covered by a uniform sediment of $d_s = 0.5$ mm. For this channel different flow conditions are simulated by fixing the water discharge at values in the range from 1.0 to 3.0 l/s. Values of $\Delta x = 0.30$ m and $\Delta y = 0.05$ m were used in the simulation.

Figs. 4.7 to 4.12 present some of the results obtained from the application of the numerical model to the conditions specified above. The results shown in those figures correspond to the conditions defined by a water discharge of 2.9 l/s, however they can be taken as representative of all of the cases modeled, since they allow to describe in general terms the main characteristics of the flow and bed deformation as predicted by the numerical model. Values of $r = 0.3$ and $n_m = 0.0184$, this last parameter calibrated from the experimental results presented in next chapter, were used in those computations. Only equilibrium results are presented, associated with the steady state of the bed deformation.

Table 4.1 Geometry of Meandering Channel utilized in the Numerical Analysis.

CHANNEL	λ	ν	B (m)
1	0.20	0.030	0.20

Fig. 4.7 presents the results obtained in terms of the velocity distribution at different cross sections along one wavelength of the meandering channel. As it can be observed therein, the zone of maximum velocity tends to be located at the outer wall with respect to the curves of the channel. There exists a lag between the section of maximum curvature and the section at which a maximum deformation of the velocity profile is attained. The latter is also the zone at which the maximum velocity occurs and as it will be shown later is also the zone of maximum scour of the channel bed. Although the velocity vector is plotted in Fig.4.7, very small deviation of the arrows from the axial direction can be detected, thus indicating a small magnitude of the depth-averaged transverse velocity component. For the particular application shown in that figure the maximum depth-averaged transverse velocity is about 10% of the mean depth-averaged axial velocity. In spite of their small magnitude, transverse depth-averaged velocity components are observed to be directed towards the outer bank with respect to the curvature of the channel.

Fig. 4.8 shows longitudinal profiles of the water surface elevation along three different axes taken over one wavelength of the channel, namely left wall, centerline and right wall. The water surface elevation, H, was made dimensionless with the uniform flow depth, D_0. Likewise, the axial coordinate s was made dimensionless with the wavelength of the channel, L, measured along the channel centerline. As it can be observed in that figure, H/D_0 oscillates around 1.0 along the three longitudinal axis considered, such that the oscillations

are lagged with respect of each other. In other words, the maximum overelevation at the outer wall does not occur in the same section than the maximum underelevation at the inner wall. For the particular application shown in Fig. 4.8, a lag equivalent to about 20% of the channel wavelength between those sections is obtained.

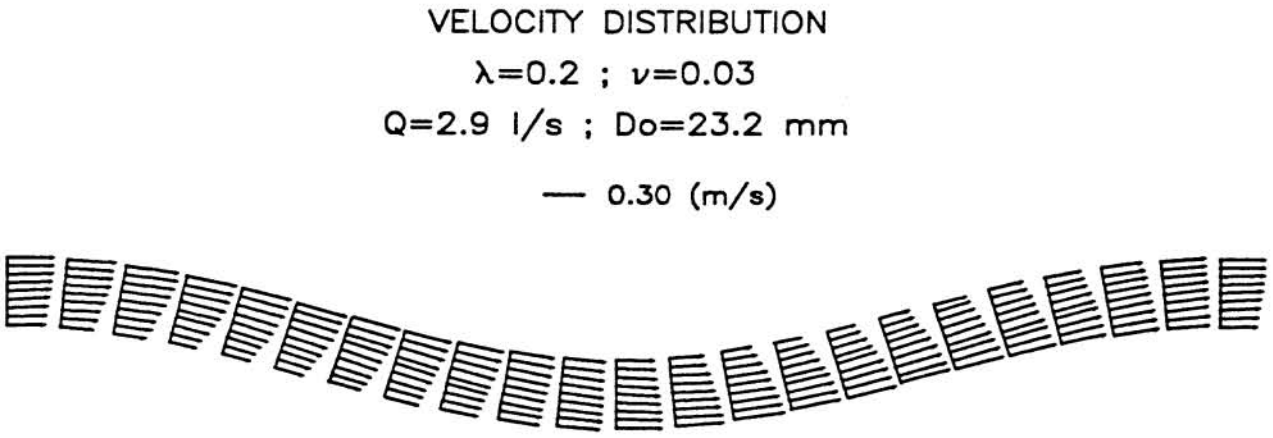

Fig. 4.7 Velocity Vector Distribution in Channel 1. Numerical Simulation.

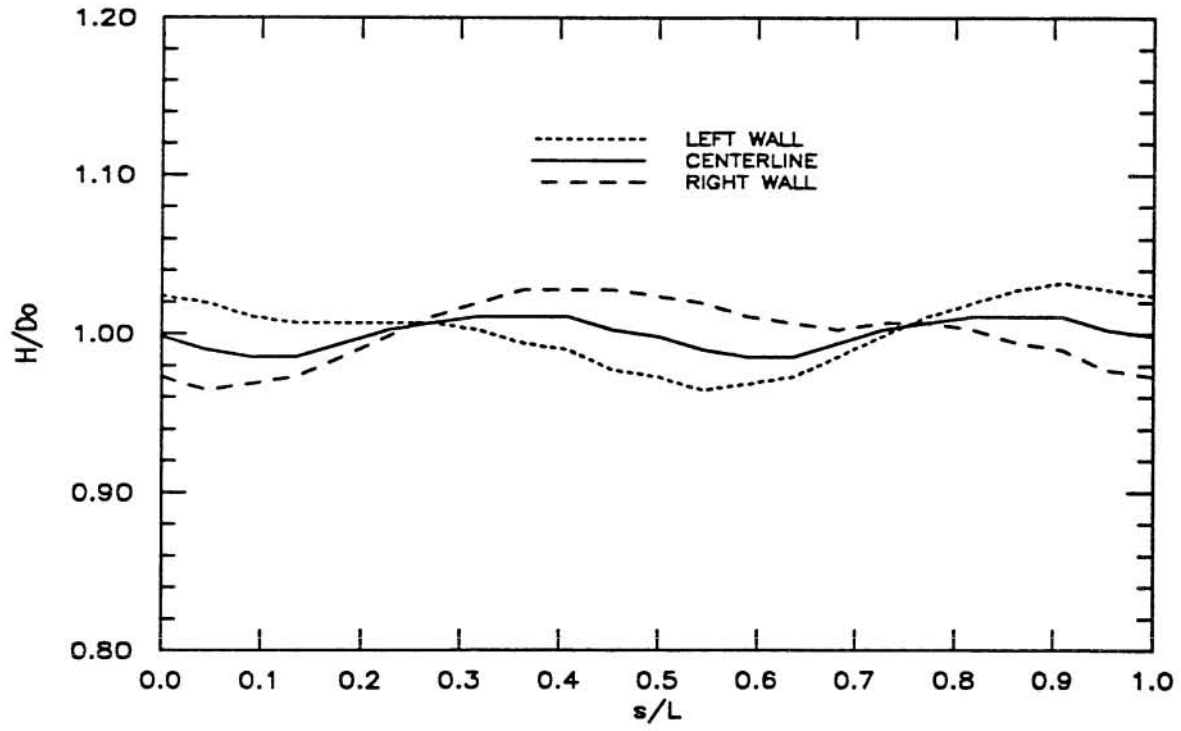

Fig. 4.8 Longitudinal Profile of Dimensionless Water Surface Elevation in Channel 1. Numerical Simulation.

Also from Fig. 4.8, it can be noticed that the maximum values of the over and under elevation within the same curve of the channel are equal in magnitude, and that for the particular application shown in that figure such values are on the order of 4% of the uniform flow depth.

Fig. 4.9 shows the total bedload vector at different cross sections along one wavelength of the meandering channel. As it can be observed in that figure the zones of maximum bedload transport are located at the outer wall with respect to the curvature of the channel, some distance downstream the apex, and coincident with the sections of maximum velocity as observed in Fig. 4.7. The deformation of the bedload profile in Fig. 4.9 is more evident than that of the flow velocity shown in Fig. 4.7, having a very small value at the inner wall in the zone of maximum deformation. As it also happens with the flow velocity distribution, the bedload distribution is almost uniform at the apex of the channel curves. Very small deviation of the arrows from the axial direction can be noticed in Fig. 4.9, thus indicating a small magnitude of the transverse component of the bedload, which however point towards the outer bank with respect to the curves of the channel. For the particular application shown in this figure the maximum transverse bedload rate is about 10% of the mean value of the bedload in the axial direction.

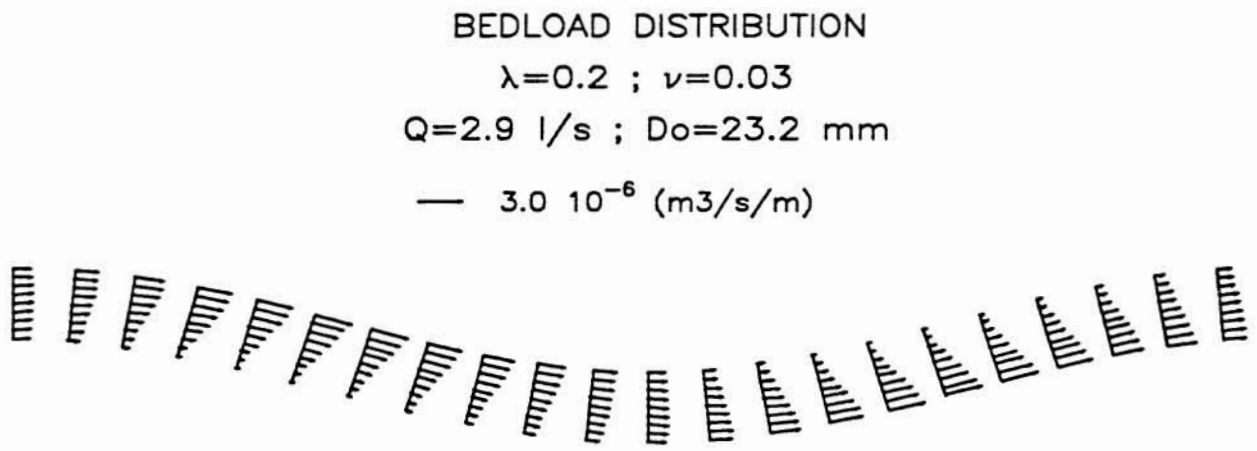

Fig. 4.9 Bedload Vector Distribution in Channel 1. Numerical Simulation.

Fig. 4.10 presents longitudinal profiles of the bed deformation along three different axes taken over one wavelength of the meandering channels, namely left wall, centerline and right wall. The bed elevation, η', was made dimensionless with the uniform flow depth, D_0. Likewise, the axial coordinate s was made dimensionless with the wavelength of the channel, L, measured along the channel centerline. Different distinctive features of the calculated bed

deformation are apparent from that figure. In the first place, a bar-like deformation is observed, formed by successive zones of scour, which tend to be located at the outer wall with respect to the curve, and deposition, which tend to be located at the inner wall with respect to the curve. The section of maximum deposition coincides with the section of maximum scour, and is located some distance downstream the apex of the channel curves, which for the particular application shown therein is equivalent to about 10% of the meander wavelength. This section also coincides with the sections of maximum velocity, as observed in Fig. 4.7 and maximum bedload, as observed in Fig. 4.9.

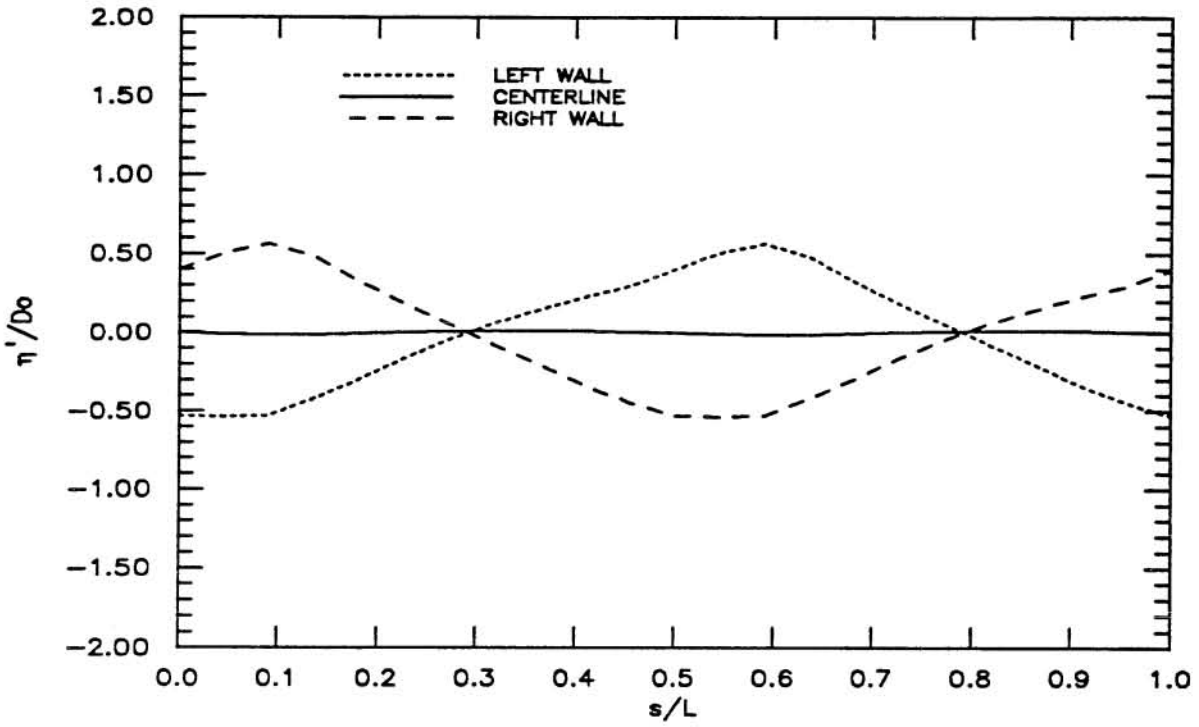

Fig. 4.10 Longitudinal Profile of Dimensionless Bed Elevation in Channel 1. Numerical Simulation.

The magnitude of the maximum deposition in Fig. 4.10 appears to be equal to the magnitude of the maximum scour, thus defining a very symmetric bed deformation with respect to the channel axis. This result of the numerical model does not seem to be in agreement with experimental observations, for example with those of Colombini et al. (1990) who describe less symmetrical structures, and appears to be one of its shortcomings. The improvement of this feature, however, would require an improvement in the modeling of the direction and magnitude of the sediment transport in the meandering channel, which as was discussed before is one of the crucial aspects of the model.

In the particular application shown in Fig. 4.10, the bar height, defined as the sum of the maximum scour and the maximum deposition within a wavelength of the channel, has a value of about 1.2 times the uniform flow depth. The behavior of this parameter with flow conditions is explored and discussed later in this section.

Fig. 4.11 presents a cross sectional plot of the bed deformation at the zone of maximum scour together with the water surface elevation at the same section. This figure reinforces the picture discussed above about the transverse symmetry of the bed deformation predicted by the model. Also, Fig. 4.11 gives an idea on how small is the magnitude of the transverse slope of the water surface elevation, as compared with the depth of flow and bed deformation, for the particular meandering channel configuration simulated herein. As it can be deduced from the simplified form of the transverse momentum equation, eq.(4.7), this slope is controlled mainly by the curvature of the channel, such that it is zero in absence of curvature. This demonstrates that for small values of the channel curvature, such as the one used in the simulation presented here, the curvature by itself does not deform sensibly the flow field from the uniform flow conditions. On the contrary it acts in a more subtle way, by providing the conditions for the bed deformation which is the agent that more markedly alters the flow conditions.

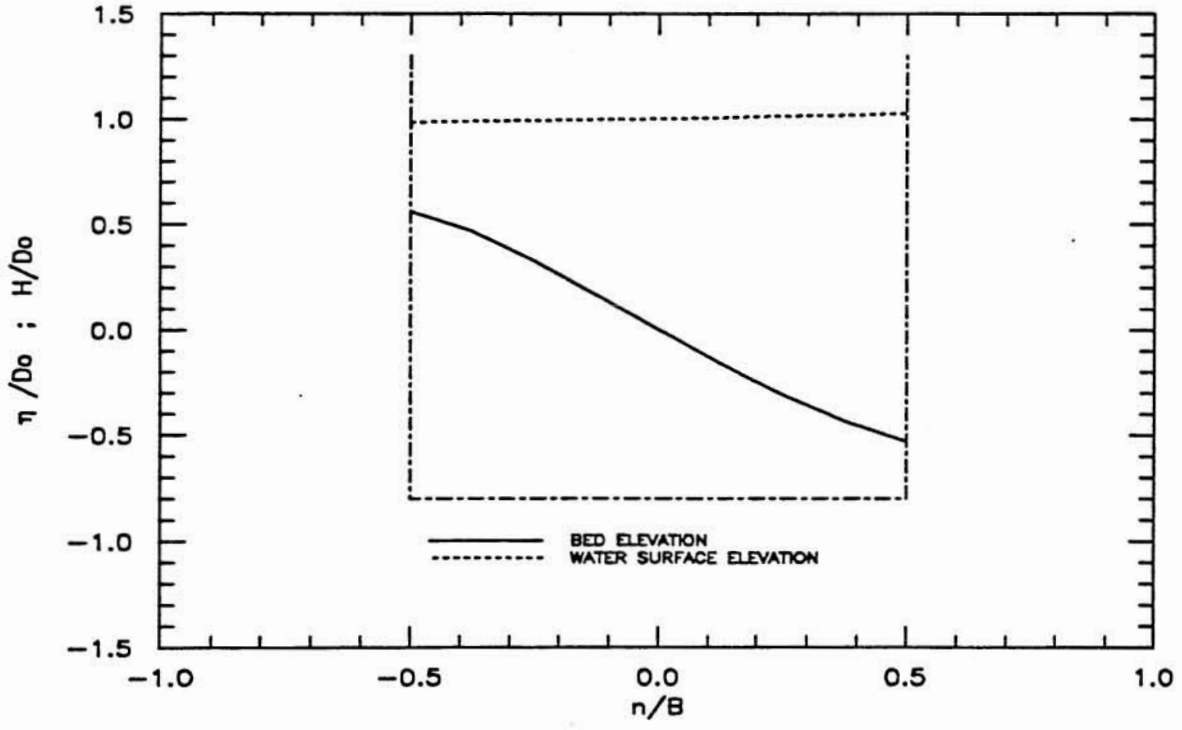

Fig. 4.11 Transverse Profile of Bed and Water Surface Elevations in Channel 1. Numerical Simulation.

In order to complete the description of the bed deformation predicted by the model for the particular conditions described above, Fig. 4.12 shows a three-dimensional plot of the computed bed elevations within one wavelength of the channel. This figure does not show the curvature of the channel, however the apex of the curves are marked with arrows. Likewise, the scales in the figure are distorted in order to amplify the magnitude of the bed deformation. As it can be observed therein, the three-dimensional plot summarizes the bed deformation information presented in Figs. 4.10 and 4.11, helping to visualize in better shape some of the aspects already discussed, such as the lag in the response of the bed with respect to the apex of the curves and the symmetry of the bar structure as predicted by the model.

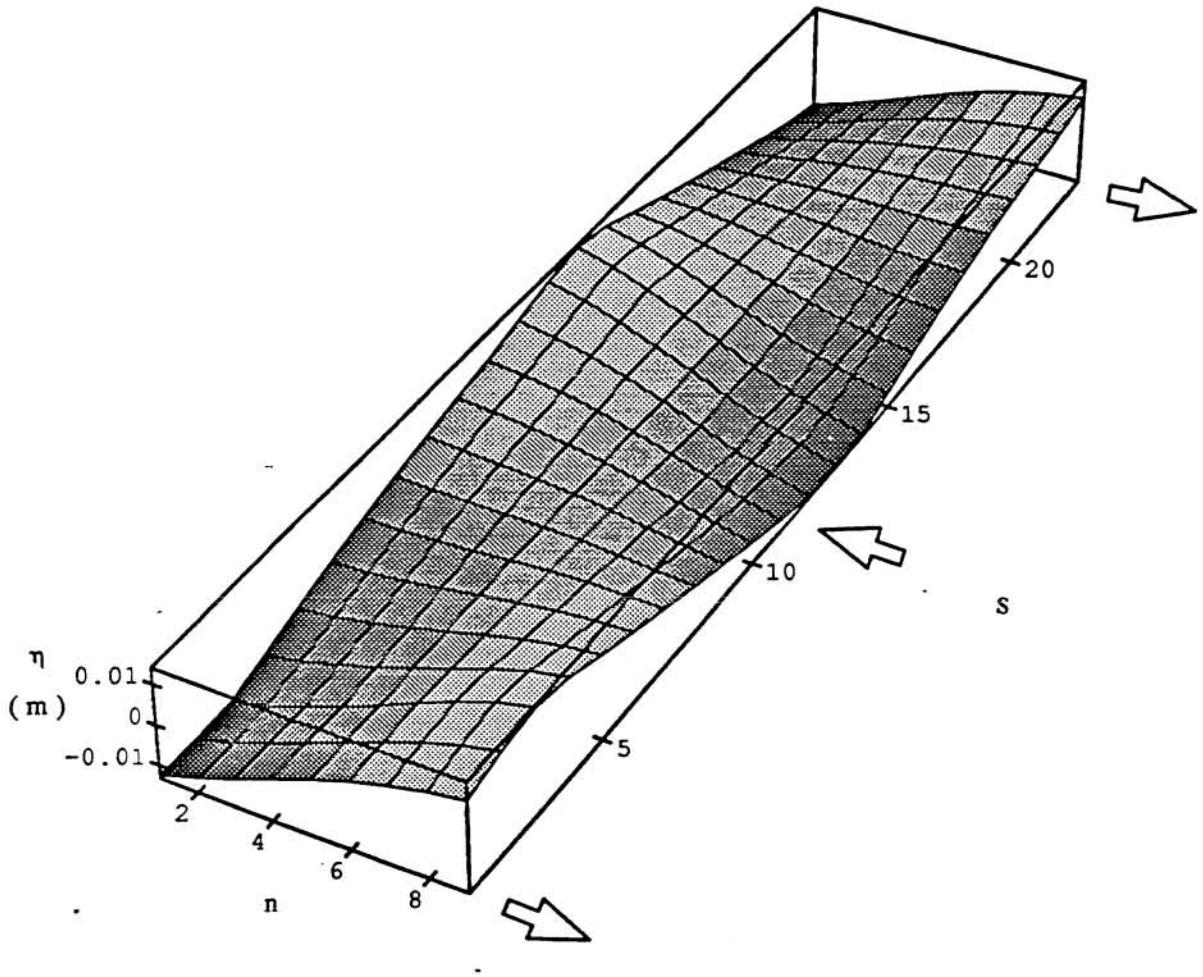

Fig. 4.12 Three-dimensional Plot of Bed Deformation in Channel 1. Numerical Simulation.

Finally, the influence of flow parameters, such as the channel width to depth of flow ratio, over the bed response is analyzed in Fig. 4.13. To build this figure, different flows

discharges varying in the range 1.0 to 3.0 l/s were simulated for the channel configuration corresponding to Channel 1. The figure shows the bar height, H_B, defined as the sum of the maximum scour and maximum deposition within one wavelength of the channel, made dimensionless with the uniform depth D_0, plotted as a function of the parameter β, defined as $\beta = B/D_0$. As it can be observed in Fig. 4.13, the bar height tends more or less asymptotically to a constant value of about 1.5 times the uniform flow depth as β increases over 15, whereas for values of β less than 10 it tends to decrease with a steeper slope towards values of bar height smaller than the uniform flow depth. This particular behavior of the bed deformation will be further examined with the help of experimental data, in following chapters.

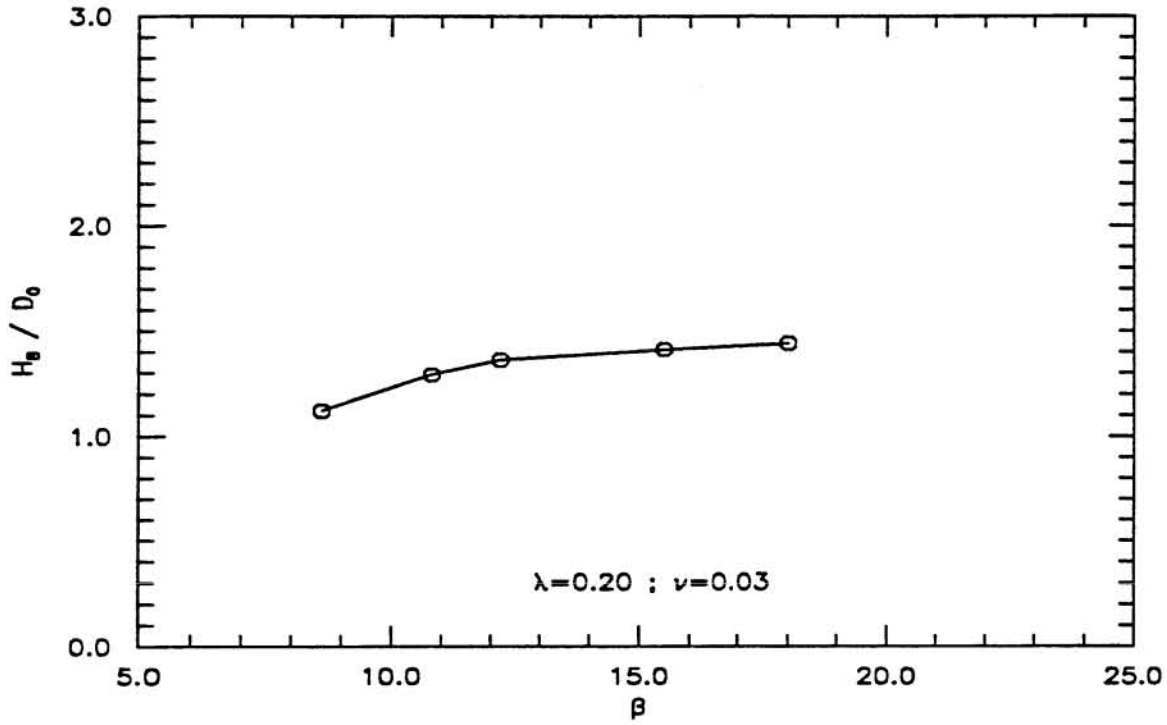

Fig. 4.13 Dimensionless Bar Height as a function of β in Channel 1. Numerical Simulation.

Since a very limited range of flow variables and channel configurations were considered, the analysis of the results obtained with the numerical model developed in the present section is by no means exhaustive. However, this exercise allowed to get some insight on the principal characteristics of the different physical processes involved in the flow and bed deformation phenomena in meandering channels. A comparison of some of the results obtained from the application of the model with experimental results obtained in the laboratory experiments made as part of the present research is reported in following chapters.

5. EXPERIMENTAL STUDY

5.1 Introduction

The main objective of the experimental study conducted as part of the research work reported herein, was to provide empirical evidence for the verification of specific aspects of recently developed analytical theories on the alternate bar and meander phenomena. In this chapter, descriptions of the experimental plan, the laboratory facilities, and the methodologies utilized in the study are presented, together with a dimensional analysis of the problem.

5.2 Dimensional Analysis

In the preceding chapter different forms of the set of governing equations commonly used in analytical and numerical studies of the flow and bed deformation problem in meandering channels were presented. In what follows the system of governing equations (4.2) is made dimensionless with the aim of identifying dimensionless parameters involved in such problem. The dimensionless form of (4.2) can be written as:

$$U\frac{\partial U}{\partial s} + V\frac{\partial U}{\partial n} + \frac{1}{R+n}UV = -\frac{1}{F_0^2}\left(\frac{\partial D}{\partial s} - \beta S_0 + \frac{\partial \eta'}{\partial s}\right) - \beta\frac{\tau_s}{D} \qquad (5.1a)$$

$$U\frac{\partial V}{\partial s} + V\frac{\partial V}{\partial n} - \frac{1}{R+n}U^2 = -\frac{1}{F_0^2}\left(\frac{\partial D}{\partial n} + \frac{\partial \eta'}{\partial n}\right) - \beta\frac{\tau_n}{D} \qquad (5.1b)$$

$$\frac{\partial(UD)}{\partial s} + \frac{1}{R+n}\frac{\partial((R+n)VD)}{\partial n} = 0 \qquad (5.1c)$$

$$\frac{\partial \eta'}{\partial t} + Q_0\left(\frac{\partial Q_s}{\partial s} + \frac{1}{R+n}\frac{\partial((R+n)Q_n)}{\partial n}\right) = 0 \qquad (5.1d)$$

where (U,V) are dimensionless depth averaged velocity components in the s and n directions respectively, τ_s and τ_n are dimensionless bottom shear stresses, D is dimensionless local depth, η' is dimensionless bed elevation, S_0 is the slope of the channel, Q_s and Q_n are dimensionless bedload components, F_0 is the Froude number of the mean flow, and R is the dimensionless local radius of curvature of the channel. In 5.1, Q_0 and β are dimensionless parameters defined as:

$$Q_0 = \frac{d_s^*\left((\varrho_s/\varrho - 1)\, g\, d_s^*\right)^{\frac{1}{2}}}{(1-p)\, D_0^*\, U_0^*} \quad , \quad \beta = \frac{B^*}{D_0^*} \qquad (5.2a, b)$$

where ρ_s and d_s^* are density and diameter of the uniform sediment, ρ is water density, g is gravitational acceleration, p denotes sediment porosity, and B^* is half the channel width.

Likewise, D_0^* is flow depth averaged over one wavelength of the meandering channel and U_0^* is the mean flow velocity defined as: $U_0^* = Q/(2B^*D_0^*)$, where Q denotes flow discharge.

In (5.1) the variables have been made dimensionless in the form:

$$(U^* , V^*) = U_0^* (U , V) \quad , \quad (\eta'^* , D^*) = D_0^* (\eta' , D) \qquad (5.3a, b)$$

$$(s^* , n^*) = B^* (s , n) \quad , \quad (\tau_s^* , \tau_n^*) = \varrho \, U_0^{*2} (\tau_s , \tau_n) \qquad (5.3c, d)$$

$$(Q_s^* , Q_n^*) = d_s^* \left(\left(\varrho_s/\varrho - 1 \right) g \, d_s^* \right)^{\frac{1}{2}} (Q_s , Q_n) \qquad (5.3e)$$

$$R^* = B^* R \quad , \quad t^* = \frac{B^*}{U_0^*} t \qquad (5.3f, g)$$

where the superscript * denotes dimensioned variables.

From (5.1), the following dimensionless relationship can be written between dependent and independent variables:

$$(U , V , D , \eta') (s,n,t) = f_0 (R , F_0 , S_0 , \beta , \tau_s , \tau_n , Q_0 , Q_s , Q_n) \qquad (5.4)$$

However, by using closure relationships for sediment transport and resistance to the flow such as those specified in chapter 3, for instance, equations (3.4), (3.5), (3.6) and (3.7), τ_s, τ_n, Q_s and Q_n can be expressed in terms of the following dimensionless relationships:

$$(\tau_s , \tau_n) = \mathrm{T} (U , V , D , d_s , \theta) \qquad (5.5a)$$

$$(Q_s , Q_n) = Q (U , V , D , \eta' , d_s , \theta , \beta) \qquad (5.5b)$$

where d_s denotes dimensionless sediment diameter defined as $d_s = d_s^*/D_0^*$ and θ denotes the Shields parameter of the flow defined as in (3.5c). This parameter can be expressed in terms of the slope of the channel such that:

$$\theta = \frac{D \, S_0}{\left(\varrho_s/\varrho - 1 \right) d_s} \qquad (5.6)$$

Also, Q_0 can be rewritten in the form:

$$Q_0 = \frac{\left(\varrho_s/\varrho - 1 \right)^{\frac{1}{2}} d_s^{\frac{3}{2}}}{(1-p) F_0} \qquad (5.7)$$

Finally, the local dimensionless radius of curvature R is in general a function of the coordinates (s,n), which is completely defined by specifying the shape of the channel axis. If the particular equation of the channel axis given by (4.21) is used, then the dimensionless radius of curvature can be represented by the relation:

$$R(s, n) = R(\lambda_m, \nu) \qquad (5.8)$$

with,

$$\lambda_m = \frac{2\pi B^*}{L_m^*} \quad , \quad \nu = C_{max}\frac{B^*}{2} \qquad (5.9a, b)$$

where L_m^* denotes meander wavelength and C_{max} denotes the maximum curvature of the channel axis.

Therefore, using relationships (5.5), (5.6), (5.7) and (5.8), expression (5.4) can be rewritten as:

$$(U, V, D, \eta')(s,n,t) = f_1(\lambda_m, \nu, \varrho_s/\varrho, p, F_0, d_s, \theta, \beta) \qquad (5.10)$$

or alternatively as:

$$(U, V, D, \eta')(s,n,t) = f_2(\lambda_m, \nu, \varrho_s/\varrho, p, F_0, d_s', S_0, \beta) \qquad (5.11)$$

where $d_s' = B^*/d_s^*$.

In (5.11), selecting the sediment and the channel width such that ρ_s/ρ, p and d_s' are fixed, selecting the channel configuration such that λ_m and ν are fixed, and also fixing the slope of the channel S_0, the following dimensionless relation results:

$$(U, V, D, \eta')(s,n,t) = f_3(F_0, \beta) \qquad (5.12)$$

where F_0 and β depend basically on the flow discharge for all the other parameters fixed. This relation can be further simplified by assuming that F_0 does not change significantly within the experimental range of values of this parameter, such that,

$$(U, V, D, \eta')(s,n,t) = f_4(\beta) \qquad (5.13)$$

Equation (5.13) can be used particularly to express different variables characterizing the bed deformation $\eta'(s,n,t)$, for given sediment, channel configuration and slope. For instance, the following relationship can be written:

$$(H_B, S, \lambda, c, \delta) = f_5(\beta) \qquad (5.14)$$

where $H_B = H_B^*/D_0^*$ denotes dimensionless maximum bar height defined as the sum of the maximum scour and maximum deposition given by the bed deformation, $S = S^*/D_0^*$ denotes dimensionless maximum scour, $\lambda = 2\pi B^*/L$ represents a wavenumber such that L is the wavelength of the bed deformation, $c = c^*/U_0^*$ denotes dimensionless celerity of migrating bedforms and $\delta = 2\delta^*/L_m$ is the dimensionless lag between the zone of maximum curvature of the channel and the zone of maximum scour of the bed.

The general validity of (5.14), particularly the fact that F_0 has a negligible effect on the functional dependence described by this equation if it is kept in a relatively narrow range seems to be validated by the experimental results of Ikeda (1984) and Colombini et al. (1990).

Equations (5.10) to (5.14) were used to develop the experimental plan as it is explained below, and also to analyze the experimental results as it is shown in following chapters.

5.3 Experimental Plan

The main objective of the experimental plan is to define a range of values for the parameters involved in the problem, such as those described by (5.11), in order that the resulting experimental conditions allow to effectively observe the phenomena which are to be investigated in the present work.

With the aim of satisfying the specific objectives of the present research, which were explained in detail in Chapters 1 and 2, a straight channel covered by a movable bed of uniform sediment was designed as to allow alternate bars to develop naturally. Also, a set of three different meandering channels derived from the basic straight channel configuration, having the same width and covered by the same sediment, were designed, as to cover conditions ranging from those for which no migrating bars exist in the channel, to conditions for which migrating bars coexist with fixed bars formed in channel curves. Based on what it was discussed in preceding chapters, conditions for the suppression of alternate bars in meandering channels require to cover the resonant range, as described in chapter 3.

From the general dimensionless relationship between dependent and independent variables (5.11), it is concluded that by selecting the channel width and shape and the sediment properties, just three extra parameters need to be specified, namely F_0, S_0 and β, to totally cover the functional dependence described by such equation. Furthermore, due to resistance considerations, once a slope and a flow discharge are selected in a given experiment, automatically F_0 and β take fixed values. Therefore, the parameters that actually need to be specified for the experimental study are channel width and shape, sediment properties and the range of variation of the channel slope and flow discharge.

In general the channel width should be as large as possible as to avoid scale effects, however since the straight and meandering channels used in the present experimental study were built inside of wider laboratory flumes, the selection of the channel width was made based mainly on space requirements.

The threshold conditions for the formation of alternate bars in straight channels depend basically on the critical value of the parameter β, which is a function of θ and d_s as it was discussed in the analysis presented in Chapter 3, such that alternate bars should be

observed to form for values of β in the range $\beta > \beta_c$. An alternative way to determine the range of conditions for the formation of alternate bars is to use Kuroki and Kishi's (1985) phase diagram for bed regime, which was presented in Fig. 2.1. This diagram allows to specify the range of values of β for which alternate bars would form, such that $\beta_{c1} < \beta < \beta_{c2}$, where β_{c1} corresponds to the parameter β_c in the analysis of Chapter 3 and β_{c2} corresponds to the limit conditions for the formation of multiple row bars or braids.

According to what has been explained above, the selection of the alternate bar range of values of β is related to the selection of the slope of the channel and also of the sediment properties. Once the range of values of β is selected, a resistance relationship is needed to relate flow depths to flow discharges. With this aim, the Engelund–Hansen resistance equation (3.5) was used. It is necessary to point out here that recirculating flumes were used in the present experimental study, so that the bed slope can be fixed externally by setting the flume slope, and the sediment transport rate results from the natural transport capacity of the flow. This make the difference with respect to a nonrecirculating flume in which the sediment transport rate is to be fixed and fed externally and the bed slope results from natural adjustments of the flow and sediment transport.

Although typically a sine generated curve has been used to model meandering channels (Langbein and Leopold, 1966), herein, for practical reasons, particularly for simplicity to build the channels, a purely sinusoidal channel shape was used, such as that given by (4.21). This channel, as it is concluded from (5.8), is totally described by specifying the parameters B^*, λ_m and ν. The latter two parameters, which denote the wavenumber and dimensionless maximum curvature of the channel respectively, were selected as to cover conditions ranging from those for which migrating bars coexist with fixed bars, to conditions for which migrating bars are suppressed. The criteria given by Tubino and Seminara (1990) was used to determine the conditions for the suppression of migrating bars. Since this conditions are related to the resonance phenomenon described previously, the graphical relationships presented in Chapter 3 for the resonant range were also utilized.

The ranges of values for the experimental parameters obtained as explained above, however, were taken just as a general guidance because they are precisely what the present study seeks to check. According to that, it should be pointed out here that the definite experimental plan was not completed until most of the experimental work was finished, since the partial results obtained during the study were used as input for the planning of the remaining experiments.

Taking into account all restrictions exposed above, a consistent set of experiments was designed. As it was already explained, one straight channel and three different meandering

channels were used in the experiments. The channel width selected was $2B^* = 0.40$ m, which appears to be a reasonable width as compared with those utilized in similar experimental studies. Colombini et al. (1990), for instance, used a channel width of 0.35 m. On the other hand, just one type of sediment was selected for all experiments, consisting on a natural uniform silica sand having a mean diameter $d_s^* = d_{50} = 0.53$ mm. A sieve analysis of this sediment is presented in Fig. 5.1, which shows that it is in fact fairly uniform, having a standard deviation of $\sigma_g = 1.25$. From the adopted values of the channel width and the mean diameter of the sediment, the resultant value of the dimensionless parameter d_s' defined previously is: $d_s' = 377.4$.

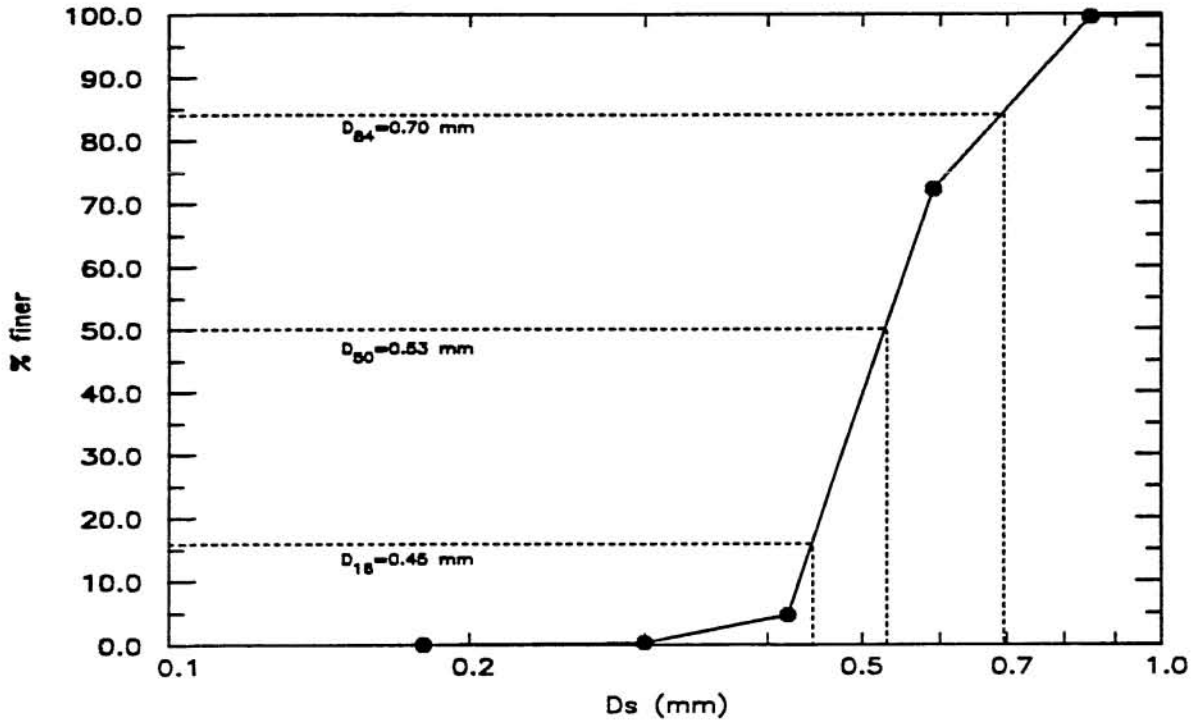

Fig. 5.1 Size Distribution of Experimental Sediment.

The rest of the experimental conditions for the series of experiments made as part of the present research is presented as follows. Table 5.1 shows the geometrical properties of the channels utilized in the study, Table 5.2 presents the experimental conditions for the series of experiments made for the straight channel and finally Table 5.3 specifies the experimental conditions for the series of experiments made in the meandering channels. Tables 5.2 and 5.3 show the slope S_0, the range of values of β and the flow discharge Q utilized in the corresponding experiments. It should be commented here that since in general the experimental conditions defined not so large values of the bottom shear stress, the lower limit

of the range of flow discharges or equivalently the upper limit of the range of β, was given basically by the threshold conditions for the movement of sediment grains.

Table 5.1 Geometry of the Experimental Channels.

CHANNEL	$2B^*$ (m)	L_m^* (m)	C_{max} (1/m)	λ_m	ν
0	0.40	-	0	-	0
1	0.40	6.283	0.30	0.20	0.030
2	0.40	6.283	0.15	0.20	0.015
3	0.40	8.378	0.30	0.15	0.030

Table 5.2 Experimental Conditions in the Straight Channel.

SERIES	CHANNEL	S_0	β	Q (l/s)
01	0	0.0056	9.4 - 26.1	0.75 - 2.98
02	0	0.0044	9.7 - 17.2	1.03 - 2.91
03	0	0.0032	9.0 - 13.2	1.46 - 2.86

Table 5.3 Experimental Conditions in the Meandering Channels.

SERIES	CHANNEL	S_0	β	Q (l/s)
11	1	0.0050	8.6 - 18.0	1.04 - 2.89
12	1	0.0056	10.8 - 18.2	1.03 - 2.45
21	2	0.0050	9.5 - 18.2	1.01 - 2.88
31	3	0.0050	10.2 - 14.7	1.00 - 2.93

In order to provide an idea of the shape of the meandering channels utilized in the study and to allow a comparison among them, about one wavelength of those three channels is shown in Fig. 5.2.

5.4 Description of Experimental Facilities

The experimental study was conducted at the Hydrosystems Laboratory of the University of Illinois at Urbana–Champaign. As it was already explained, the straight and meandering channels utilized in the experiments were built inside of wider tilting flumes. Two different flumes were utilized, one having a width of 0.9 m and a length of about 20 m, and the other having a width of 1.8 m and a length of about 50 m. Both flumes have a mechanism that allows to set slopes ranging from 0 to 2.5% for the large flume, and from 0 to 10% for the smaller one. Also, both flumes possess a hopper to collect sediment near the tail gate, which was utilized to place the sediment traps of the built–in channels. The

straight channel (Channel 0) was built inside the small flume and was given a total length of 14.0 m. The three meandering channels (Channels 1, 2 and 3) were built inside the large flume and were given a total length of about 25.0 m, which corresponds to four wavelengths for Channels 1 and 2, and three wavelengths for Channel 3.

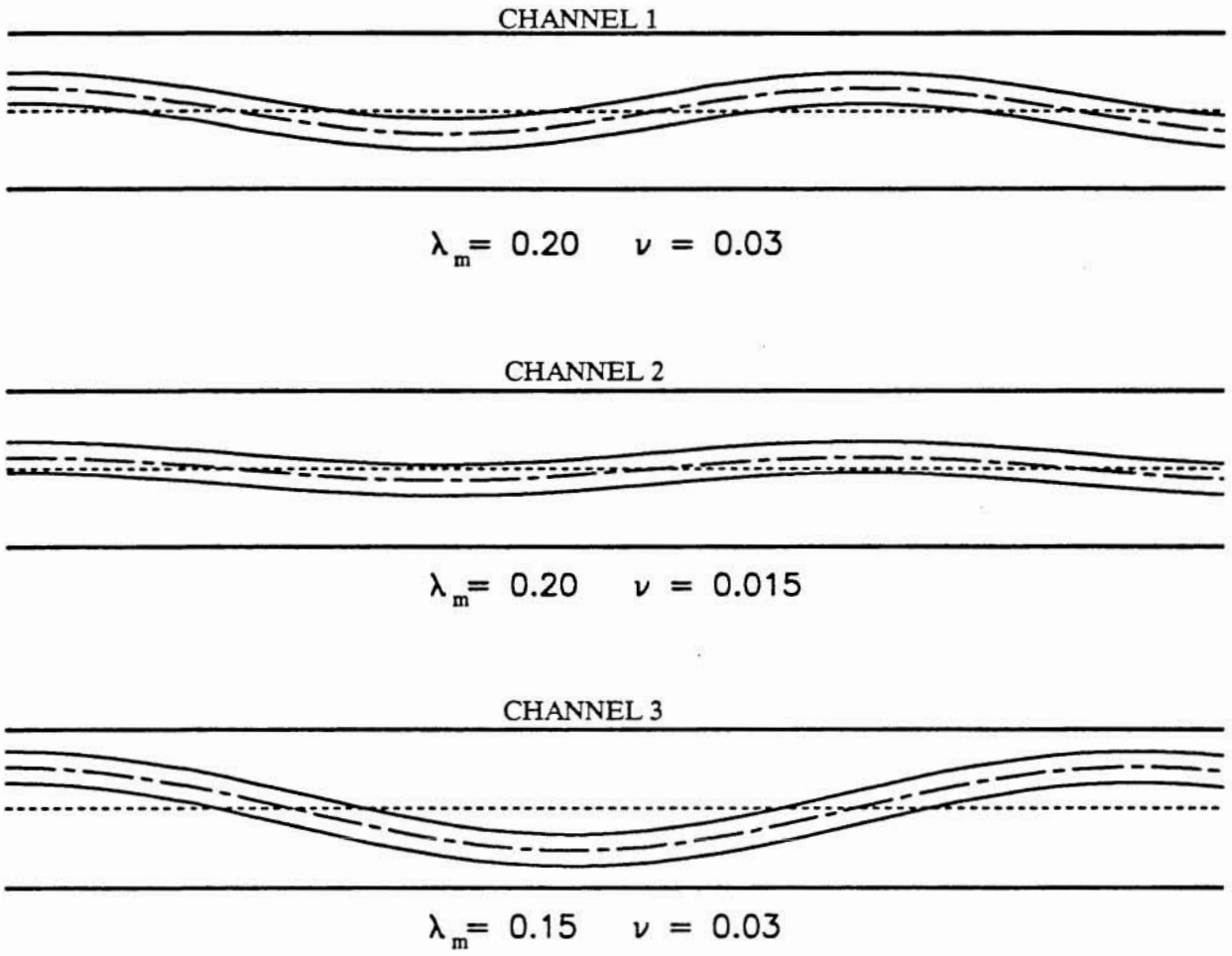

Fig. 5.2 Meandering Channels Used in the Experimental Study.

All four channels were built as recirculating circuits for both water and sediment. A sediment trap was built inside the sediment hoppers of the bigger flumes at the downstream end of the channels. From there, a pipe having a diameter of 2 inches takes the sediment–water mixture, which is carried up with the help of a pump to be fed back into the channel through a manifold installed at the head box of the channels. The sediment hopper of the flumes was filled with water in order to create a pool that helped to stabilize the whole system, and also allowed to control the downstream level of the flow inside the channels. A calibrated venturi–meter was placed in the recirculating lines in order to measure the flow

discharge. A valve located downstream the pump allowed to regulate the required flow discharges. Figs. 5.3 and 5.4 show schematic diagrams of this facilities.

The straight channel was completely made of welded sheet-metal, however, that material was not utilized to build the meandering channels, mainly because of their more complicated shape. In those cases, the side walls were modeled with flexible PVC sheets and placed over a base of plywood sheets. Silicon and duct-tape were used to seal the joint of the walls with the wooden base, while metal brackets were utilized to give rigidity to the channel walls helping to keep them vertical, and also to control width variations along the channels.

A bed of sediment having a thickness of about 10 cm was formed inside the channels, using the silica sand whose size distribution was presented in Fig. 5.1. The bed deformation obtained as the water flows and transports sediment was measured with the help of a bed-profiler (Kenek, model WH-201c). The particular device used in the present investigation allows to measure three quantities, namely the bed elevation with respect to a given datum, the water surface elevation with respect to the same datum and the depth of flow, although not simultaneously. The apparatus consists basically of a detecting rod driven by a motor, which at the operation of a switch gets down to the water surface, to the bed or both, in order to make the required measurement. A digital display shows the measurement in millimeters. Fig. 5.5 presents a photograph of both the detecting device and the control box.

The bed profiler was mounted over a movable and rotating plate which allowed to place the detecting rod at any point inside of the channel. In particular this plate allowed the measurement of the bed deformations along transverse sections which were locally perpendicular to the meandering channels axis. The plate was placed over a trolley which ran along the flumes walls, thus allowing an easy positioning of the bed profiler along the built-in experimental channels.

5.5 Experimental Methodology

This section describes the methods utilized in the realization of the experiments. Basically a given experiment consisted on seven stages, namely, selection of experimental conditions, preparation of the experiment, initiation of the experiment, development of bed deformation, stabilization or equilibrium state of bed deformation, closure of the experiments, and final measurements. In what follows each of those stages is explained in detail.

i) Selection of Experimental Conditions. For each of the series of experiments described in Tables 5.2 and 5.3 the channel configuration and slope were predefined, therefore each of the experiments of the series consisted in a different flow discharge, which was selected as to cover the required range of values of the parameter β. Recall that the flow discharge controls the flow depth, which for a given channel width has direct incidence on the values of β.

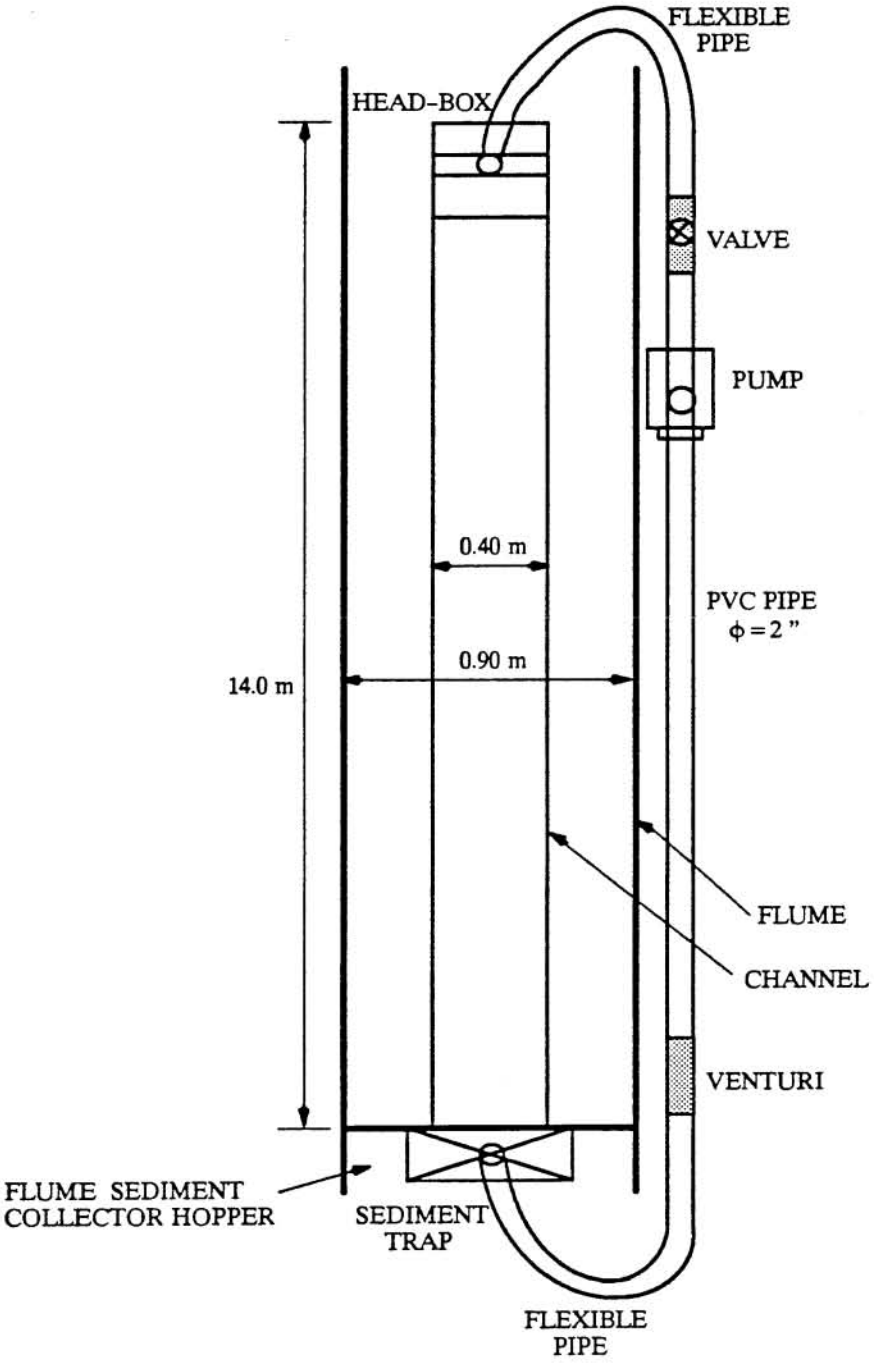

Fig. 5.3 Plan View of Experimental Facility for the Straight Channel Configuration.

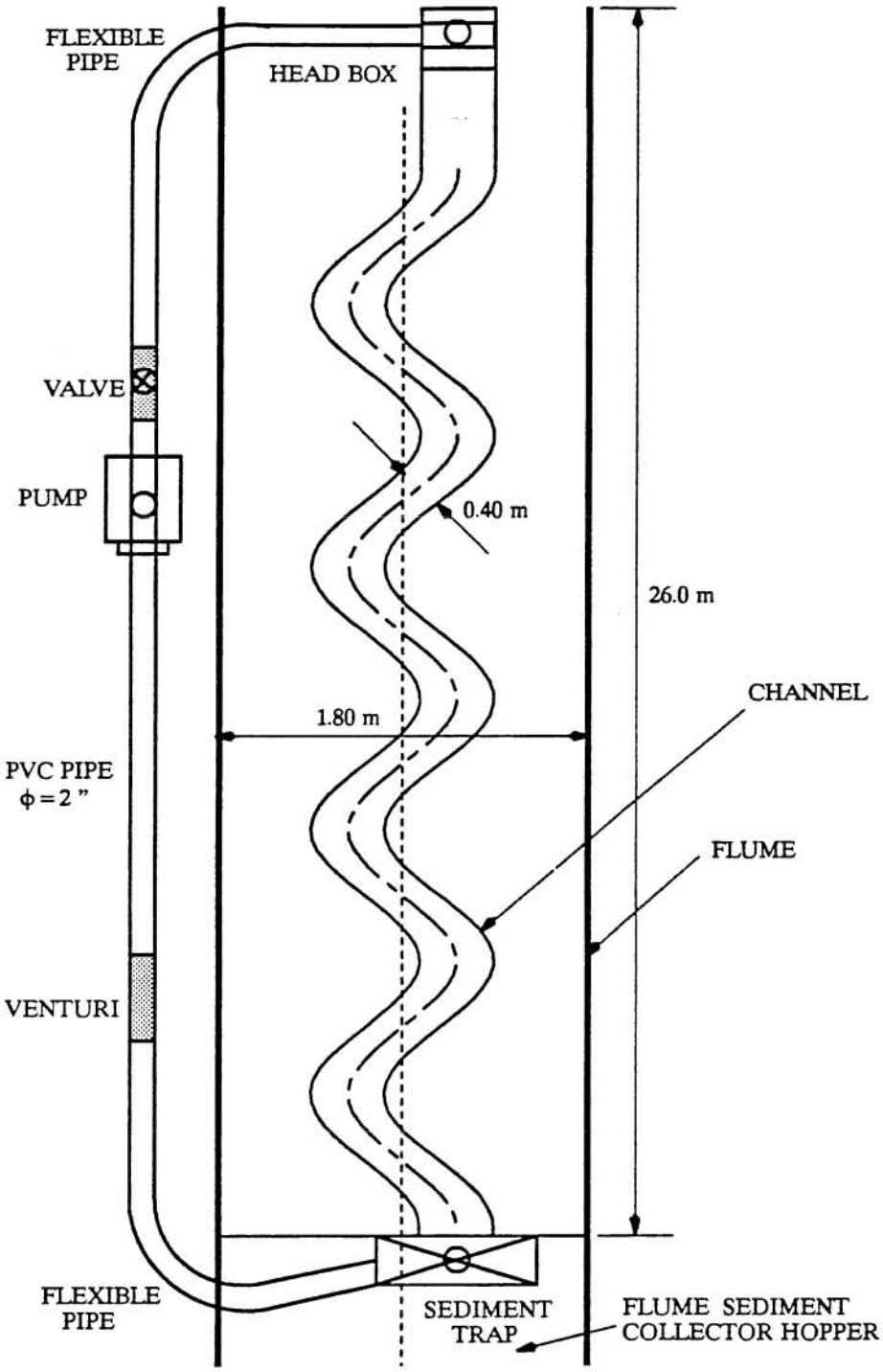

Fig. 5.4 Plan View of Experimental Facility for the Meandering Channel Configuration.

ii) Preparation of the Experiment. Previous to the beginning of the experiments the channel bed was leveled flat by using a scraper with the width of the channel running along its walls. In this way the bed was given a slope identical to the slope of the flume in which the

experimental channel was placed. This slope was controlled by measuring the horizontal surface level of a constant volume of water placed inside the flume with the help of the bed–profiler which ran over the flume walls.

Just before starting the experiments, water was fed into the flume from the downstream end, filling first the hopper in order to create the stabilization pool described before. After the pool was created, water was allowed to run upstream inside the experimental channel. The reason for following this procedure is two fold. In the first place, since the recirculating circuit is a closed system, it is necessary to have a certain volume of water in it, in order to generate the required values of flow depth and flow discharge. In the second place, the fact that the sediment was already wet made the starting procedure easier, precluding the undesired deformation of the bed during the filling process.

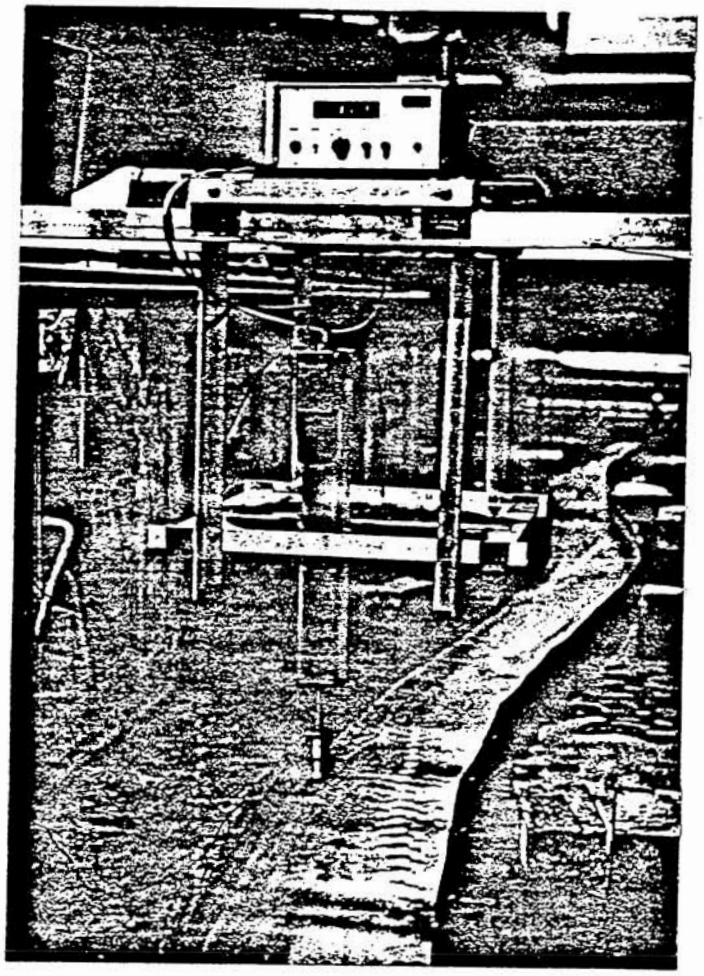

Fig. 5.5 Detecting Rod and Control Box of Bed–Profiler Used in the Experiments.

iii) Initiation of Experiments. The experiments were started by passing a very low discharge over the bed to prevent its deformation during the initiation stage. The flow discharge was

then slowly increased until the desired value of this variable was attained. The flow discharge was measured with a venturi–meter, and controlled periodically throughout the experiment. After the flow discharge was fixed, some adjustments to the amount of water in the system were made, to reach a surface level of the downstream pool that allowed an initial uniform flow all along the channel. Usually the initiation procedure did not last more than 10 or 15 minutes.

iv) Development of the Bed Deformation. After the experiment started, the bed deformation process began to develop spontaneously. During this process, the bed deformation was monitored periodically, taking notes, drawing sketches and measuring local values of variables such as scour, bar height and bar length. The duration of the development process varied with flow, slope and channel conditions, but in general was shorter for the experiments with the straight channel than for the experiments with the meandering channels. For the experiments with the straight channel the duration of the development process was in general of about two hours, while for the experiments with the meandering channels that duration was of about four to five hours.

v) Equilibrium State of the Bed Deformation. At the end of the development process, constant or equilibrium values of the different parameters describing the bed deformation were reached. This was easily detected for nonmigrating bedforms, such as those observed in some of the experiments with the meandering channels. In the case of migrating bedforms such as those observed in the straight channels, however, it was necessary to follow the whole train of bars as it developed and migrated downstream. Once the equilibrium state was reached, the experiment was allowed to run for at least another three or four hours.

The migration speed of the alternate bar train was measured by following the position of successive bar fronts as a function of time. A measuring tape attached to the flume served as the reference system for the measurements. The wavelength of the bedforms was also measured following this procedure.

Measurements of the bed and water surface elevations were made simultaneously after the equilibrium state was attained. Transverse profiles were taken each 0.30 m along a control reach which varied in length depending on the channel configuration. A control length of about 6.0 m was utilized for the experiments in the straight channel, which allowed to characterize two or three bar units. Longer control lengths were not used in the straight channel because of the fact that the bedforms were moving. Even though the migration speed of the bedforms was small, longer control reaches, which are associated with longer measuring times, would have introduced important errors in the characterization of the bed deformation. A control length equivalent to 1.5 meander wavelengths was used for the

experiments in the meandering channels, which corresponds to lengths of about 10.0 m or about 12.5 m depending on the channel configuration considered. Since very small migration rates or not migration at all was observed in those channels, this longer control reaches did not affect the accuracy of the measurements.

Five point measurements were taken for each of the transverse bed profiles. This points were not equispaced, but had the spacing shown in Fig. 5.6. The transverse profiles were taken along lines that are locally perpendicular to the channel axis.

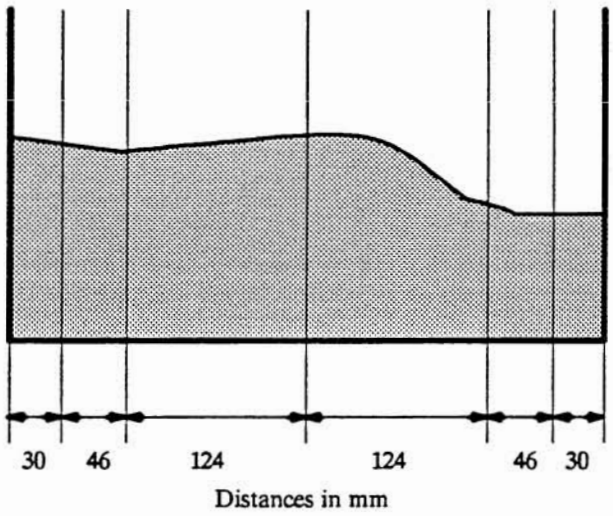

Fig. 5.6 Location of Point Measurements along Transverse Profile.

A second measurement of the bed deformation was taken once the experiment was finished.

For the experiments of the Series 03 in the straight channel (Channel 0), the total sediment transport rate was measured, by simply placing a collecting box inside the sediment trap at the end of the channel. No sediment transport rates were measured during the experiments in the meandering channels.

vi) End of the Experiments. After the flow depth and bed deformation measurements were completed, the experiments were finished by turning off the pump. This generated a rapid recession of the flow inside the channel, with almost no sediment transport associated with it, which prevented the deformation of the existing bedforms. Preserving the bedforms was important since in most cases a second measurement of the bed elevation was taken after the experiment was finished. The volume of water inside the system was large enough as to assure that the downstream part of the channel was still covered by water under no flow

conditions, which prevented the dissection of the sideslopes of the bars and consequent filling of the pools. Although, some small erosion of the sideslopes of the bars was produced in the upstream part of the channel which was not under water, that deformation was still very small to affect the measurements, given the resolution of the sampling grid employed.

vii) Final Measurements. In most of the cases, a second measurement of the bed deformation was taken after the experiment was finished. The methodology utilized was the same as that explained in v).

5.6 Experimental Results

In this section a summary of the results obtained in the experiments described previously is presented. No analysis of the experimental data is attempted at this point, and only the basic variables extracted from the data collected are shown in the Tables presented below.

Fig. 5.7 shows schematically the definition of the variables used to describe the bed deformation obtained in the experiments. Basically they correspond to the set of variables included in the dimensionless relationship (5.14). In what follows variables with the superscript * denote dimensioned parameters, while values without this superscript denote dimensionless parameters.

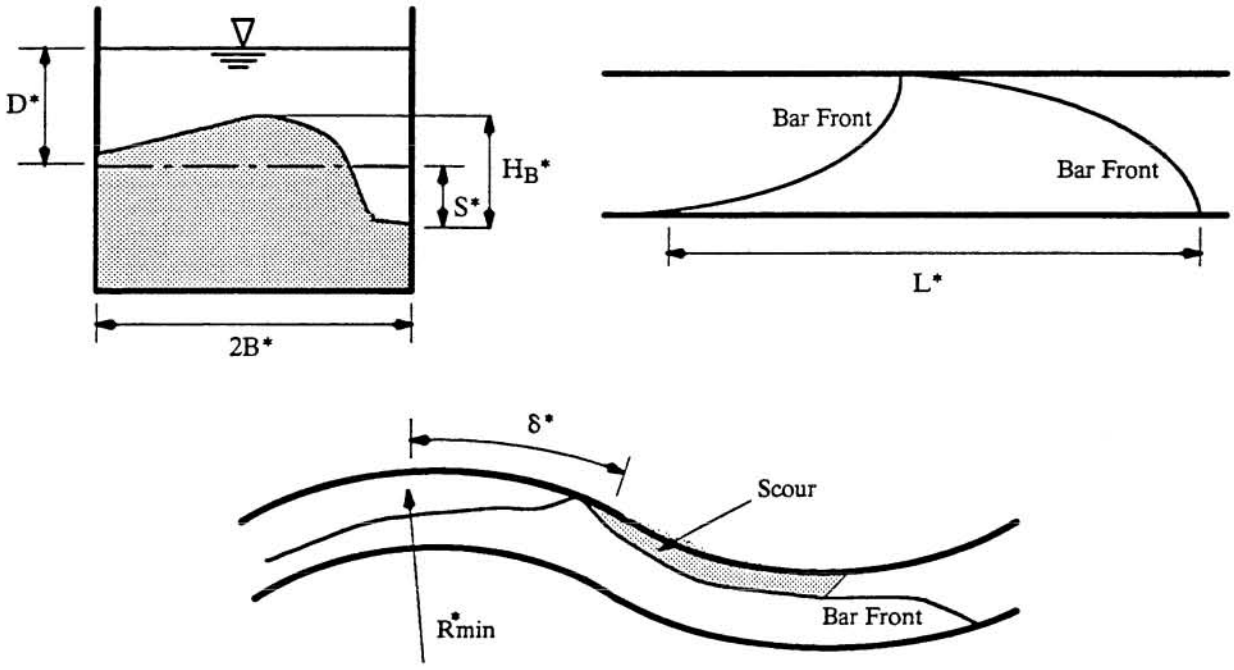

Fig. 5.7 Sketch for the Definition of Variables.

In Fig. 5.7, the depth of flow and the maximum scour are defined with respect to the mean bed elevation. This variable was computed from the data collected by making a numerical integration over the whole reach surveyed. A parabolic interpolation was utilized to compute the cross sectional area of each transverse profile measured. The depth of flow was computed by obtaining first a mean value of the water surface elevation along the channel, and then subtracting the mean bed elevation from this value. Since in general the deformation of the flow surface was very small, the mean water surface elevation was computed simply by averaging over the whole set of data collected.

Some researchers (e.g. Ikeda, 1984) define two different characteristic values of the bar height. One of those values is given by the variable defined in Fig. 5.7, which corresponds to the difference between the maximum and minimum bed elevation at the section of maximum scour. The other parameter usually employed is the maximum bar height, defined as the difference between the maximum and minimum bed elevation within a wavelength, which do not necessarily coincide at the same cross section. Herein such differentiation is not made because in all cases observed, the maximum bar height occurred precisely at the section of maximum scour.

The rest of the parameters characterizing the bed deformation, such as L^*, δ^*, etc, were computed directly from the data collected, such that mean values, characteristic of each experiment, were computed as simple averages over the available data.

Tables 5.4, 5.5 and 5.6 present the results obtained for the experiments in the straight channel (Channel 0), corresponding to Series 01, 02 and 03, respectively. In those tables the dimensioned values of the flow discharge and depth for each experiment of the series are shown, together with β, θ and the associated dimensionless values of the bar height, maximum scour, alternate bar wavelength, bar celerity, and the Reynolds and Froude numbers of the flow.

The Reynolds number of the flow, defined as $Re = q\,\rho/\mu$, where q is the flow discharge per unit width, and μ and ρ are the dynamic viscosity and density of the water, has been included therein even though the dimensional analysis performed before did not predict any effect of this parameter in the functional relationship derived (see for instance (5.11)). Evidently this parameter did not appear as relevant in the problem since a fully turbulent flow was assumed, for which no viscous effects are present. Herein the experimental values of the Reynolds number has been used as to define whether the observed flows were effectively turbulent.

Table 5.4 Experimental Results in Channel 0 – SERIES 01.

Q (l/s)	D* (mm)	β	θ	H_B	S	L*/2B*	c x 10^4	Re	F_0
0.750	7.7	26.08	0.049	3.69	2.71	8.75	1.2	1953	0.89
1.011	10.1	19.82	0.065	3.15	2.36	9.80	4.2	2633	0.80
1.370	13.0	15.34	0.084	2.45	1.73	9.14	7.8	3568	0.74
1.523	14.2	14.08	0.091	2.36	1.77	10.00	6.9	3966	0.72
1.890	16.9	11.86	0.108	1.71	1.30	9.00	6.6	4922	0.69
2.107	17.3	11.55	0.111	1.75	1.33	9.25	9.6	5487	0.74
2.510	19.6	10.20	0.126	1.55	1.32	8.75	10.2	6536	0.73
2.950	20.4	9.83	0.130	1.49	1.12	8.75	6.3	7682	0.81
2.981	21.3	9.39	0.136	1.40	1.06	8.00	6.9	7763	0.77

Table 5.5 Experimental Results in Channel 0 – SERIES 02.

Q (l/s)	D* (mm)	β	θ	H_B	S	L*/2B*	c x 10^4	Re	F_0
1.033	11.6	17.24	0.058	1.08	0.91	9.00	-	3003	0.66
1.494	13.8	14.53	0.069	2.03	1.52	9.13	5.0	4343	0.74
1.972	16.5	12.12	0.083	1.58	1.11	9.15	9.1	5733	0.74
2.509	19.1	10.50	0.096	1.21	0.91	8.60	9.3	7294	0.76
2.905	20.6	9.71	0.104	1.19	0.97	8.40	8.6	8445	0.79

Table 5.6 Experimental Results in Channel 0 – SERIES 03.

Q (l/s)	D* (mm)	β	θ	H_B	S	L*/2B*	c x 10^4	Re	F_0
1.741	15.0	13.30	0.055	0.80	-	-	-	4946	0.75
1.961	17.2	11.66	0.063	1.17	0.76	9.14	7.0	5571	0.70
2.266	18.7	10.71	0.068	0.90	0.66	9.73	6.1	6438	0.71
2.491	19.9	10.06	0.073	0.80	0.57	8.13	7.4	7077	0.71
2.861	22.1	9.04	0.081	0.80	0.60	8.50	6.7	8128	0.69

Table 5.7 presents the bedload measured in the experiments of Series 02. In that table the values of the discharge, depth of flow and bedload are shown, together with the dimensionless parameters Φ and d_s, where Φ is the Einstein dimensionless sediment transport rate defined as:

$$\Phi = \frac{Q_s^*}{d_s^* \left((\rho_s/\rho - 1)\, g\, d_s^* \right)^{\frac{1}{2}}}$$

and Q_s^* is the total volumetric sediment transport rate per unit width.

Table 5.7 Bedload Measurements in Channel 0 – SERIES 02.

Q (l/s)	D* (mm)	Q_s^* (gr/s)	1/ ds	Φ
1.095	11.0	0.406	20.8	0.003
1.432	14.0	1.432	26.4	0.011
1.972	16.5	2.559	31.1	0.020
2.431	18.5	1.905	34.9	0.015
2.774	20.5	2.431	38.7	0.019

Tables 5.8, to 5.11 present the results obtained for the experiments in the meandering channels (Channels 1, 2 and 3), corresponding to Series 11, 12, 21 and 31, respectively. In those tables the dimensioned values of the flow discharge and depth for each experiment of the series are shown, together with β, θ and the associated dimensionless parameters characterizing the bed deformation and the Reynolds and Froude numbers of the flow.

In the experiments made in Channel 1, no migrating bars were observed. Therefore the scour and bar height presented in Tables 5.8 and 5.9 correspond to that of the fixed bars formed at channel curves. In those tables, the dimensionless parameter δ defined previously to characterize the lag between the zone of maximum scour and the apex of the curves is also presented.

Table 5.8 Experimental Results in Channel 1 – SERIES 11.

Q (l/s)	D* (mm)	β	θ	H_B	S	δ	Re	F_0
1.040	11.1	18.00	0.063	3.29	2.72	0.00	2955	0.71
1.454	12.9	15.54	0.074	3.27	2.59	0.05	4131	0.80
2.046	16.4	12.21	0.094	2.61	1.88	0.14	5813	0.78
2.479	18.4	10.88	0.105	2.48	1.78	0.19	7043	0.79
2.890	23.2	8.62	0.133	2.04	1.46	0.29	8210	0.65

Table 5.9 Experimental Results in Channel 1 – SERIES 12.

Q (l/s)	D* (mm)	β	θ	H_B	S	δ	Re	F_0
1.033	11.0	18.21	0.070	3.14	2.40	0.00	2869	0.72
1.523	13.5	14.78	0.086	2.71	1.97	0.10	4231	0.77
2.450	18.5	10.81	0.118	2.38	1.71	0.19	6806	0.78

In all of the experiments made in Channel 2, migrating bars were observed to develop, coexisting with fixed bars formed at the channel curves. Accordingly, variables as wavelength and celerity of the migrating alternate bar train were measured in the same way done in the experiments in the straight channel. Also, two different characteristic bar heights and scour can be defined, depending on whether the migrating bar train is in or out phase with respect to the channel curvature. Larger heights and scours were observed for bars that at a given time are in phase with respect to the channel curves, i.e., when the migrating bars melt with the fixed bars. In Table 5.10, dimensionless values of the measured bar heights for in and out of phase conditions are shown, together with the maximum scour defined by the fixed bars, and the wavelength and celerity of the migrating bedforms.

Table 5.10 Experimental Results in Channel 2 – SERIES 21.

Q (l/s)	D* (mm)	β	θ	H_B 1	H_B 2	S	L*/2B*	c x 10^4	Re	F_0
1.011	11.0	18.18	0.063	2.89	2.05	2.28	11.88	0.3	2872	0.70
1.474	13.7	14.58	0.078	2.51	2.04	1.93	12.07	-	4188	0.73
1.957	16.3	12.24	0.093	2.08	1.77	1.51	13.73	2.2	5560	0.75
1.980	16.0	12.54	0.091	2.26	1.76	1.71	14.52	2.0	5625	0.79
2.467	18.4	10.87	0.105	1.81	-	1.33	15.32	2.7	7009	0.79
2.879	21.1	9.48	0.121	1.47	1.33	1.05	14.03	4.1	8179	0.75

H_B1: Bars in Phase H_B2: Bars not in Phase

Migrating bars were observed to develop in only one of the experiments made in Channel 3, corresponding to the maximum value of β of that series. For lower values of β only fixed bars were observed, similar to those observed in the experiments in Channel 1. In Table 5.11, the bar height in the experiments with fixed bars and the maximum bar height (in phase) in the experiment with movable bars are presented, together with the maximum scour and the observed values of the parameter δ for the experiments with fixed bars.

Table 5.11 Experimental Results in Channel 3 – SERIES 31.

Q (l/s)	D* (mm)	β	θ	H_B	S	δ	Re	F_0
1.499	13.7	14.65	0.063	2.86	2.25	-	4409	0.75
1.965	15.7	12.74	0.063	2.68	2.21	-0.05	5779	0.80
2.533	17.7	11.30	0.063	2.62	2.02	-0.01	6666	0.86
2.931	19.6	10.20	0.063	2.09	1.51	0.12	7328	0.85

6. ANALYSIS OF EXPERIMENTAL RESULTS

6.1 Introduction

Herein the analysis of the experimental results presented in the preceding chapter is made. Section 6.2 presents the analysis of the results corresponding to the experiments in the straight channel (Channel 0), Series 01, 02 and 03, while Section 6.3 presents the analysis of the results corresponding to the experiments in the meandering channels (Channels 1, 2 and 3), Series 11, 12, 21 and 31.

The analysis of the experimental results is based mainly on the dimensional analysis developed in the preceding chapter, particularly on the dimensionless relationship given by (5.14). This relationship expresses that for given sediment properties, fixed values of the channel width, shape and slope, and if the Froude number is restricted to a narrow band, any parameter describing the bed deformation should be only a function of β.

In order to compare the experimental results with theoretical developments, use is made of some of the theories on the alternate bar and river meandering phenomena discussed in Chapter 2.

6.2 Analysis of Results in the Straight Channel

6.2.1 Generalities. The first step of the analysis is to verify in general terms how the results obtained herein compare with the results of similar experimental studies. With this aim, the relationships proposed by Ikeda (1984), based in an extensive set of experimental data from different investigations, are used. Ikeda (1984) proposed the following relationships for the dimensionless bar height H_B and wavelength $L^*/2B^*$:

$$H_B = 0.1208\ \beta^{1.9}\ d_*'^{-0.45} \quad , \quad 3 < \beta < 20 \qquad (6.1)$$

$$L^*/2B^* = 7.76\ \beta\ d_*'^{-0.45} \quad , \quad F_0 > 0.8 \qquad (6.2)$$

This relationships are plotted in Figs. 6.1 and 6.2, together with the experimental data of the present study. In those figures, the dashed lines indicate the scatter of the data utilized by Ikeda. From that figure it appears that most of the data of the present study fall relatively well within the expected scatter range as defined by Ikeda. This leads to the conclusion that, in general terms, the data obtained herein do not present important scale effects that may have made them not comparable to other data sets.

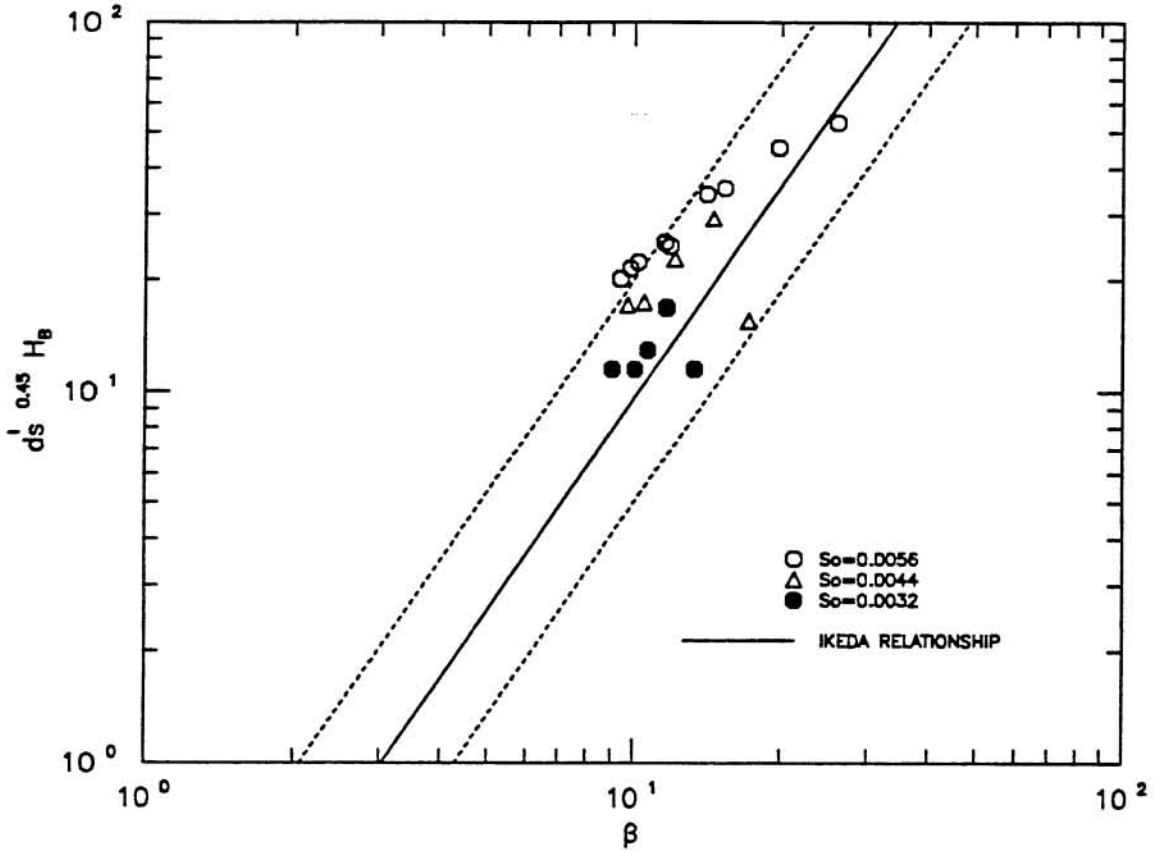

Fig. 6.1 Comparison of Experimental Values of Dimensionless Bar Height with Ikeda Relationship.

It is necessary to point out here, however, that it is apparent that the relations proposed by Ikeda do not adequately predict the physical behavior of the parameters describing the dimensions of the observed alternate bars. In fact by comparing the dimensionless parameters involved in (6.1) and (6.2) with those of equations (5.10) or (5.11), it is clear that Ikeda's relations do not consider the effect of the channel slope, or alternatively, the dimensionless bottom shear stress. Besides, they put some restrictions over the Froude number only in the prediction of the wavelength. At least, the latter supports the argument given for the derivation of (5.14), in which the Froude number was neglected. This conclusion may be valid, however only for a restricted range of variation of this parameter.

From Tables 5.4 to 5.6 it can be concluded that the range of variation of the Froude number in the present experiments is in fact very narrow, being bounded by the values 0.70 and 0.80 approximately. This fact allows to neglect Froude number effects in the following, thus supporting an analysis of the experimental data based in (5.14).

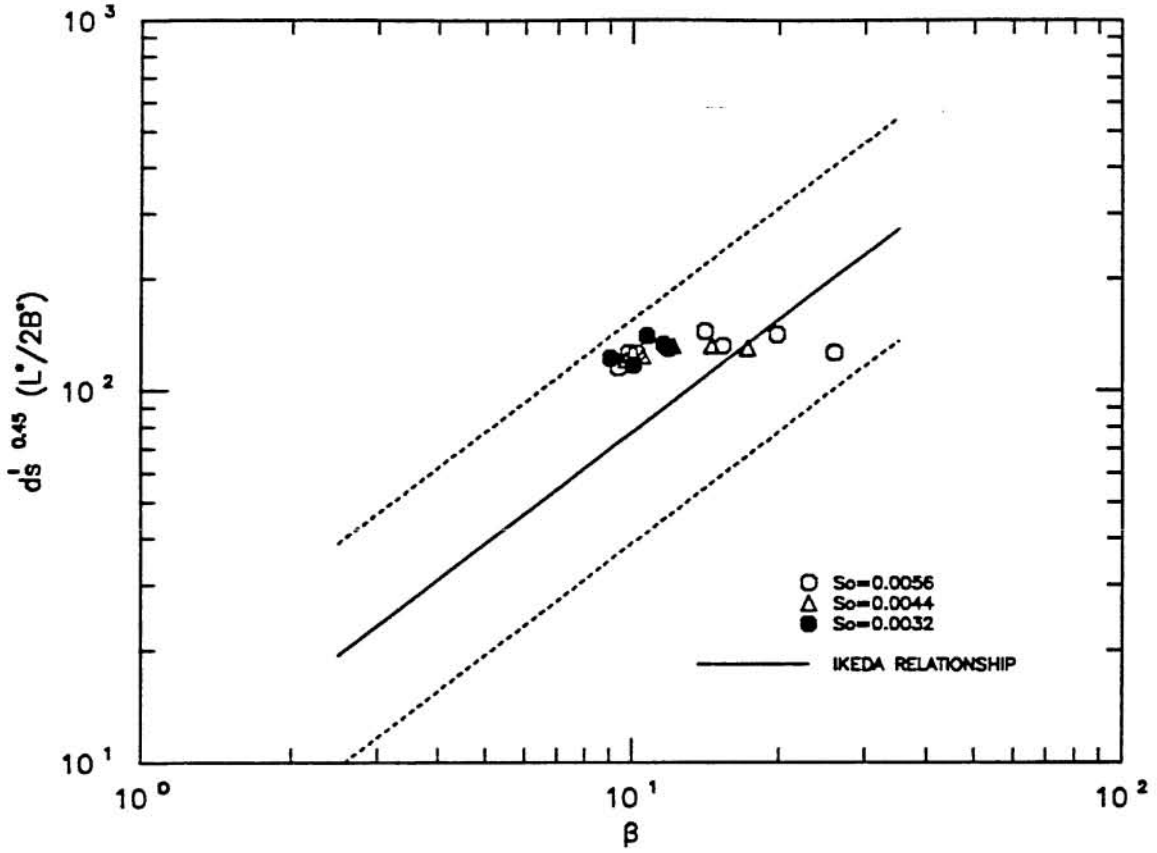

Fig. 6.2 Comparison of Experimental Values of Dimensionless Bar Wavelength with Ikeda Relationship.

From Tables 5.4 to 5.6 it can also be concluded that the variation of the Reynolds number in the present experiments is in the range 2000 to 8000. This indicates that the observed flows were effectively turbulent, although since the lower limit of that range is not so high, some influence of the viscosity may not be disregarded a priori, at least in the experiments covering the lower range of Reynolds numbers. On the other hand, the relative roughness of the flows, which can be measured by the dimensionless parameter $d_s = d_s^*/D^*$, was relatively high, varying in the range 0.025 to 0.070. By estimating the Reynolds number of the sediment particle as $Re_p = u^* d_s^* / (\mu/\rho)$, where $u_* = (g D^* S_0)^{1/2}$, it can be shown that in the present experiments Re_p varied in the range 11 to 18, which indicates that the sediment bed was in the transition regime between hydraulically smooth and hydraulically rough wall conditions.

According to what was explained above and the relatively good agreement of the present results with previous experimental data as observed in Figs. 6.1 and 6.2, it can be expected that viscous effects did not play an important role in the overall pattern of the observed bed deformation.

6.2.2 Bar Height. With the aim of analyzing the behavior of the dimensionless bar height H_B in more detail, this parameter is plotted as a function of β and S_0 in Fig. 6.3. Note that for given sediment properties and channel width, (5.11) predicts that the dimensionless bar height in the straight channel is a function only of the parameters considered above.

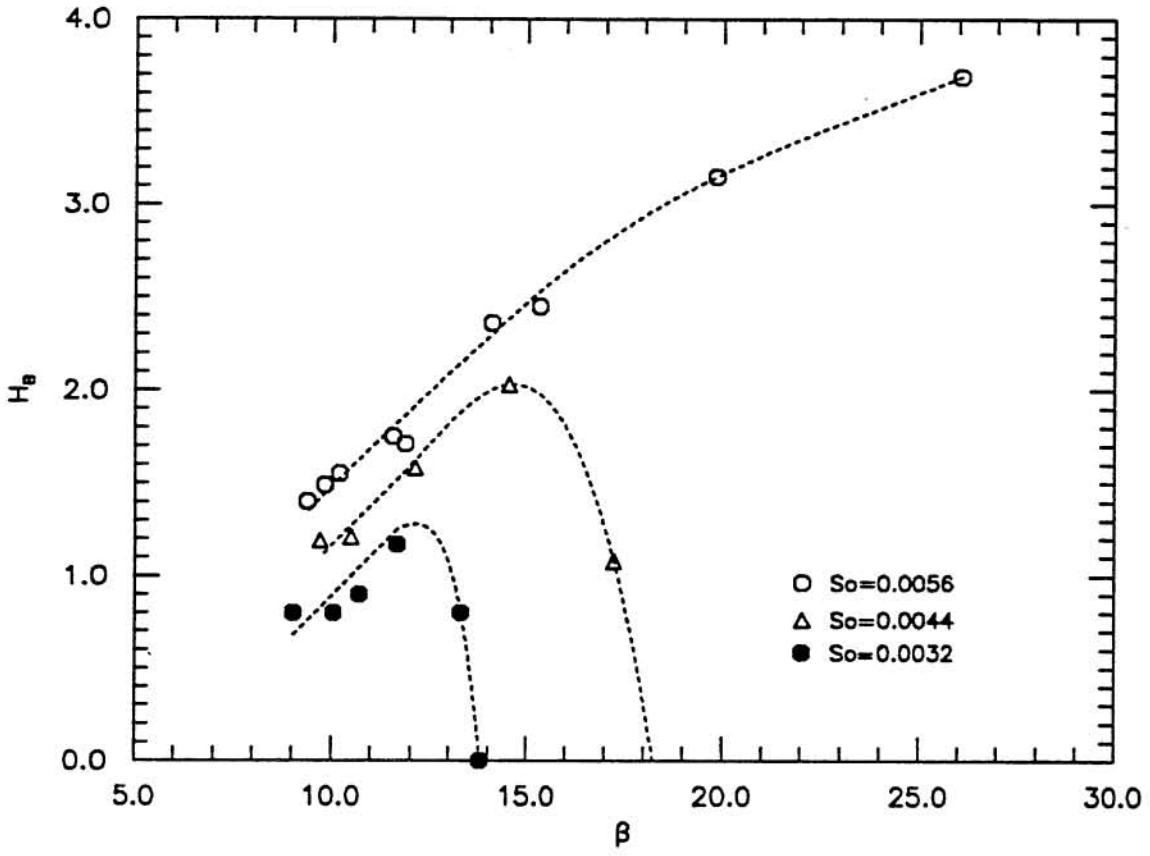

Fig. 6.3 Experimental Values of the Dimensionless Bar Height as a Function of β and S_0.

Fig.6.3 reveals some interesting features of the dimensionless bar height behavior. In general terms, H_B tends to increase as β increases, i.e. as the flow depth decreases. In the experiments corresponding to the slopes 0.0032 and 0.0044 a limit value of β exists, beyond which a sharp decreasing of the bar height is observed, such that it eventually reaches a vanishing magnitude at a certain critical value of β. For the experiments corresponding to the slope 0.0056, such behavior is not observed within the experimental range of β, however the rate at which the dimensionless bar height increases with β tends to decrease for values of this parameter larger than 15. The slope of the channel also appears to play an important role in the phenomenon, such that, in general, larger values of H_B are observed for larger values of S_0. The curves fitted to the experimental data with different slope define parallel

tendencies, at least for values of β lower than the limit described above. The slope of the channel also seems to affect the values of that limit, in that larger values of β at the vanishing bar height limit are observed for larger slopes of the channel.

From what it is exposed above, it can be concluded that two critical values of β seem to exist for a given slope of the channel. The lower limit, associated with deeper flows, corresponds to the threshold condition for the formation of alternate bars, or in other words, to the parameter β_c analyzed in detail in Chapter 3. This limit, however, was not covered by the range of experimental conditions because it is associated with flow discharges which are larger than the maximum given by the experimental facilities utilized herein. The upper limit, associated with shallower flows, corresponds to the critical value of β at which the bar height vanishes. This limit is associated with the threshold condition for sediment motion, such that for larger values of β no movement of sediment is possible, neither is the formation of bedforms. Obviously, being the bottom shear stresses related to the slope of the channel, larger slopes imply larger shear stresses, which are associated with higher sediment transport capacity and therefore with larger values of the upper limit of β.

Last conclusion means that if large enough values of β had been tested in the series corresponding to the slope 0.0056, a decreasing trend in the H_B curve should have been observed, similar to those shown in Fig. 6.3 for the slopes values of 0.0044 and 0.0032.

Next, a comparison between the present experimental results and the theoretical developments for the finite amplitude of alternate bars made by Colombini et al. (1987) and discussed previously in Chapter 2, is made.

Colombini et al. (1987) by means of a weakly nonlinear analysis developed a very simple relationship that allows to estimate the maximum bar height of the alternate bar structure. This relationship can be written in dimensionless terms as:

$$H_B = b_1 \left(\frac{\beta - \beta_c}{\beta_c} \right)^{\frac{1}{2}} + b_2 \left(\frac{\beta - \beta_c}{\beta_c} \right) \qquad (6.3)$$

where H_B has been used here to represent the dimensionless maximum bar height since, as was already discussed, in the present experiments the bar height coincided with the maximum bar height as defined in the preceding chapter. In (6.3), b_1 and b_2 are parameters that depend on θ and d_s, and β_c is the critical value of β for the formation of alternate bars as defined and analyzed in Chapter 3. Fig. 5 of Colombini et al. (1987) presents a graph that allows to compute b_1 and b_2, such that for the range of values of θ and d_s in the present experiments, b_1 takes values close to 1.0, while b_2 is in the range 0.7 to 0.8.

Since the present experiments did not cover the range of β close to β_c, no experimental values of the latter parameter are available to be used in (6.3). This parameter, however,

can be estimated from the predictive graphic relationships presented previously in Chapter 3. Instead, in what follows β_c is calibrated as to allow a good fit between the values predicted by (6.3) and the experimental data shown in Fig. 6.3. The calibrated values of β_c are then compared with the theoretical predictions of Chapter 3. Table 6.1 presents the calibrated values of β_c together with the corresponding critical values of θ and d_s, while Fig. 6.4 shows the resultant theoretical predictions for the dimensionless bar height plotted together with the experimental data of Fig. 6.3.

Table 6.1 Calibrated Values of β_c.

S_0	β_c	θ_c	$d_{s\,c}$
0.0056	5.5	0.230	0.015
0.0044	6.5	0.150	0.017
0.0032	7.5	0.100	0.020

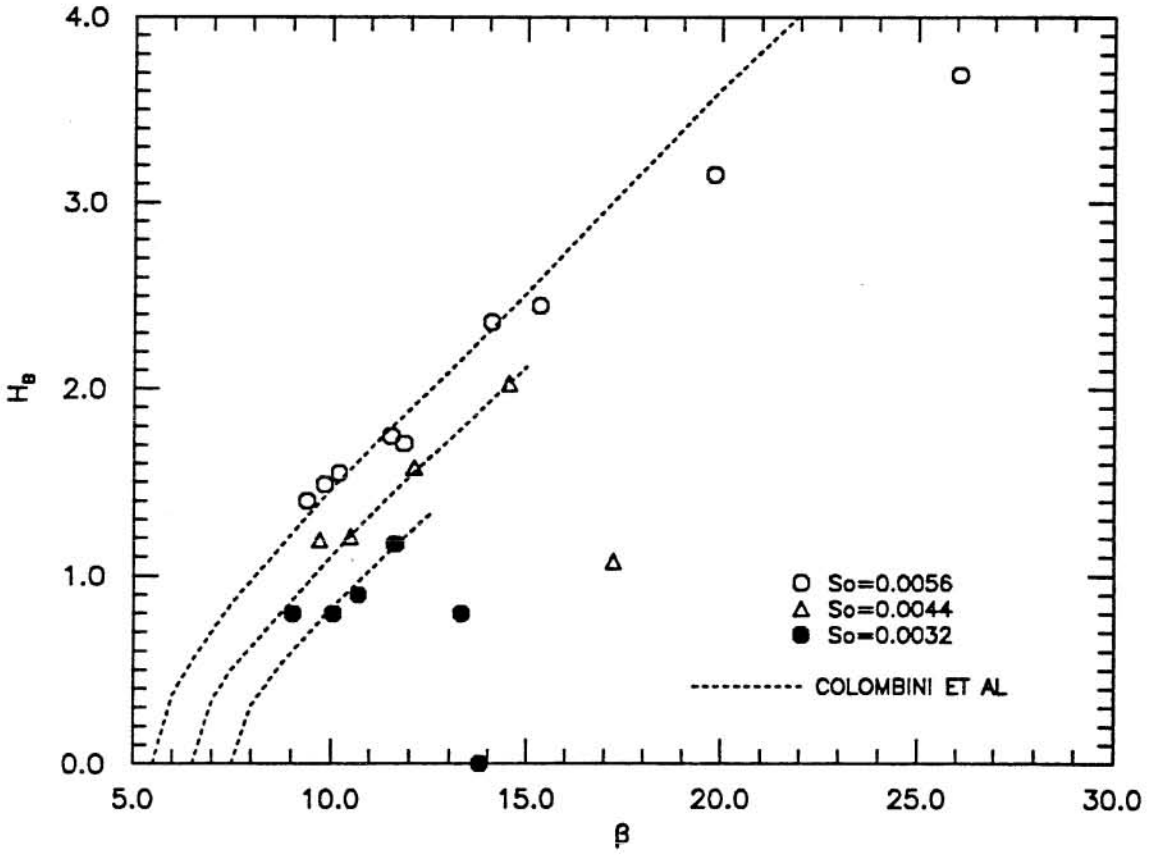

Fig. 6.4 Comparison of Experimental Values of Dimensionless Bar Height with Colombini et al. (1987) Predictive Relationship.

As it can be observed from Fig. 6.4, equation (6.3) describes adequately the observed behavior of the dimensionless bar height, at least within the limits of parallel behavior of the

experimental curves, and for the calibrated values of β_c. Obviously the theory is unable to reproduce the behavior of the curves in the neighborhood of the threshold condition for sediment motion, since it was derived by means of an asymptotic expansion about β_c, the critical condition for the formation of alternate bars. Besides, the theory is valid for small values of $(\beta - \beta_c)/\beta_c$. This is clearly observed in Fig. 6.4, in the experiments with slope 0.0056, for which theoretical and experimental curves diverge for values of β larger than about 15. This, which corresponds to a value of $(\beta - \beta_c)/\beta_c = 1.7$, however, still gives the theory a wider range of validity than expected.

To derive a complete theoretical description of the behavior of the dimensionless bar height, a second solution should be sought which has to be valid in the neighborhood of the critical condition for sediment motion. An asymptotic matching between both solutions would then complete the theoretical description. This is by no means an easy task since, as it was observed in the present experiments, in the vicinity of the critical condition for sediment motion, the alternate bar structure tends to evolve into elongated deformed shapes that hardly resemble the original alternate bar pattern, and which, for sure, are controlled by strong nonlinear effects.

Table 6.1, shows that the calibrated values of β_c decrease with increasing slope, or equivalently, with increasing dimensionless shear stress θ. In order to compare this behavior and also the magnitudes of β_c with those predicted by the theoretical analysis presented in Chapter 3, Table 6.2 presents three different theoretical values of β_c, which were computed from Figs. 3.3, 3.5 and 3.7, using the values of θ and d_s of Table 6.1. Those three values correspond to the use of different resistance and bedload equations as closure relationships in the theoretical analysis.

Table 6.2 Comparison Between Calibrated and Theoretical Values of β_c.

S_0	β_c CALIBRATED	β_c (1)	β_c (2)	β_c (3)
0.0056	5.5	9.5	7.8	1.8
0.0044	6.5	9.2	8.7	0.6
0.0032	7.5	8.3	9.1	3.0

(1) : Meyer-Peter & Muller bedload relationship; flat bed Engelund-Hansen resistance equation.
(2) : Engelund-Hansen bedload relationship; flat bed Engelund-Hansen resistance equation.
(3) : Engelund-Hansen bedload relationship; dune covered Engelund-Hansen resistance equation.

From Table 6.2 it can be concluded that the values of β_c computed for flat bed conditions tend to overestimate the calibrated values of this parameter by an average

magnitude of about 30 to 40%, whereas the values computed for the dune covered bed, associated with higher resistance, tend to underestimate them, being on the average about 30% of the calibrated values. On the other hand, for flat bed conditions, the values of β_c corresponding to the Meyer-Peter and Muller bedload equation increase with increasing slope, defining a tendency that is opposite to that exhibited by the calibrated values, whereas the values of β_c corresponding to the Engelund-Hansen bedload relationship follow a trend that is in agreement with that observed for the calibrated values.

The observations made above, point out that it is crucial for the adequate modeling of the phenomenon being studied to know what relationships best describe the bedload transport and flow resistance occurring in the alternate bar regime. From the values in Table 6.2, the Engelund-Hansen bedload relationship performs better than the Meyer-Peter and Muller equation, in that it adequately predicts the tendency exhibited by β_c. Similarly, it seems that the flow resistance controls the magnitude of β_c, such that the higher the resistance the smaller the value of this parameter. From this point of view, the flat bed Engelund-Hansen resistance equation appears to predict less resistance than that required to generate values of β_c close to the calibrated ones, however the dune covered bed Engelund-Hansen resistance equation seems to predict excessive resistance, generating values of β_c that are well under the calibrated ones.

In order to contrast the latter conclusions with the present experimental observations, Fig. 6.5 shows a comparison between theoretical and experimental rating curves. The Engelund-Hansen resistance equation (3.5) was used for the computation of the theoretical rating curves, which have two branches corresponding to the flat bed and dune covered bed conditions, respectively. The lower curve corresponds to flat bed conditions and it is supposed to be valid for discharges smaller than the one associated with the intersection of the two branches. Accordingly, the upper branch corresponds to dune covered bed conditions and is supposed to be valid for discharges larger than the one associated with the intersection of the two branches.

As it can be observed in Fig. 6.5, the flat-bed theoretical curve tends to underestimate the observed resistance, predicting values of the flow depth that are in general lower than the corresponding experimental values, at least for flow discharges that are larger than the theoretical limit for flat bed conditions. On the contrary, the dune covered bed curve tends to overestimate the resistance, predicting values of the flow depth that are in general larger than the observed values.

The above observations are in agreement with the argument previously used to validate the calibrated values of β_c. On the other hand, they are opposed to the common

argument expressing that being the alternate bars very long bedforms as compared with the flow depth, the form resistance associated with them is negligible, and thus the resistance induced by these bedforms is mainly due to grain friction. From Fig. 6.5 it is clear that this argument is not valid in the present experiments, at least for the mean flow depth D^*, which, recall, is not a uniform value but the average over a wavelength of the bed deformation.

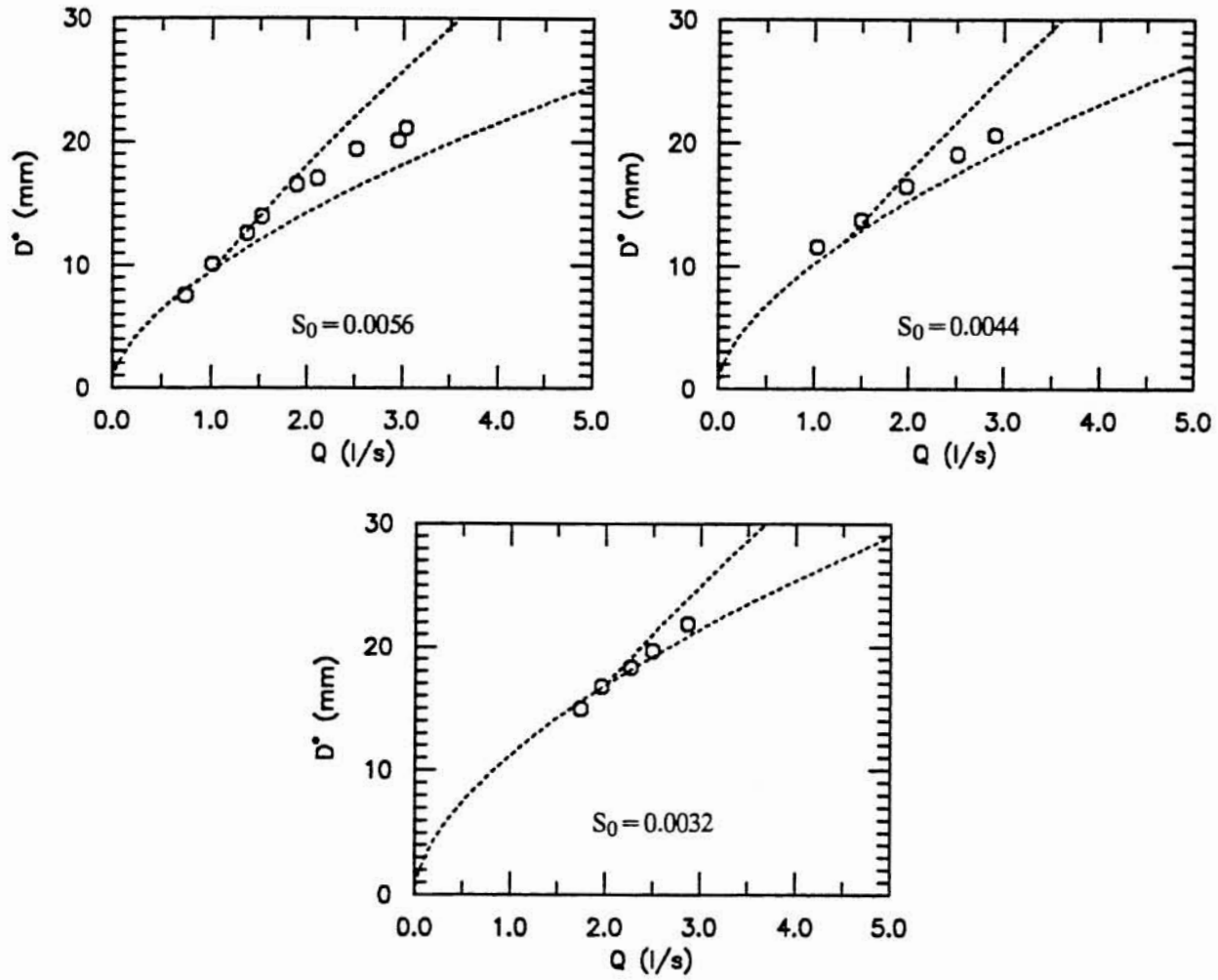

Fig. 6.5 Comparison Between Theoretical and Experimental Rating Curves.

A final conclusion derived from Fig. 6.5 is that even though the Engelund–Hansen equation predicts the development of dunes for a range of conditions covered by the present experiments, no bedforms of that kind were actually observed. This is not totally unexpected, considering that the stability conditions for the formation of bedforms of the dune type should be affected by the strong deformation of the flow induced by the alternate bar structure.

Fig. 6.6 presents a comparison between the experimental values of the dimensionless bedload Φ plotted as a function of d_s, together with the corresponding values predicted by the Meyer-Peter and Muller and Engelund-Hansen bedload equations. These last values were computed using equations (3.7a) and (3.7b) respectively, and the values of the channel slope corresponding to the SERIES 02, in which the bedload measurements were taken.

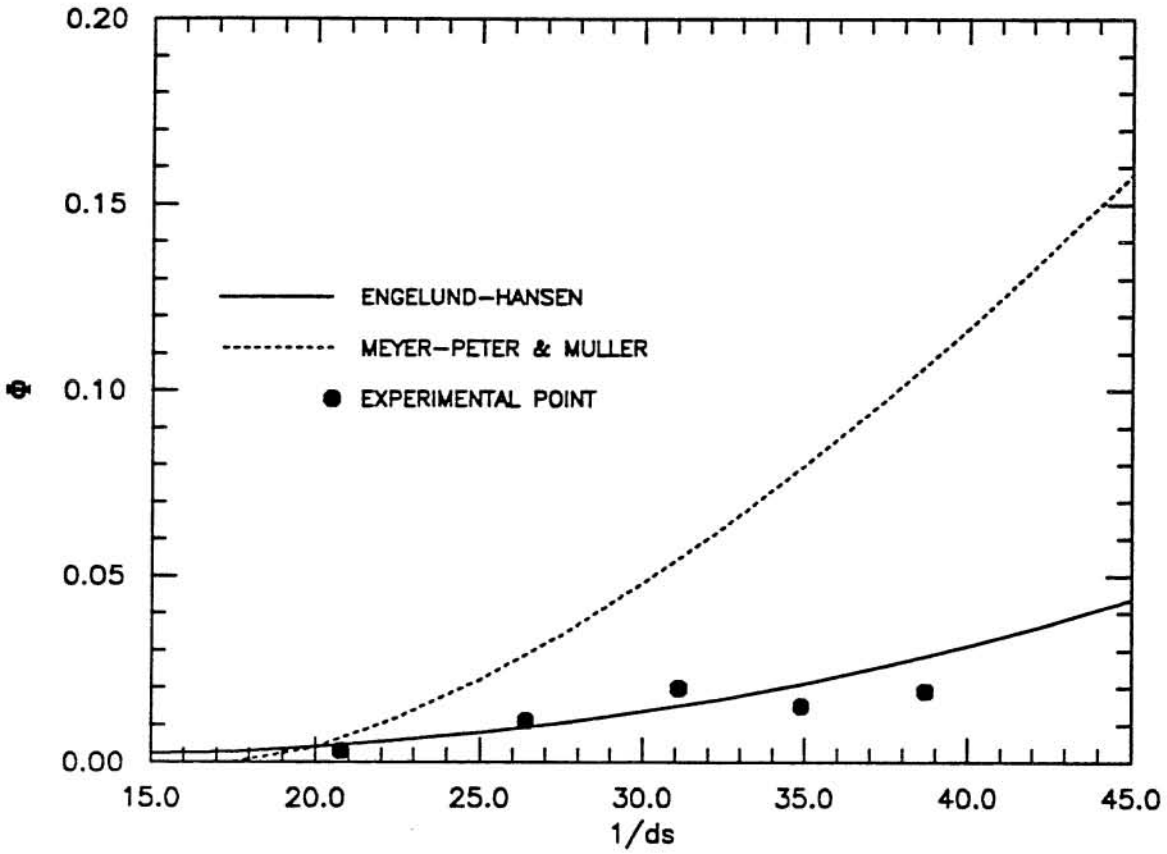

Fig. 6.6 Comparison Between Experimental and Predicted Values of Dimensionless Bedload Φ.

From Fig. 6.6, it is evident that Engelund-Hansen bedload equation predicts much more accurately the observed values of the bedload than the Meyer-Peter and Muller relationship. The latter equation largely overestimates the experimental values of the bedload in almost the whole range covered by the experiments, except for the range of very small values of $1/d_s$, which is close to the threshold conditions for sediment motion.

In conclusion, the experimental observations presented above support the use of the Engelund-Hansen equation as a bedload relationship, and also suggest that the observed resistance in the alternate bar regime exceeds that predicted by the flat bed Engelund-Hansen equation. Both arguments tend to indicate that the calibrated values of

β_c presented in Table 6.1 are plausible of being obtained theoretically if those conditions are included in the analysis. Accordingly, the theory for the finite amplitude of alternate bars developed by Colombini et al. (1987) appears to predict adequately the observations made in the present experimental study, at least within the limits of validity discussed before, and under the recommendations for the computation of the required β_c formulated above.

6.2.3 Scour. In order to analyze the behavior of the scour generated by the alternate bars as compared with the bar height, Fig. 6.7 presents a plot of S as a function of H_B. It is apparent from that figure that a linear relationship exists between those variables such that:

$$S = 0.75\ H_B \qquad (6.4)$$

This result is in good agreement with the experimental results analyzed by Ikeda (1984), who also found the same value for the coefficient of proportionality in (6.4).

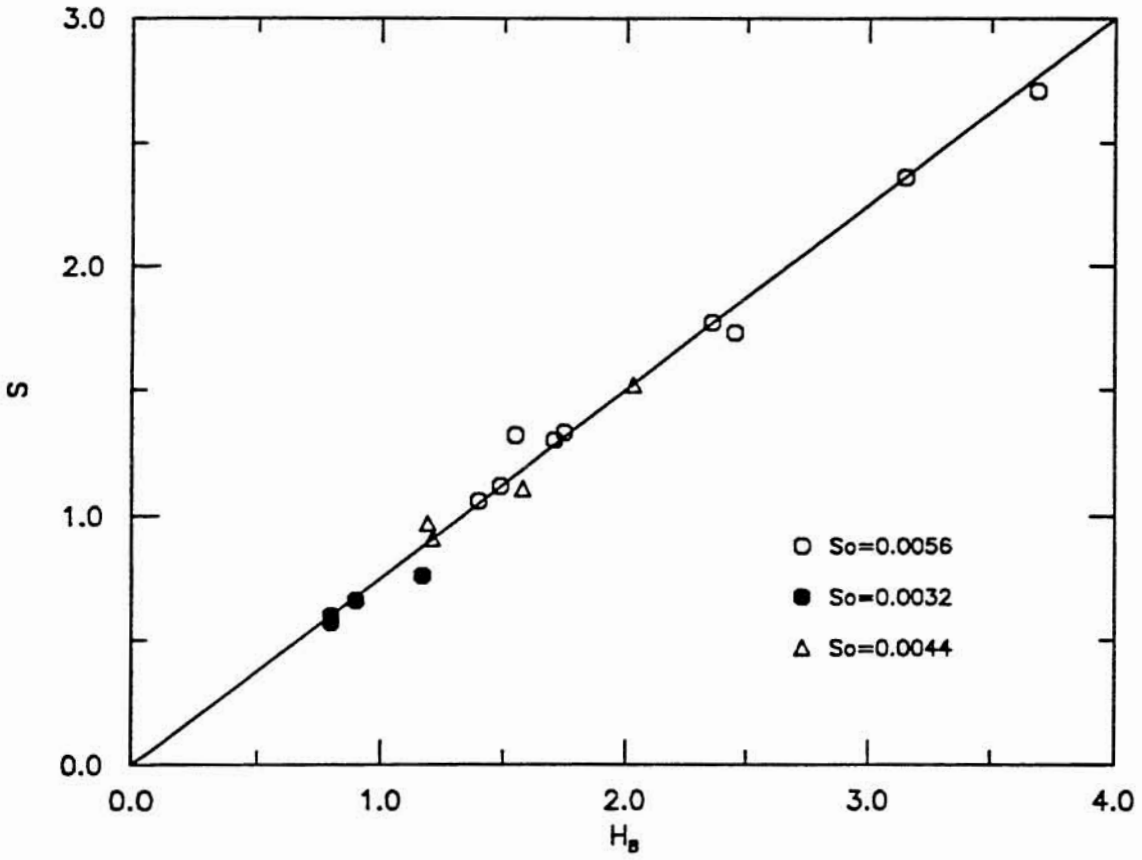

Fig. 6.7 Dimensionless Scour as a Function of the Dimensionless Bar Height.

6.2.4 Bar Wavelength. Fig. 6.8 presents the experimental values of the dimensionless wavelength of the observed alternate bars, plotted as a function of β. As it can be seen in that figure, the scattering of the experimental data is larger than in the case of the bar height

analyzed before. It is also apparent that the effect of the slope of the channel on the wavelength is less evident than in the bar height case, such that the experimental points do not seem to define different tendencies for different values of that parameter. According to this only one curve was fitted to the experimental data, just in order to define the global trend exhibited by them.

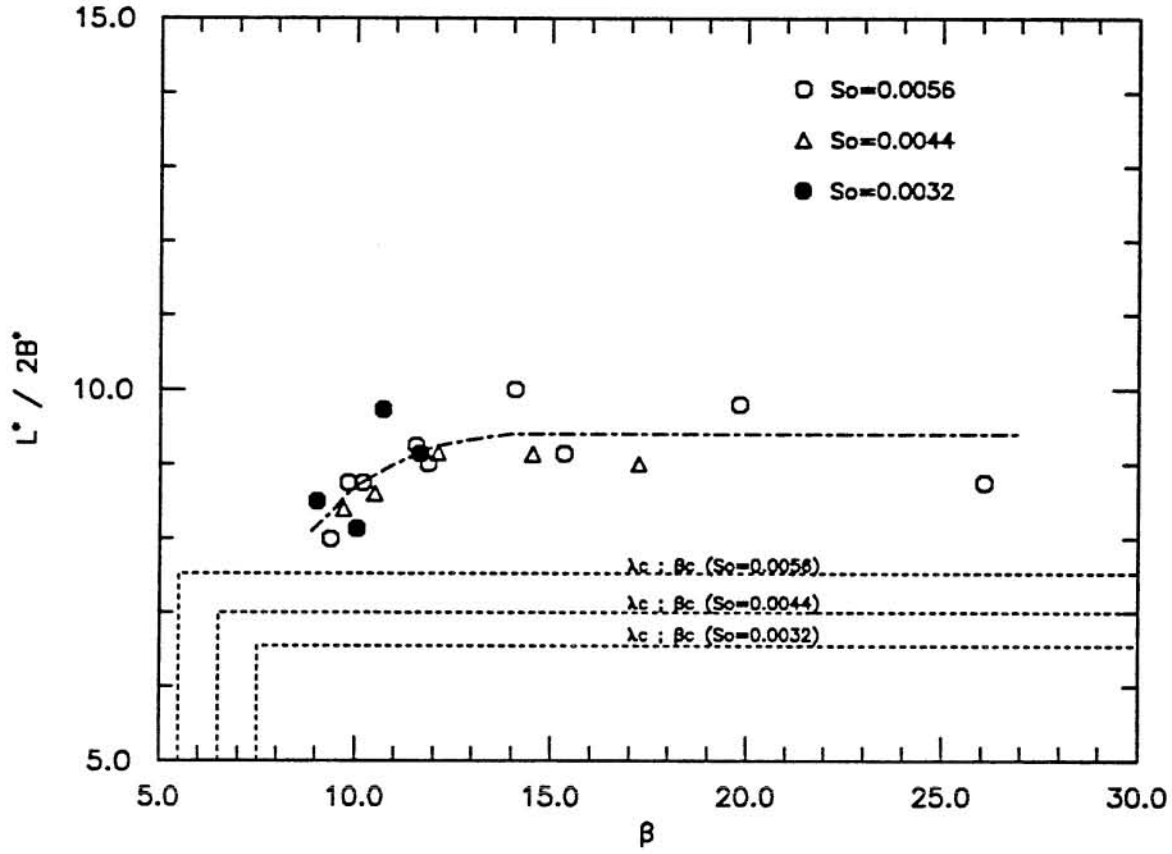

Fig.6.8 Experimental Values of the Dimensionless Wavelength as a Function of β.

From Fig. 6.8, it can be concluded that the experimental dimensionless wavelength tends to increase as β increases, approaching a constant value of about 9.4 for values of β larger than 15. This is in agreement with the experimental results analyzed by Ikeda (1984), which show that, in general, the dimensionless wavelength $L^*/2B^*$ is roughly equal to 9.0.

Fig. 6.8 also presents the theoretical values of the critical dimensionless bar wavelength corresponding to the calibrated values of β_c shown in Table 6.1, which were computed from Fig. 3.11 for flat bed conditions and using the Engelund–Hansen Bedload relationship. It can be observed therein that the theoretical predictions of the critical dimensionless wavelength take values around 7.0, which are lower than the values of this

parameter observed experimentally for conditions of well developed alternate bars. The experimental trend, however, tends to approach values that are relatively close to 7.0 for values of β lower than 10, i.e. for values of β approaching β_c. This shows that as the bar height, the wavelength seems also to increase from its critical value as β increases over the critical condition for the formation of alternate bars, although in the latter case a rapid tendency towards a constant value of the wavelength appears to occur.

6.2.5 Celerity of Alternate Bars. With the objective of analyzing the migration speed of the observed alternate bars, the experimental dimensionless values of this variable are shown in Fig. 6.9, plotted as a function of β. Even a larger scatter of the experimental data than in the case of bar wavelength is observed, such that it is not possible to clearly define the effect of the slope on the observed celerity of the bars. It is possible, however, to derive some general conclusions of the behavior of the alternate bars celerity.

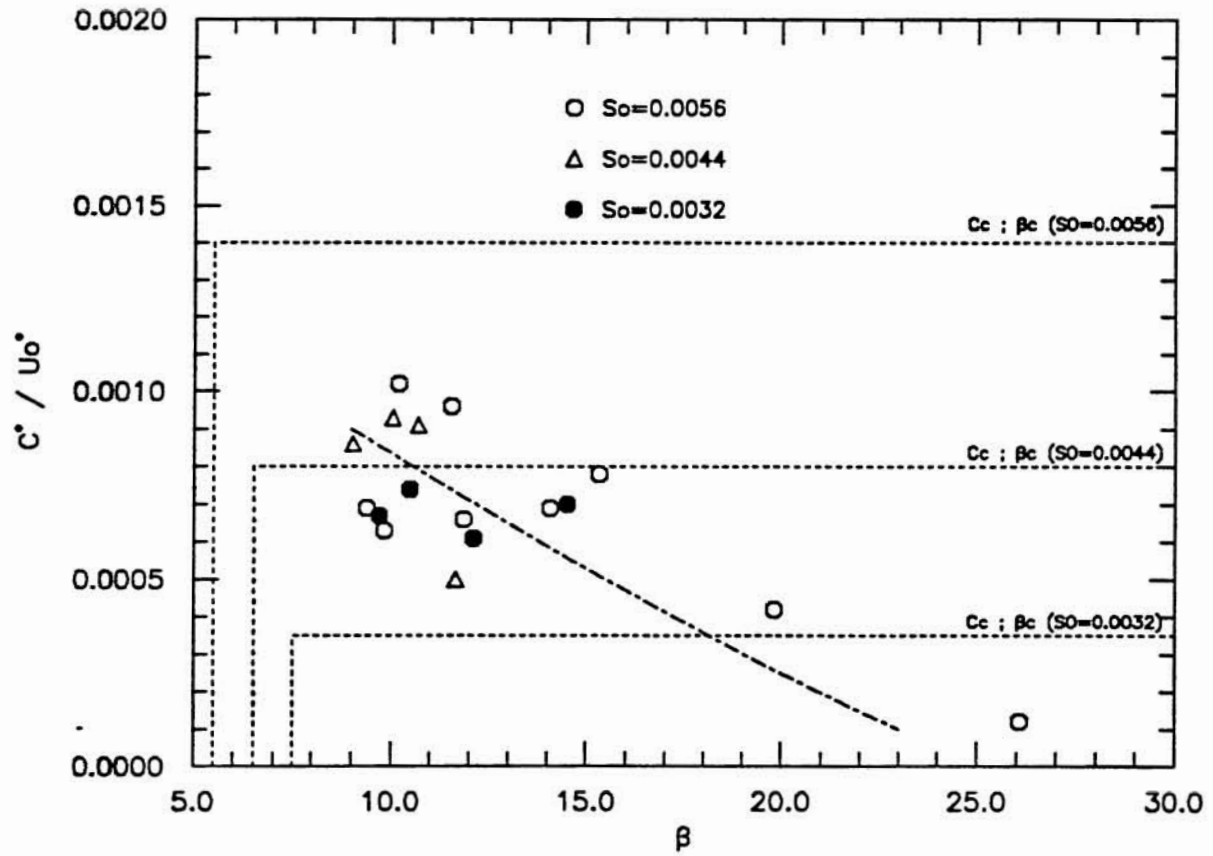

Fig. 6.9 Experimental Values of the Dimensionless Migration Speed as a Function of β.

As it can be seen in Fig. 6.9 the migration speed of the observed alternate bars is in fact very small, being in general lower than 0.1% of the mean flow velocity. A curve was fitted

to the experimental data, just to define the global trend exhibited by them. That trend indicates that the dimensionless migration speed of the bars tends to decrease as the parameter β increases. This conclusion seems to be reasonable, considering that as β increases, for a fixed value of the slope and also for a fixed sediment size, then the bottom shear stress decreases, and so does the transport capacity of the flow. Obviously for decreasing transport capacity, the migration speed of the bedforms, which depend directly on it, must also decrease. Even though the flow discharge also decreases for increasing β, a more sharp decreasing in the celerity of the bedforms can be expected to occur, such that a net decrease in the dimensionless speed is obtained.

In Fig. 6.9 the theoretical values of the critical dimensionless celerity of the alternate bars corresponding to the calibrated values of β_c shown in Table 6.1, which were computed from Fig. 3.10 for flat bed conditions and with the Engelund–Hansen bedload relationship, are also presented. It can be observed therein that the theoretical predictions of the critical dimensionless celerity take values in the range 0.04 to 0.15%, which appears to be wider than the observed variation of that parameter for conditions of well developed alternate bars. For this reason, the trend defined by the experimental data does not appear to be connected with the corresponding theoretical critical point. However, the theory seems to predict the order of magnitude of the measured migration speeds fairly well.

6.2.6 Fourier Analysis of the Bed Deformation. Next, in order to analyze the properties of the bed deformation associated with the observed alternate bars, not only from the point of view of local variables such as bar height or wavelength, but from the point of view of the overall bed topography, a two–dimensional Fourier analysis of the measured bed elevations is performed. With this aim, the bed elevation data are made dimensionless with the bar height, such that:

$$\eta\,(s^*,n^*) = \frac{\eta^*(s^*,n^*)}{H_B^*} \qquad (6.5)$$

The two–dimensional Fourier analysis is based in the representation of the measured bed deformation in a Fourier series, such that:

$$\eta\,(s^*,n^*) = \sum_{l=0}^{\infty}\sum_{m=0}^{\infty} \eta_{lm}\, e^{i\,(l\,\lambda_s\,s^* + m\,\lambda_n\,n^*)} \qquad (6.6)$$

with,

$$\lambda_s = \frac{2\pi}{L^*} \quad , \quad \lambda_n = \frac{2\pi}{4B^*} \qquad (6.7)$$

where λ_s is the wavenumber in the axial direction, associated with the wavelength L^* of the alternate bars, λ_n is the wavenumber in the transverse direction, associated with the

wavelength of the bed deformation in the transverse direction which corresponds to twice the channel width, i.e. to $4B^*$, and η_{lm} are the Fourier coefficients of the series, such that each of them represents the complex amplitude of the different wave components in which the bed deformation is decomposed. For example, the coefficient η_{11} represents the fundamental of the bed deformation, in that it corresponds to a two–dimensional wave whose wavelengths are identical to the alternate bar axial and transverse wavelengths respectively. Analogously, the coefficient η_{21} represents a harmonic which has half the wavelength of the alternate bar in the axial direction and a transverse wavelength that is equal to the transverse wavelength of the alternate bar. Following this interpretation, each of the coefficients can be understood as the amplitude of a two–dimensional wave which has wavelengths in the axial and transverse directions that are, in general, a fraction of the original wavelengths of the alternate bar being analyzed.

In order to compute the Fourier coefficients from the data collected in the present experiments, a discrete Fast Fourier Transform algorithm given by the IMSL MATH/LIBRARY software is used, which requires for the grid of discrete points representing the spatial domain to be uniform, although the spacing should not necessarily be the same in both directions. Since the grid utilized to take the bed measurements was not evenly spaced in the transverse direction, a parabolic interpolation is utilized to generate transverse profiles of uniform spacing. For each experiment, all sets of data corresponding to one axial wavelength of the alternate bars available are Fourier–analyzed, and the absolute value of the complex coefficients obtained for each of those bedforms are averaged. In this way, a set of averaged Fourier coefficients representing the weight of each harmonic associated with the bed deformation is obtained for each experiment, which allows to identify the most important harmonics and to analyze how they behave as a function of the channel slope and the parameter β.

From the results obtained through the analysis described above, it can be concluded that in general, only the first three or four harmonics in each direction have relevance in the Fourier characterization of the observed alternate bars, and even within that group only a few contribute to most of the total bed deformation. Fig. 6.10 shows as an example a density plot, in which the absolute value of the complex coefficient of the corresponding harmonic is represented in relative terms by the density of the gray scale, such that black represents a value equal to zero and white represents a value equal to the maximum observed. This particular example corresponds to the experiment $Q = 2.107$ l/s of the SERIES 01, however it is representative of the whole set of results obtained. From that figure, it is apparent that the most important harmonics correspond to η_{11} and η_{02}, which denote the fundamental and

a harmonic with no oscillation in the axial direction and with a transverse wavelength equivalent to the channel width, respectively. Other less important harmonics are η_{21} and η_{31}, which correspond to harmonics with axial wavelengths equal to one half and one third of the alternate bar wavelength, respectively, and with transverse wavelengths equivalent to twice the channel width.

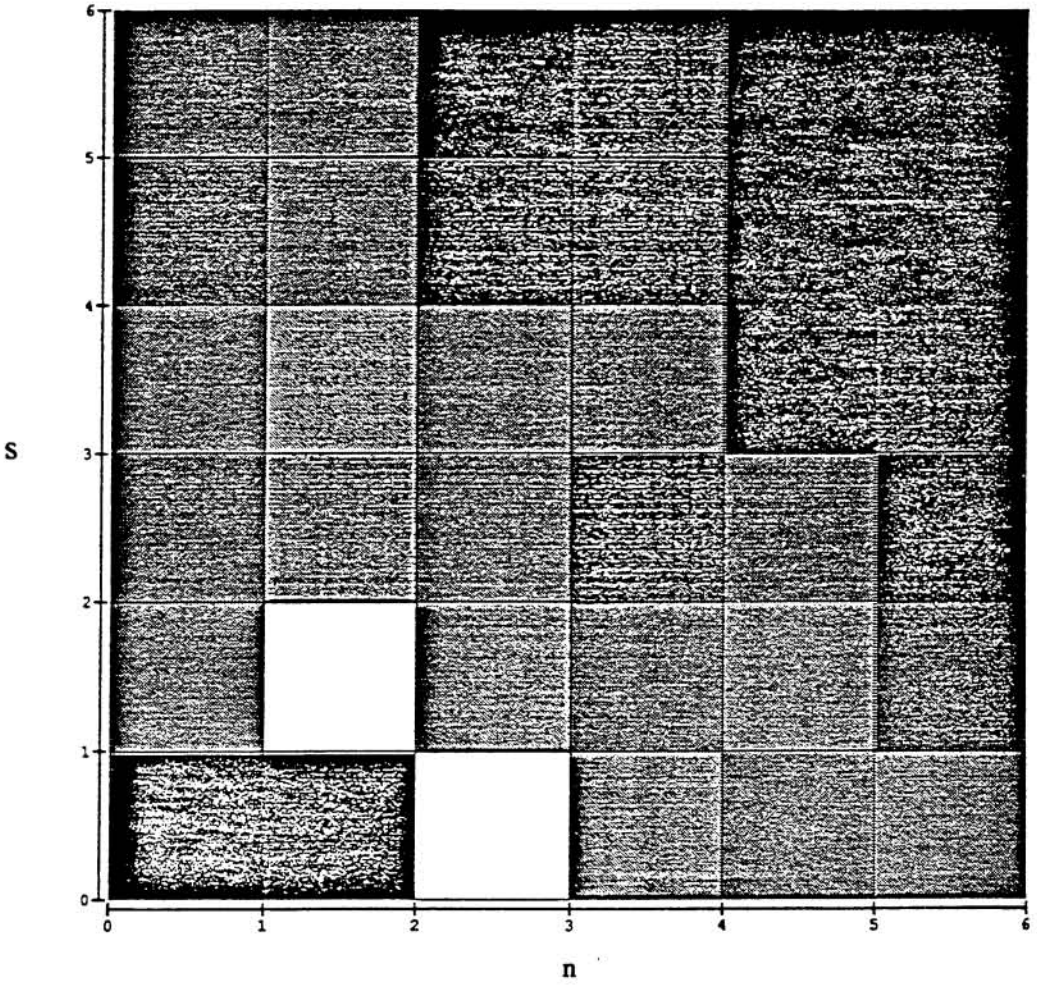

Fig. 6.10 Density Plot for the Typical Distribution of Fourier Coefficients Associated with the Experimental Bed Deformation. (Experiment Q=2.107 l/s; SERIES 01).

With the aim of analyzing how the dimensionless bed deformation corresponding to one alternate bar unit changes with β and the slope of the channel, Fig. 6.11 shows the absolute value of the complex Fourier coefficients corresponding to the harmonics η_{11}, η_{02}, η_{21} and η_{31}, plotted as a function of β, for different slopes associated with SERIES 01, 02 and 03, respectively.

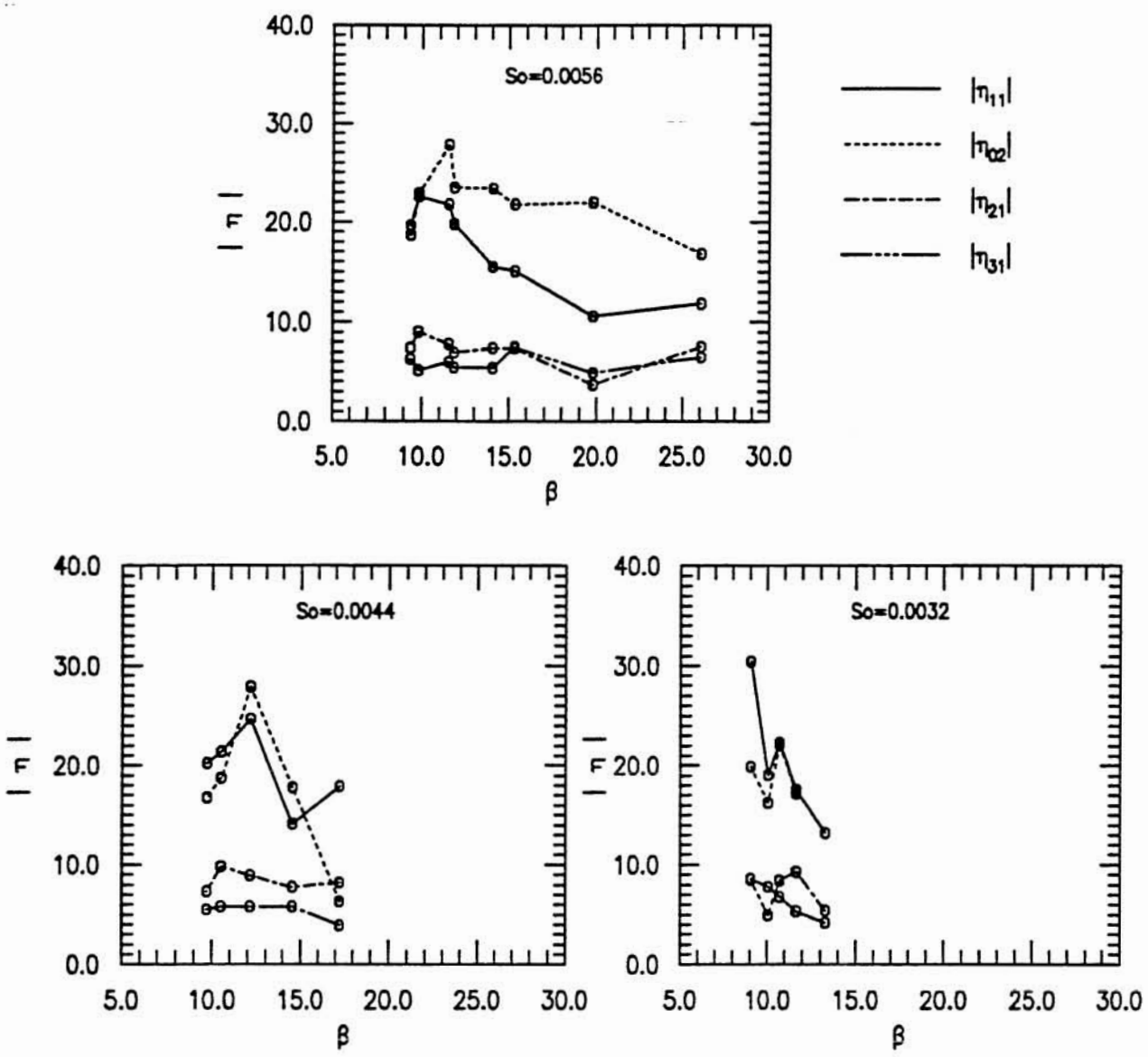

Fig. 6.11 Fourier Harmonics of Bed Deformation as a Function of β and S_0.

From Fig. 6.11 it can be concluded that in general terms the harmonics η_{11} and η_{02} are of comparable magnitude, which is of the order of twice the magnitude of the harmonics η_{21} and η_{31}. From that figure it is also apparent that while the latter do not show much variation either with β or with S_0, the former appear to be functions of both of those parameters. For the experiments with the highest slope, $S_0 = 0.0056$, the harmonic η_{02} seems to be of higher magnitude than the fundamental by about 40% on the average. For that slope, both η_{11} and η_{02} tend to increase as β decreases, however, for values of this parameter below approximately 11.0 they exhibit a relatively sharp decrease. For the experiments with the intermediate slope, $S_0 = 0.0044$, the fundamental is of similar magnitude as η_{02}. In this case

both parameters tend to increase as β decreases, similarly as for the experiments corresponding to $S_0 = 0.0056$. For the intermediate slope however, the rate of increasing is higher than in the latter case. As for the highest slope, η_{11} and η_{02} decrease sharply for values of β lower than 12.0. For the experiments with the lowest slope, $S_0 = 0.0032$, the fundamental and η_{02} are also of similar magnitude. Both parameters tend to increase as β decreases, at a rate comparable to that for the intermediate slope, $S_0 = 0.0044$, however, in this case, no decreasing of those harmonics is observed for small values of β.

According to what is exposed above, it can be concluded that the dimensionless geometry of the bed deformation is a function of both, β and S_0, which is reflected in the variation of its principal harmonics, η_{11} and η_{02}, with those parameters, as observed in Fig. 6.11. Comparing the qualitative behavior of those harmonics with the behavior of the dimensionless bar height shown in Fig. 6.3, it can be concluded that the zone of increasing values of η_{11} and η_{02} with decreasing β, corresponds to the zone of decreasing bar height with decreasing β, which is bounded by the limits corresponding to the critical condition for the formation of alternate bars and the critical conditions for sediment motion. It seems that whenever β is close to any of those limits a sharp variation of the principal harmonics of the bed deformation occurs, such that for example a sharp increase takes place as β decreases from values close to the critical conditions for sediment motion, and a sharp decrease occurs as that parameter gets closer to the critical conditions for the formation of alternate bars.

6.3 Analysis of Results in the Meandering Channels

6.3.1 Bar Height. With the aim of analyzing the behavior of the dimensionless bar height H_B for the experiments in the meandering channels, this parameter is plotted as a function of β in Fig. 6.12. In that figure, the results associated with each of the meandering channels tested, which correspond to the slope $S_0 = 0.005$, are plotted with a different symbol in order to analyze also the effect of the dimensionless parameters λ_m and ν, characterizing the geometry of the channel. As a reference, Fig. 6.12 also shows the curve fitted to the experimental results in the straight channel, corresponding to the slope 0.0056.

Although the curve representing the results in the straight channel in that figure is not totally comparable with the experimental results plotted therein, since it is valid for a larger slope, it can be considered to be the upper limit of the expected results in the straight channel for a slope $S_0 = 0.005$, and therefore it still can be utilized to make the comparison between the results in the meandering and straight channels.

As it can be observed in Fig. 6.12, the dimensionless bar heights corresponding to the experiments in the meandering channels are larger than that of the experiments in the straight channel, even for the case of smallest channel curvature, $\nu = 0.015$. In the latter case,

however, in which migrating bars were observed to develop in the channel, only the values of the dimensionless bar height associated with bars in phase with the channel curves were plotted, and therefore the previous conclusion is valid only for those bars. An analysis of the heights of migrating bars is made later in this section.

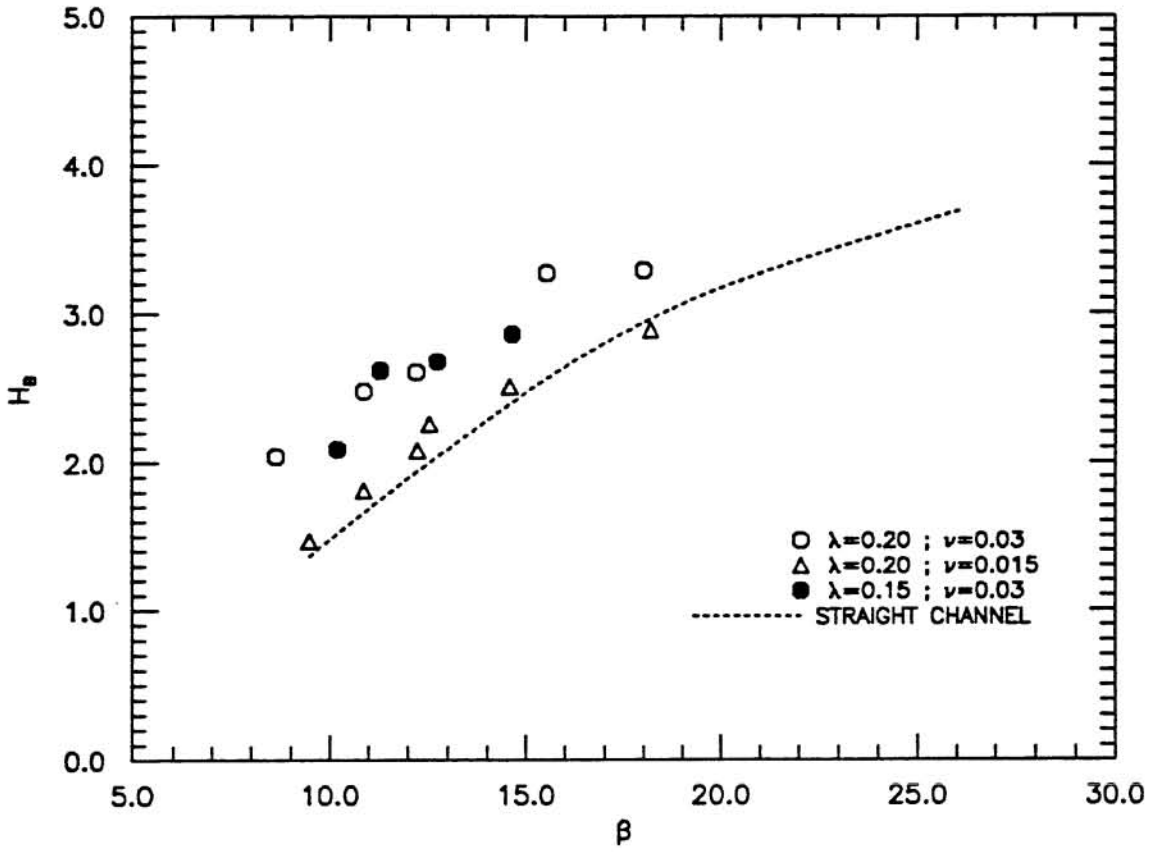

Fig. 6.12 Experimental Values of the Dimensionless Bar Height as a Function of β, λ_m and ν.

From Fig. 6.12, it is also apparent that the dimensionless bar height appears to increase with the dimensionless curvature of the channel, such that the experiments corresponding to $\nu = 0.03$ show larger bar heights than the experiments corresponding to $\nu = 0.015$, for the whole range of values of β and λ_m covered in the present study. A not so strong effect of the dimensionless wavenumber of the channel, λ_m, over the bar height is apparent from that figure for the experiments of equal curvature $\nu = 0.03$. However, a tendency exists for the values of the bar height corresponding to $\lambda_m = 0.20$ to be slightly larger than the values corresponding to $\lambda_m = 0.15$.

This latter conclusion is crucial from the point of view of the resonance phenomenon described in previous chapters. As it was already explained, the linear theory of resonance

predicts that the bed response to the forcing effect of the curvature has a maximum, which formally corresponds to an infinite peak, for a dimensionless wavenumber λ_m in the range 0.10 to 0.15. However, it is pointed out by Colombini et al. (1990) that a nonlinear analysis of this phenomenon developed by Professor's Seminara group in Italy, showed that the bed response in this case, rather than exhibiting a sharp peak within the resonance range, is found to follow a smoother trend, which still exhibits a maximum for values of λ_m that are typically larger than those predicted by the linear theory. The results presented in Fig. 6.12 appear to support this conclusion, in that for the experiments with the same value $\nu = 0.03$, the bar heights associated with both wavenumbers, $\lambda_m = 0.15$ and 0.20, take similar values, which however tend to be slightly larger for $\lambda_m = 0.20$. Since only two different wavelengths of the meandering channel were tested in the present research, the experimental data do not allow to define more precisely whether the maximum bed response effectively occurs within the range of λ_m covered herein. Nevertheless, the experimental results of Colombini et al. (1990), which covered a wider range of values of λ_m, tend to indicate that such maximum occurs for values of the channel wavenumber in the range 0.20 to 0.25, for the experimental conditions covered therein.

In order to compare the present results in the meandering channels with those obtained by Colombini et al. (1990), Fig. 6.13 shows the experimental points of Fig. 6.12, plotted together with the results of Colombini et al. corresponding to the wavenumbers $\lambda_m = 0.15$ and 0.20. The latter results were obtained for a dimensionless curvature $\nu = 0.05$, a slope $S_0 = 0.006$ and a dimensionless sediment size $d_s' = 230.3$, and covered a range of Froude numbers very similar to that of the present experiments.

Even though both sets of data are not totally comparable because of the differences in the values of the slope and the dimensionless sediment size, the experimental points of Colombini et al. locate consistently above the experimental points corresponding to the present study, defining, as expected for a larger curvature of the channel, larger bar heights. As it can also be observed in Fig. 6.13, the experimental points of Colombini et al. corresponding to $\lambda_m = 0.20$ define larger bar heights than those corresponding to $\lambda_m = 0.15$, similarly to what is observed for the present experimental results. However, in the case of Colombini et al.'s experiments that tendency is more evident.

Next, an analysis of the bar height of migrating bars in meandering channels is made. With this goal, the results corresponding to the experiments in Channel 2 are considered, since in those experiments migrating bars were observed to develop for a wide range of values of β. In the preceding chapter the distinction was made between bars in phase, which are bars that at a given time are located at the channel curves, and bars not in phase, which are

bars that at a given time are located away from the channel curves. This distinction was made because as the bars continuously migrate downstream, their amplitude changes with time such that it reaches a maximum when the bar is located at the channel curve, and a minimum when it is away from the curve. The experimental values of the bar height associated with bars in phase and with bars not in phase obtained in the experiments of SERIES 21 are plotted as a function of β in Fig. 6.14.

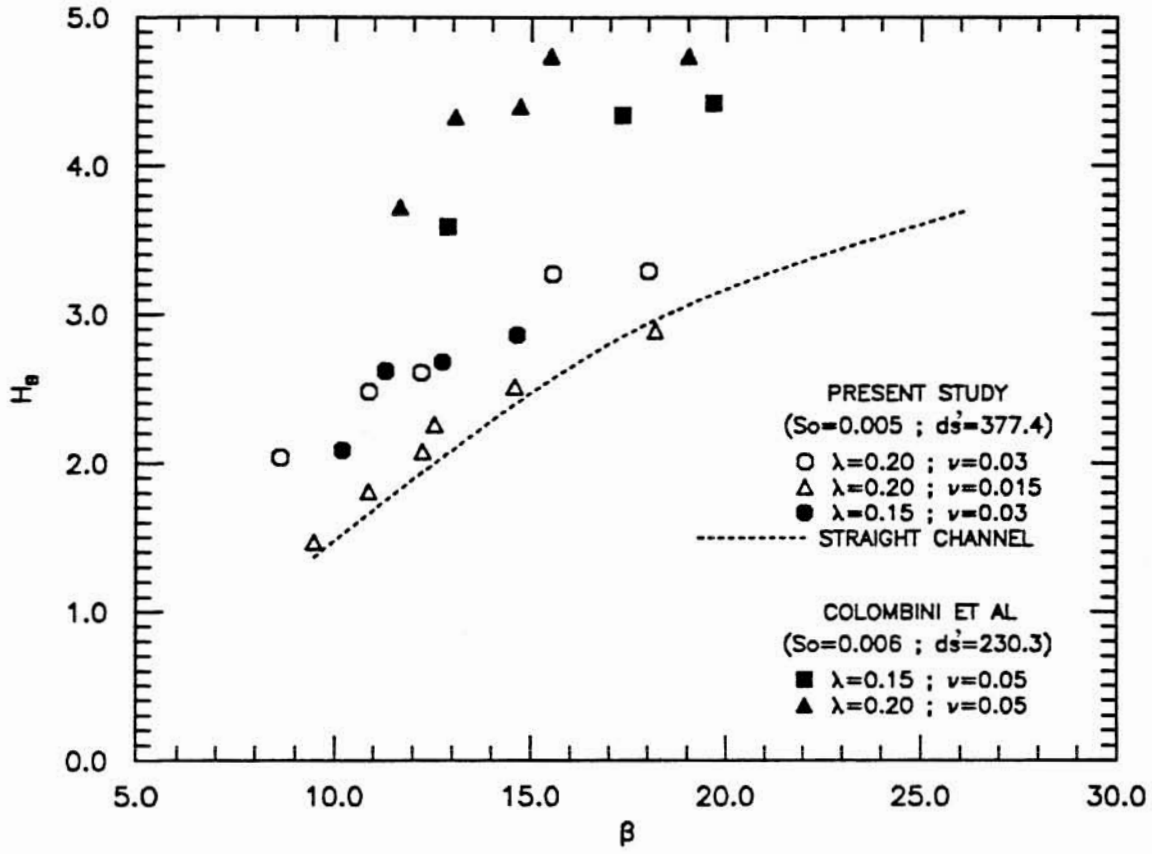

Fig. 6.13 H_B as a Function of β, λ_m and ν. Comparison Between the Experimental Results of Colombini et al. (1990) and the Present Study.

As it can be observed in Fig. 6.14, the height of bars not in phase with the channel curves tends to be lower than that of bars in phase, however the difference between those values appears to be a function of β, such that the difference increases as β increases. For a value of β of about 9.0, the height of bars not in phase is about 90% of the height of bars in phase, however for a value of β of about 18.0, such magnitude decreases to about 70%. A comparison with the curve fitted to the experimental results corresponding to the straight channel shows that while the heights of bars in phase are in general slightly larger than the values corresponding to the straight channel as it was already discussed, the heights of bars not in phase locate below that curve, which indicates that even though migrating bars develop

in the meandering channel, the curvature of the channel tends to damp them so their amplitude tends to be lower than the amplitude of the free migrating bars observed in the straight channel.

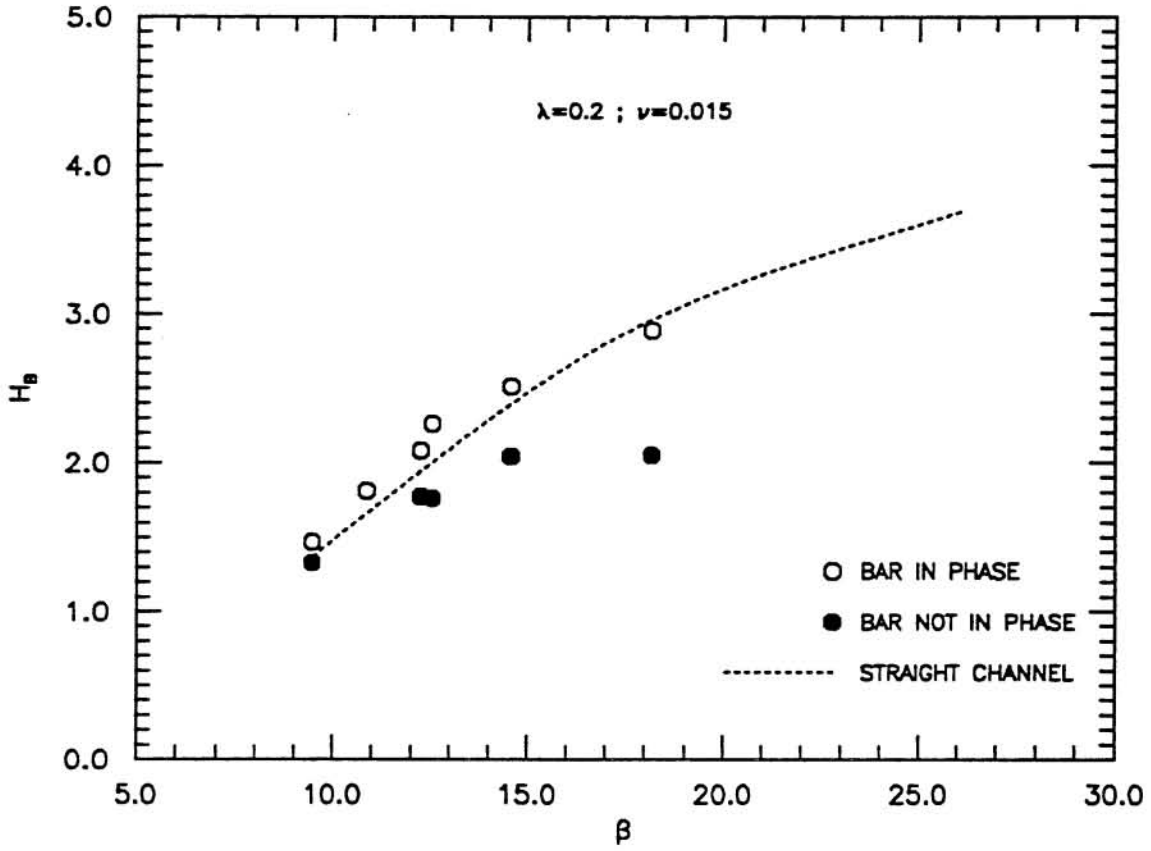

Fig. 6.14 Experimental Values of the Dimensionless Bar Height of Migrating Bars. Experiments in Channel 2.

This conclusion is in agreement with the theoretical analysis made by Tubino and Seminara (1990), which predicts that even though migrating bars are likely to develop in a meandering channel configuration, their amplitude is damped and their celerity is slowed down in magnitudes that depend on the values of β, θ and d_s (or alternatively S_0 and d_s') and the geometry of the channel, and eventually, depending on the values of those parameters, they can be totally suppressed. From Fig. 6.14 only the effect of β can be analyzed, however it is apparent that more damping of the amplitude of the migrating bars occurs as β increases.

Finally, a comparison is made between the present experimental results and the results obtained through the application of the numerical model developed in Chapter 4. With this aim, Fig. 6.15 presents the dimensionless bar heights corresponding to the experiments in Channel 1, SERIES 11, plotted as a function of β, together with the

corresponding numerical results obtained for the same conditions as those imposed in the laboratory experiments.

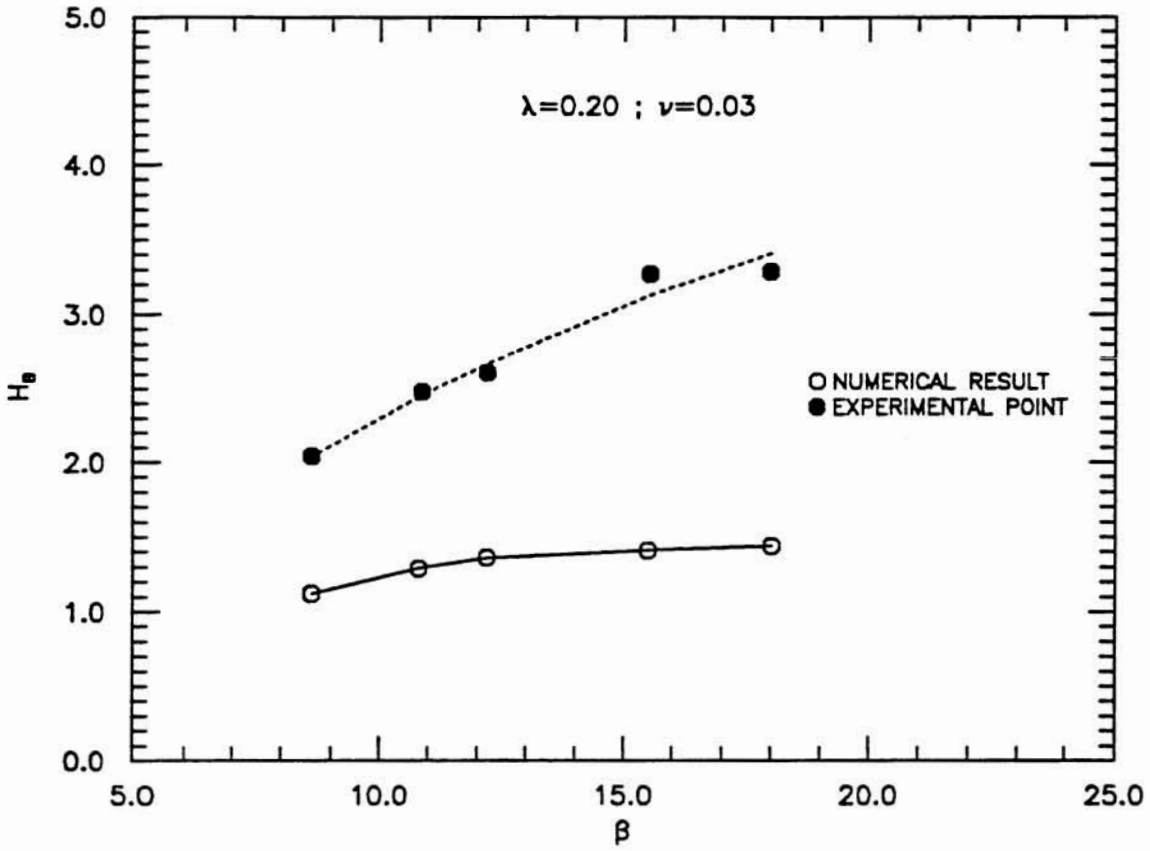

Fig. 6.15 Comparison Between Numerical and Experimental Results for the Dimensionless Bar Height as a Function of β in Meandering Channels.

As it can be seen in Fig.6. 15, the numerical results for the bar height define a curve along which H_B increases as β increases, at least within the covered range of values of this parameter. This trend is in agreement with the corresponding experimental results, however it is evident from Fig. 6.15 that the numerical model tends to underestimate in about 50% the observed amplitude of the bed deformation. Although there are simple ways to improve the numerical results presented in Fig. 6.15, for example by means of an adequate calibration of parameters, such as r in equation (4.11), for which a fixed value of 0.3 was assumed, it is apparent from the general characteristics of the bed deformation predicted by the numerical model, that a better modeling of this phenomenon requires an improvement in the modeling of the direction and magnitude of the sediment transport in the meandering channel. In particular, one of the main shortcomings of the model utilized herein is that it predicts a very symmetric deformation in the transverse direction (Fig. 4.12), which is in clear disagreement

with the observations made in the present study. For instance, it will be shown next that the maximum scour defined by the observed point bars is about 75% of the total bar height, whereas the numerical model predicts a value of 50% for this relation. This kind of features cannot be modified by simply varying the parameters of the model, requiring a review of the conceptual model used for sediment transport in the meandering channel.

6.3.2 Scour. In order to analyze the behavior of the scour generated by the bars observed in the meandering channels as compared with the bar height, Fig. 6.16 presents a plot of S as a function of H_B. The values of the scour presented therein correspond only to fixed bars or bars that are in phase with the channel curves in the case of migrating bars. In that figure a straight line with a slope of 0.75 is also plotted, in order to make a comparison with the results in the straight channel which were found to be well represented by such relationship.

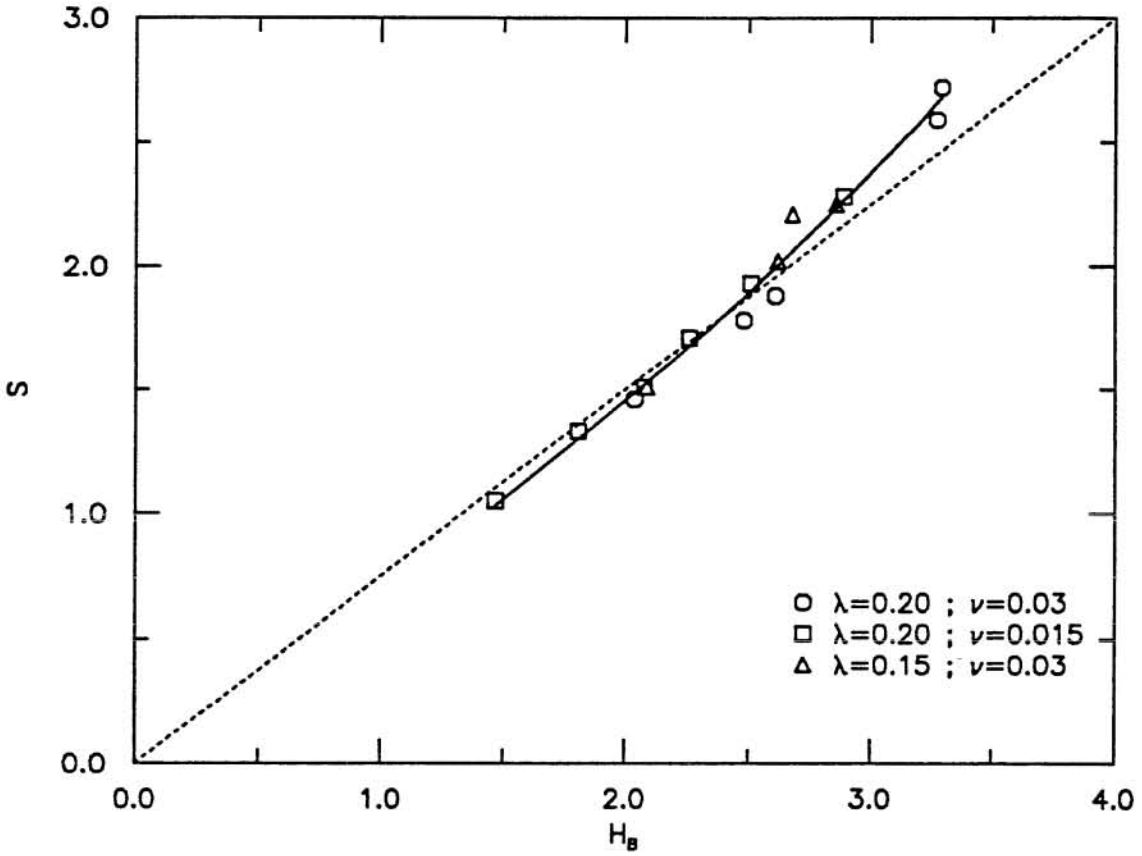

Fig. 6.16 Dimensionless Scour as a Function of the Dimensionless Bar Height.

Fig. 6.16 shows that although the experimental points are located around the straight line of slope 0.75, they tend to define a different trend, which appears to be nonlinear, such that the ratio S/H_B takes values that are larger than 0.75 for values of H_B larger than about 2.5, and slightly lower than 0.75 for values of H_B less than 2.5. This behavior seems to indicate

that as the bed scour increases, for example because of increasing β or increasing channel curvature, its effect tends to be more local, thus defining a slightly flatter bed than in the case of alternate bars in the straight channel. Since the area of the bed affected by scour decreases, the mean level of the bed tends to increase, such that because of the definition of the magnitude S, it increases its relative contribution to the magnitude of the total bar height.

6.3.3 Phase Lag of Fixed Bars. Next, an analysis of the dimensionless parameter δ, defined as the lag between the zone of maximum bed scour and the apex of the channel curves, is presented. Obviously this analysis is valid only for fixed bars, since for migrating bars no steady-state definition of δ is possible. Fig. 6.17 shows the experimental values of δ corresponding to the experiments in Channels 1 and 3, SERIES 11, 12 and 31, plotted as a function of β.

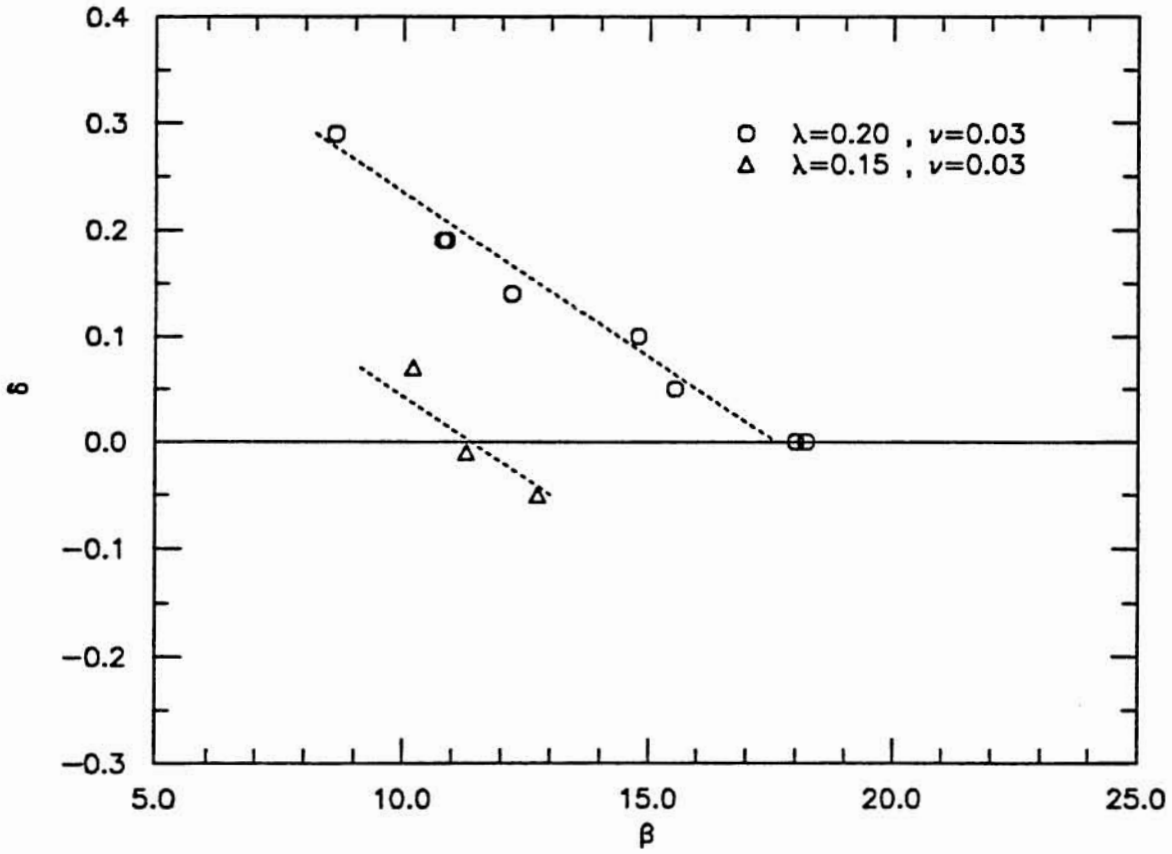

Fig. 6.17 Experimental Values of the Dimensionless Lag δ as a Function of β.

As it can be observed in Fig. 6.17, a linear relationship fits reasonably well the data corresponding to $\lambda_m = 0.20$, which appears to have a negative slope, indicating that δ tends to decrease as β increases. Only three points associated with fixed bars are available for the

wavenumber $\lambda_m = 0.15$, therefore it is not possible to define accurately the trend exhibited by that data. However, a straight line of slope similar to that of the points corresponding to $\lambda_m = 0.20$ seems to fit the data reasonably well. From those fittings it is clear that as the wavenumber of the channel decreases, i.e. as its wavelength increases, the dimensionless lag δ tends to decrease, for constant values of β and ν. It is also apparent from the results plotted in Fig. 6.17 corresponding to $\lambda_m = 0.15$, that for values of β larger than about 11.0, δ takes negative values, which means that the zone of maximum scour is located upstream of the curve apex. This behavior can also be deduced from the tendency exhibited by the data corresponding to $\lambda_m = 0.20$, which allows to expect negative values of δ for values of β larger than about 19.0.

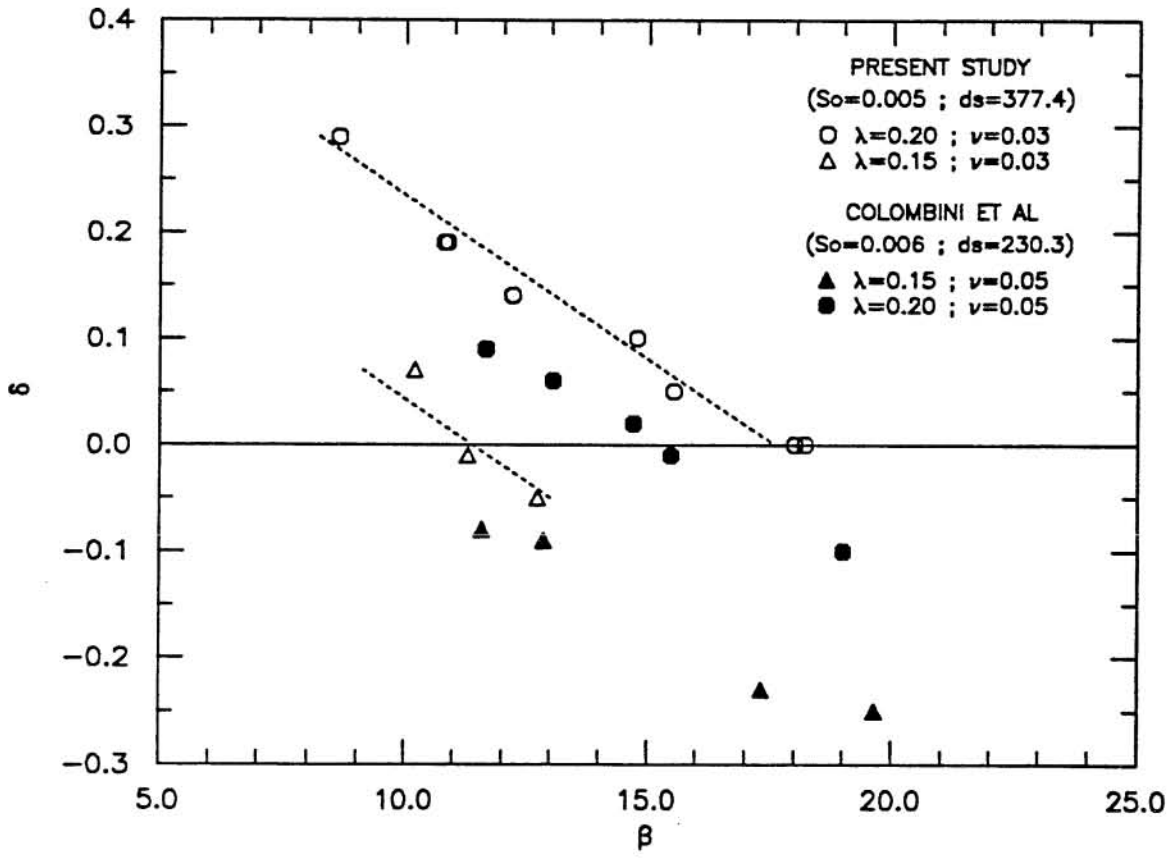

Fig. 6.18 δ as a Function of β, λ_m and ν. Comparison Between the Experimental Results of Colombini et al. (1990) and the Present Study.

Fig. 6.18 presents a comparison between the results for δ obtained herein, which correspond to a channel curvature $\nu = 0.03$, with the results of Colombini et al. (1990) for $\lambda_m = 0.15$ and 0.20, which correspond to a channel curvature $\nu = 0.05$. Although both sets of data are not totally comparable because of their differences in S_0 and d_s', as it was already

explained, a relatively good agreement in the tendencies exhibited by them is apparent from that figure. As it can be observed therein, the data corresponding to $\nu = 0.05$ show lower values of δ than those corresponding to $\nu = 0.03$, which indicates that as the curvature increases it forces a faster response of the flow, such that less lag exists between the zone of maximum velocity and bedload transport (i.e. zone of maximum scour) and the apex of the curve, than in the case of less curvature.

Finally, the results of Colombini et al. showed that negative values of δ are effectively possible. According to the results presented in Fig. 6.18, those negative values tend to occur either for large values of β or small values of λ_m, i.e. for large wavelengths of the meandering channels.

6.3.4 Wavelength of Migrating Bars. Fig. 6.19 presents the experimental values of the dimensionless wavelength of the observed migrating bars in the meandering channels. These correspond to the experiments made in Channel 2, SERIES 21, in which migrating bars were observed to develop for a wide range of values of β. No analysis is made herein of the wavelength of fixed bars, such as those observed in the rest of the experiments in the meandering channels, because in those cases the bar wavelength clearly coincides with the wavelength of the channel. In order to compare the wavelengths of the observed migrating bars, which correspond to a channel slope of 0.005, with those obtained in the straight channel, Fig. 6.19 also presents the data of the experiments of SERIES 01 and 02, which correspond to channel slopes of 0.0056 and 0.0044 respectively.

Although the wavelength data of migrating bars in the meandering channel exhibit more scatter than the corresponding straight channel data, interesting conclusions can be derived from Fig. 6.19. In the first place, it is observed therein that the wavelength of migrating bars in the meandering channel tends to be larger than the wavelength of the bars in the straight channel, but at the same time smaller than the wavelength of the meandering channel. In the second place, a strong influence of β on the dimensionless wavelength of the migrating bars in the meandering channel is apparent, such that for values of β of about 10, their wavelength is close to the wavelength of the channel, whereas for values of β of about 20 the wavelength of such bars is closer to the wavelength of the bars observed in the straight channel.

Therefore, from above discussion it is clear that even though migrating bars can develop in a meandering channel, the curvature of the channel tends to force a response that exhibits longer wavelengths than those corresponding to free bars in straight channels. The fact that the wavelength of the bed response decreases with β, seems to indicate that the effect of the curvature on the wavelength tends to be less strong as β increases, such that the

wavelength tends to be closer to that of the free bars in the straight channel. This behavior, however, appears to be opposite to that observed for the damping of the bar heights of the same bars, which is more drastic for large values of β.

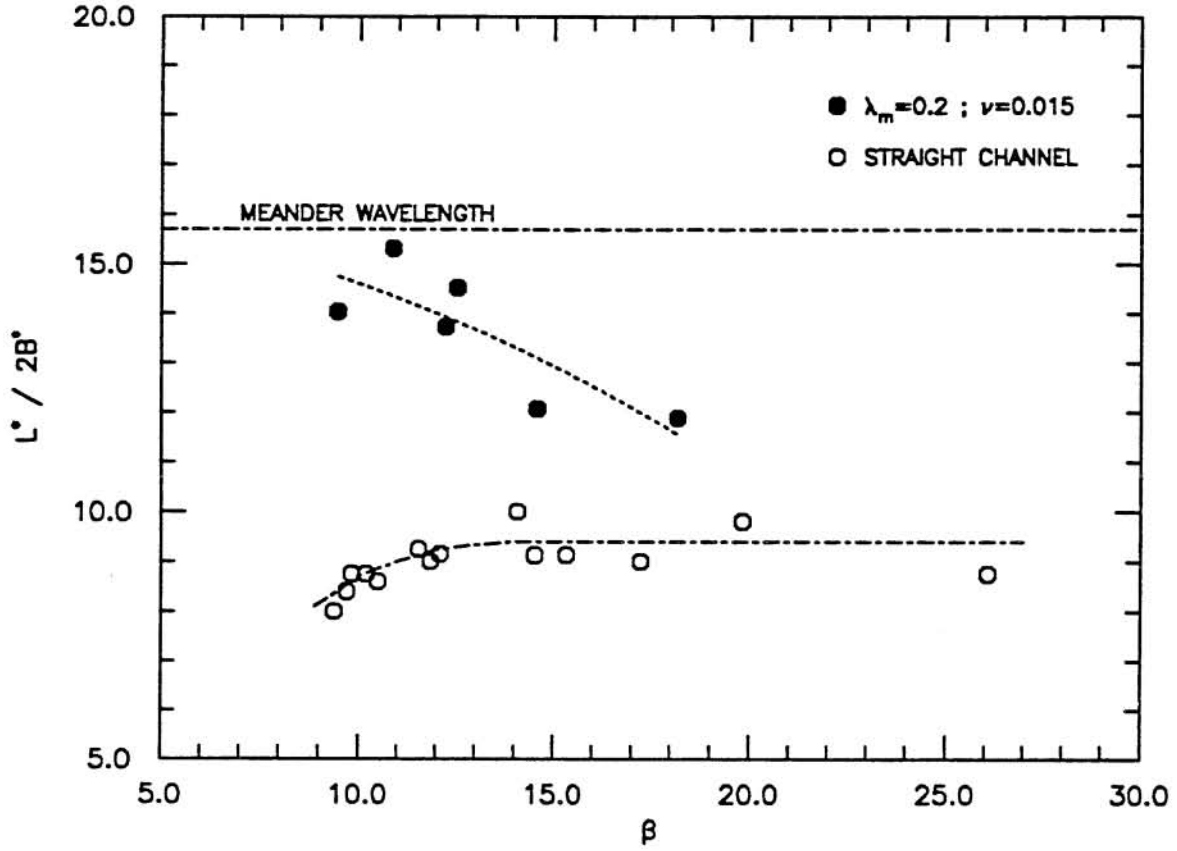

Fig. 6.19 Experimental Values of the Wavelength of Migrating Bars in Meandering Channels.

6.3.5 Celerity of Migrating Bars. In what follows, an analysis of the speed of the migrating bars observed in the meandering channels is presented. With this aim, the celerity of the migrating bars observed in Channel 2, SERIES 21, corresponding to the same experiments analyzed for the wavelength in the preceding section, is plotted as a function of β in Fig. 6.20. This figure also shows the celerity data corresponding to the experiments made in the straight channel, SERIES 01 and 02, in order to allow for a comparison between both sets of data.

As it can be observed therein, the celerity of the migrating bars in the meandering channel is smaller than that of the free bars in the straight channel, having in general, values that are lower than 0.05% of the mean flow velocity. A curve was fitted to the data corresponding to the bars in the meandering channels in order to analyze the general tendency exhibited by them and to compare it with that of the bars in the straight channel.

That curve has a negative slope very similar to that of the bars in the straight channel, showing decreasing dimensionless celerity for increasing β, and is located below the latter in an approximately constant magnitude equivalent to about 0.0003. For a value of β of about 18.0, the migration speed of the bars in the meandering channels is much less than 0.01% of the mean flow velocity, indicating a very slow migration of the bedforms, which is equivalent to less than 10% of the corresponding bar celerity in the straight channel.

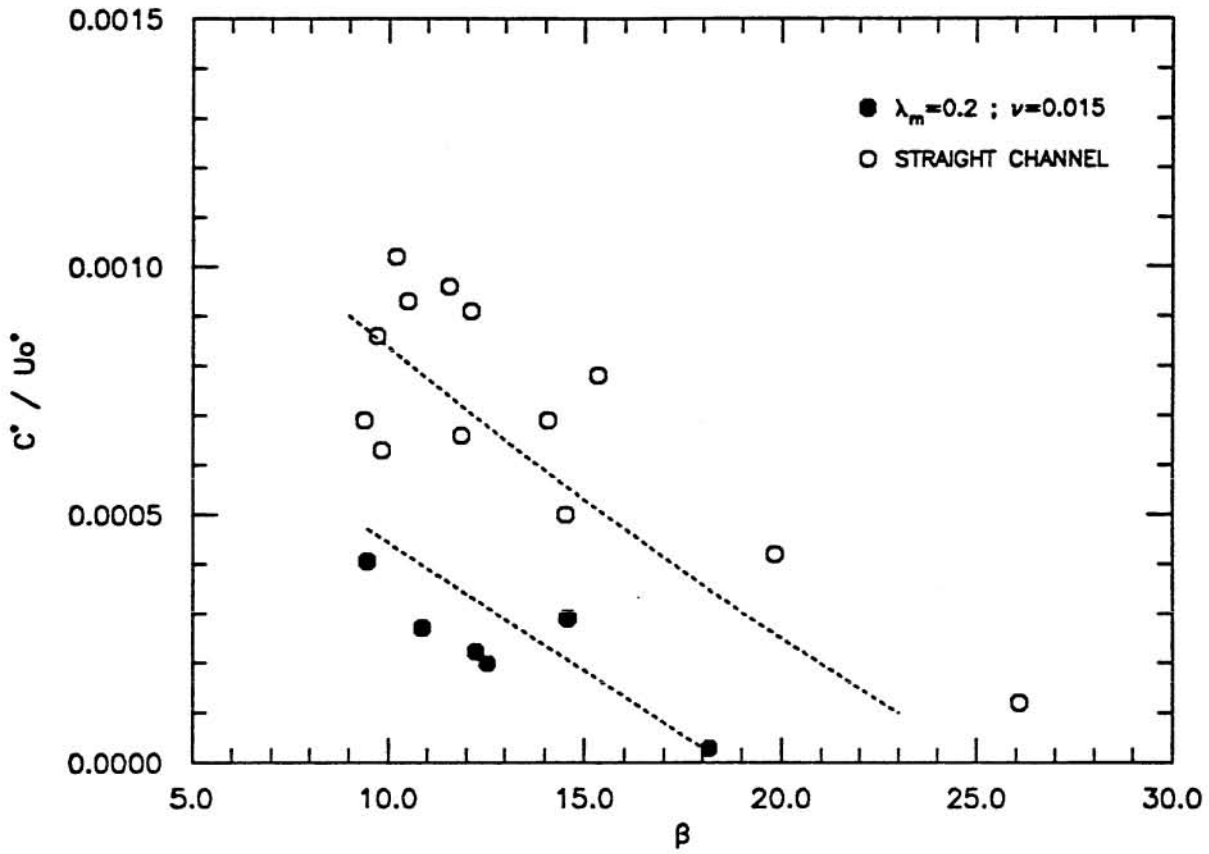

Fig. 6.20 Experimental Values of the Celerity of Migrating Bars in Meandering Channels.

From the above discussion it can be concluded that the curvature of the channels tends to slow down the migrating bedforms developed in the meandering channel, forcing values of the migration speed that are typically smaller than those of the free bars observed in the straight channel.

Therefore, summarizing the results discussed above and in preceding sections, it can be concluded that even though migrating bedforms are likely to develop in meandering channels for adequate conditions, the curvature of the channel forces a bed response whose bar height and migration speed are smaller than the bar height and migration speed of the

free bars observed in the straight channel. Likewise, the resulting wavelength of the migrating bedforms appears to be longer than that of the free bars in the straight channel. This behavior of the migrating bars in the meandering channel demonstrates that in fact the curvature of the channel tends to damp and eventually suppress those bedforms, which is in agreement with the theoretical findings of Tubino and Seminara (1990) discussed in Chapter 2. These researchers provide theoretical conditions for the total suppression of the migrating bars, which depend on the values of the wavenumber and curvature of the channel and also on β. A comparison between the present experimental results and those theoretical conditions is made later in this chapter.

6.3.6 Resistance. In order to analyze the hydraulic resistance of the flow in the meandering channels, Fig. 6.21 presents a comparison between theoretical and experimental rating curves corresponding to the conditions of the experiments in Channels 1, 2 and 3, SERIES 11, 12, 21, and 31. The Engelund–Hansen resistance equation (3.5) was used for the computation of the theoretical rating curves, which as it was already explained, have two branches, corresponding to the flat bed and dune covered bed conditions respectively.

As it is observed therein, the flat bed theoretical curve tends to underestimate the observed resistance, predicting values of the flow depth that are in general lower than the corresponding experimental values. On the contrary, the dune covered bed curve tends to overestimate the resistance, predicting values of the flow depth that are in general larger than the observed values. This behavior is similar to that discussed before for the experiments in the straight channel. In this case, however the form resistance associated with the channel curvature has to be taken into account, being the total resistance to the flow a combination between grain resistance given by the bed sediment and form resistance which is due to channel curvature and bed deformation simultaneously.

From Fig. 6.21, it can be concluded that as the channel curvature increases for fixed wavelength the total resistance also increases, as expected, since the increase in the curvature has associated an increase in the form component of the total resistance. Similarly, as the channel wavelength increases, i.e. the wavenumber λ_m decreases, for fixed curvature, the total resistance decreases, also as expected, since an increase in the wavelength for fixed curvature has associated a decrease in the form component of resistance per unit length. It can also be concluded that in the case of Channel 3, having a longer wavelength, the observed resistance is only slightly larger than that predicted by the theoretical resistance equation for flat bed conditions, which seems to indicate that in meandering channels the form resistance due to the bed deformation is less important than the form resistance associated with the channel curvature. It is also apparent by comparing with the results obtained in the straight

channel, that the bed deformation in the meandering channels has less resistance associated with it than the alternate bars observed in the straight channels, which appears to be reasonable considering that the bars in the meandering channels have in general longer wavelengths and also, as it was discussed before, seem to be flatter than the alternate bars observed in the straight channel.

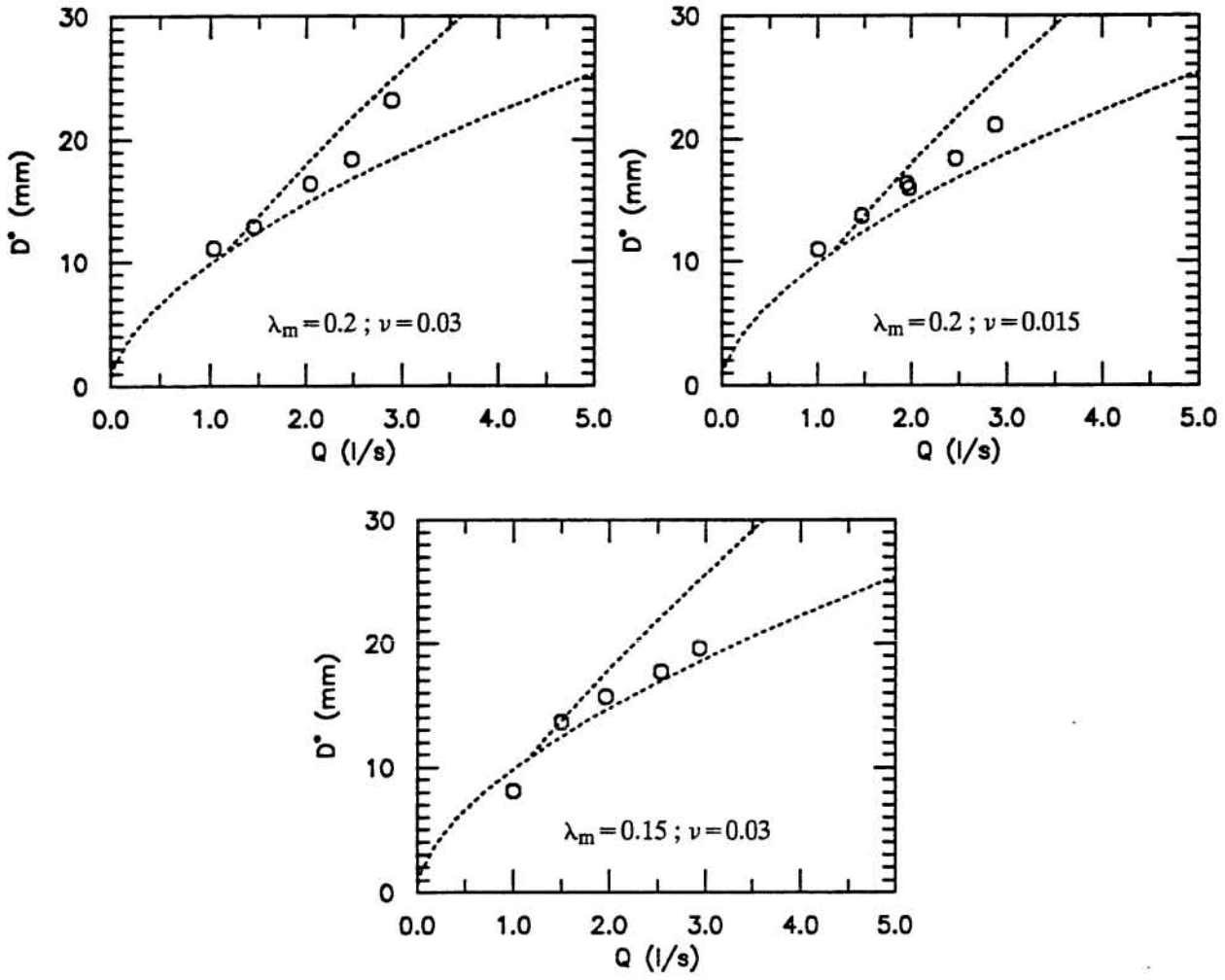

Fig. 6.21 Comparison Between Theoretical and Experimental Rating Curves.

6.3.6 Fourier Analysis of Bed Deformation. Next, a two-dimensional Fourier analysis of the bed deformation observed in the experiments in the meandering channels is performed. The analysis technique employed herein is the same as that explained in Section 6.2.6 for the Fourier analysis of the bed deformation in the straight channel.

As with the experiments in the straight channel, the results obtained from the Fourier analysis of the dimensionless bed deformation in the meandering channels indicates that only

a few harmonics in the axial and transverse directions have relevance in the Fourier characterization of the observed bars. The plot of the Fourier coefficients presented in Fig. 6.10 for the bars in the straight channel is also representative of the typical results obtained from the Fourier analysis of the bars in the meandering channels, which allows to conclude that also in this case the most important harmonics correspond to η_{11} and η_{02}.

With the aim of analyzing the effect of β and the channel geometry over the dimensionless bed deformation corresponding to one wavelength of the meandering channel, Fig. 6.22 shows the absolute value of the complex Fourier coefficients of harmonics η_{11}, η_{02}, η_{21} and η_{31}, plotted as a function of β, for Channels 1, 2 and 3, separately.

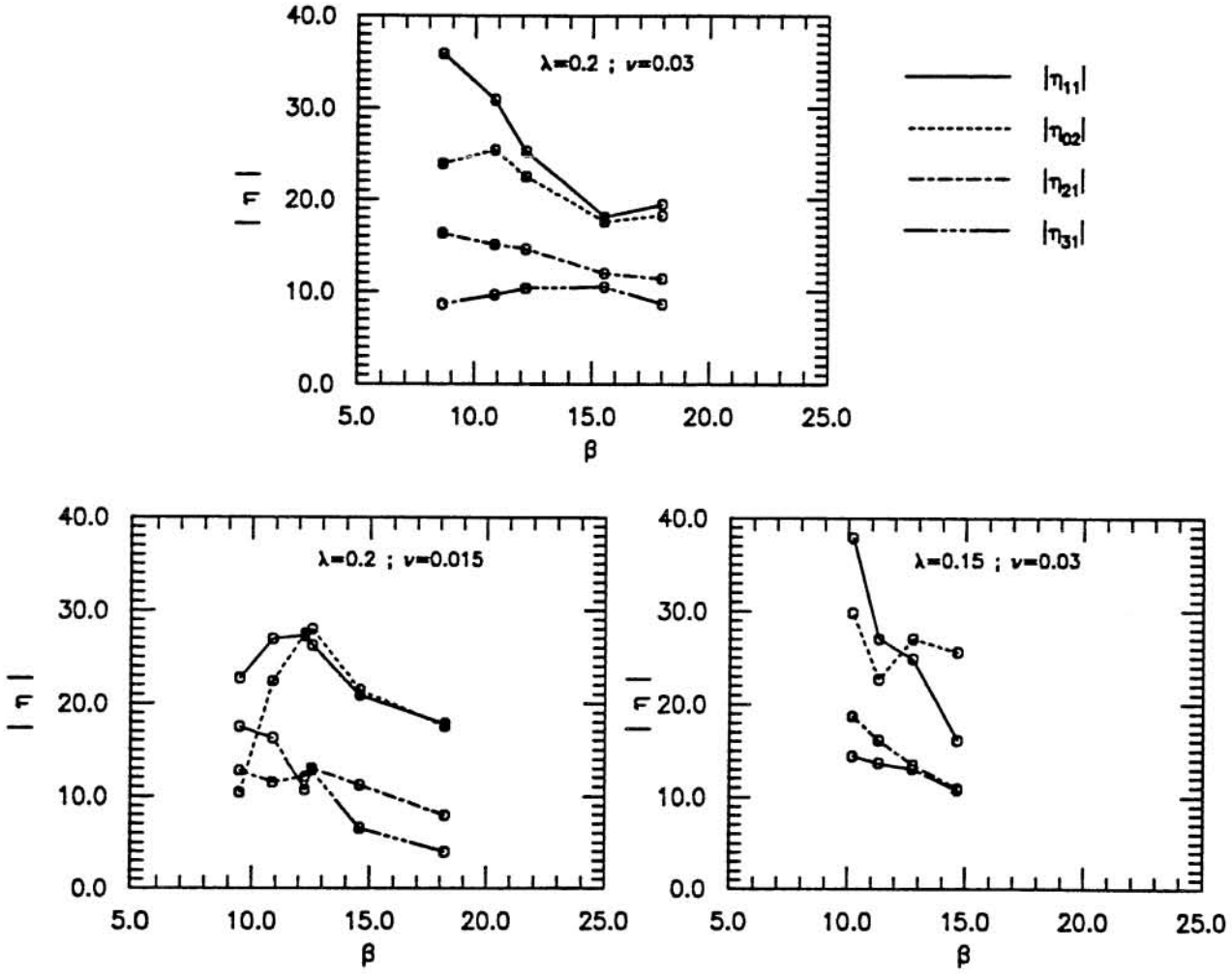

Fig. 6.22 Fourier Harmonics of Bed Deformation as a Function of β, λ_m and ν.

From Fig. 6.22 it can be concluded that in general terms the harmonics η_{11} and η_{02} are of comparable magnitude, which is of the order of twice the magnitude of the harmonics

η_{21} and η_{31}. From that figure it is also apparent that in general η_{11} and η_{02} tend to increase as β decreases, except in the case of $\lambda_m = 0.2$ and $\nu = 0.015$, for which a relatively sharp decrease occurs for values of β lower than about 12.0. The latter behavior was characteristic of the results for the experiments of equivalent slope in the straight channel, which indicates the existence of a similarity between the bars in the straight channel and those of the Channel 2 ($\lambda_m = 0.2$, $\nu = 0.015$). This is not unexpected, since in fact the bars in Channel 2 correspond to migrating bars, like the bars in the straight channel, which seems to indicate that this property is reflected in the geometric characteristics of the bed deformation.

As it can be observed in Fig. 6.22, the harmonics η_{21} and η_{31} also increase as β decreases, however, they show less variation with that parameter than η_{11} and η_{02}. Such variation, on the other hand, appears to be larger than that observed for the bars in the straight channel.

According to what is exposed above, it can be concluded that the dimensionless geometry of the bed deformation in meandering channels is a function of both the channel geometry, characterized by λ_m and ν, and β, which is reflected in the variation of its principal harmonics with those parameters, as it is observed in Fig. 6.22. It is also apparent from the above analysis that migrating bars, either in the straight or in the meandering channel, have geometric properties that are relatively different from those of the fixed bars in the meandering channels, manifested by the different behavior of the principal harmonics of the bed deformation observed in those cases, at least for values of β lower than about 12.0.

6.3.7 Critical Conditions for the Suppression of Migrating Bars. Next, an analysis of the critical conditions for the suppression of migrating bars in meandering channels derived from the present experimental results is made. With this aim, the theoretical predictive relationship proposed by Tubino and Seminara (1990), which was already discussed in Chapter 2, is employed. This relationship, derived from a weakly-nonlinear analysis that takes into account the interactions between migrating and fixed bars in a meandering channel, can be written in terms of a critical dimensionless curvature ν_c, such that the suppression of migrating bars is predicted to occur in a channel having a dimensionless curvature ν, if $\nu > \nu_c$, with ν_c given by:

$$\nu_c = k_{c1} \left(\frac{\beta - \beta_c}{\beta_c} \right)^{\frac{1}{2}} \qquad (6.8)$$

where β_c denotes the critical condition for the formation of alternate bars in a straight channel and k_{c1} represents a coefficient that is a function of the ratio between the meander wavelength and the critical wavelength of the alternate bars in the straight channel, and also of θ and d_s. This coefficient can be computed from Fig.9 of Tubino and Seminara's paper.

According to the experimental results presented in the preceding chapter, migrating bars were observed to occur in all the experiments in Channel 2 ($\lambda_m = 0.2$, $\nu = 0.015$), in one of the experiments in Channel 3 ($\lambda_m = 0.15$, $\nu = 0.03$), for instance, the one associated with the maximum experimental value of β of that series, and in none of the experiments in Channel 1 ($\lambda_m = 0.20$, $\nu = 0.03$). These results show that the conditions for the suppression of migrating bedforms appear to be a function of the geometry of the meandering channel, in this case represented by λ_m and ν, and also of β. In particular it is found that migrating bars are more likely to be suppressed as the curvature increases, the wavelength decreases or β decreases.

In order to compare these results with the theoretical prediction of Tubino and Seminara (1990), relation (6.8) is plotted as a function of β in Figs. 6.23 and 6.24, for values of the meander wavenumber corresponding to $\lambda_m = 0.20$ and 0.15 respectively. The values of k_{c1} employed to build the theoretical curves presented in those figures are shown in Table 6.3. Even though this parameter is a function of θ, and therefore should vary within the set of experiments corresponding to each meandering channel tested, only one value of k_{c1} is used herein for each meander wavenumber, since the experimental range of variation of θ is rather narrow and because Tubino and Seminara's paper gives information for the evaluation of this parameter only for a value of $\theta = 0.1$, which fortunately corresponds to a representative value of θ for the present experiments. In computing k_{c1}, a value of λ_c, the critical wavenumber for the formation of alternate bars in a straight channel, is needed. Herein, this parameter is computed from the theoretical curve presented in Fig. 3.6, using the calibrated values of θ and d_s associated with the experimental critical conditions for the formation of the alternate bars presented in Table 6.1.

Table 6.3 Values of k_{c1} for the Theoretical Critical Condition for the Suppression of Migrating Bars.

λ_m	$\lambda m / \lambda_c$	k_{c1}
0.20	0.45	0.06
0.15	0.33	0.05

Figs. 6.23 and 6.24 also present the experimental values of β associated with each channel curvature tested, such that white points denote experiments in which no migrating bars were observed and black points identify experiments in which migrating bars were observed to develop. As it can be observed in those figures, the theoretical curves do not appear to agree with the experimental results, predicting that in general the value of the critical curvature for the suppression of migrating bars is larger than the experimental values

of this parameter, and therefore, that migrating bars should have formed in all of the present experiments.

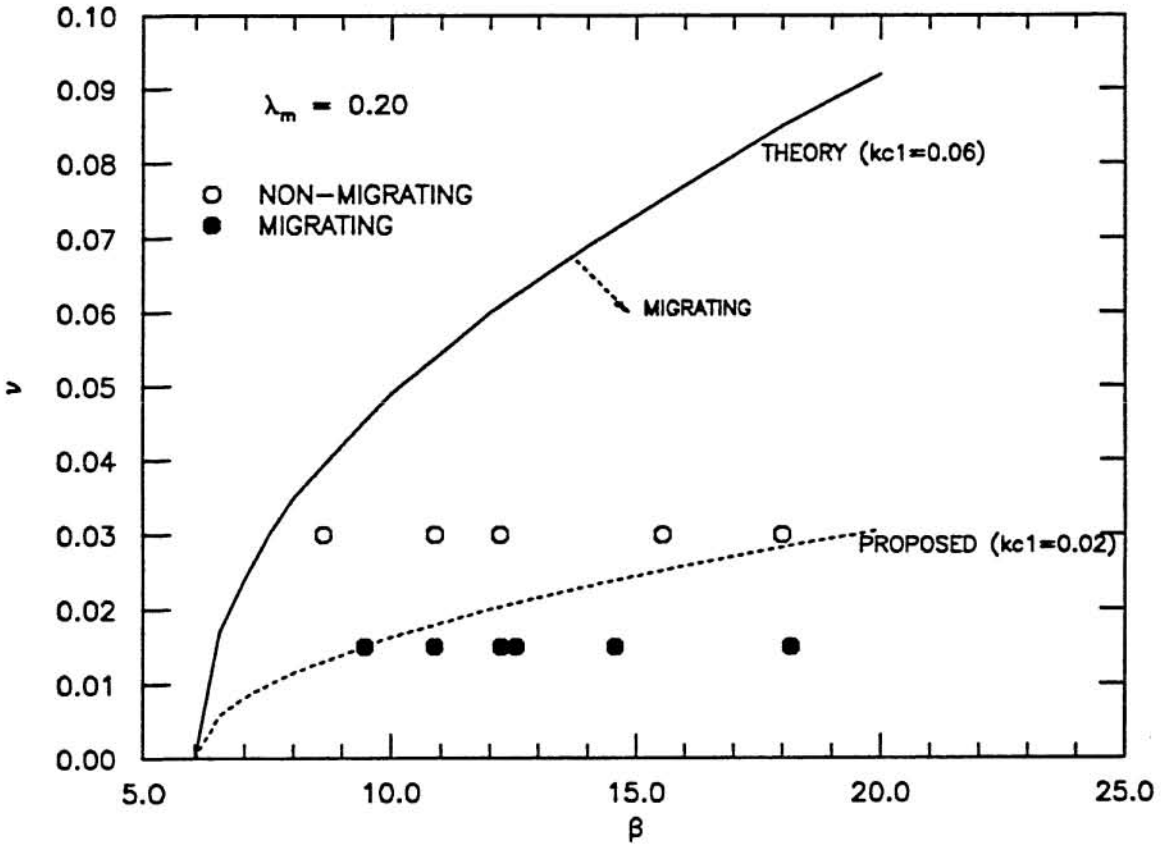

Fig. 6.23 Comparison Between Theoretical and Experimental Conditions for the Suppression of Migrating Bars in Meandering Channels ($\lambda_m = 0.20$).

With the aim of improving the theoretical prediction of the conditions for the suppression of migrating bars in meandering channels, a calibration of the values of k_{c1} is made, in order for the curves for ν_c given by (6.8) to be in agreement with the experimental results. The calibrated values are presented in Table 6.4.

Table 6.4 Calibrated Values of k_{c1} for the Critical Condition for the Suppression of Migrating Bars.

λ_m	k_{c1} THEORETICAL	k_{c1} CALIBRATED
0.20	0.06	0.020
0.15	0.05	0.025

As it can be observed in Table 6.4, the calibrated values of k_{c1} are of the order of 30 to 50% of the theoretical values. Besides, they appear to increase as the meander

wavenumber decreases, whereas the theoretical behavior is exactly the opposite. These differences between theoretical and calibrated parameters, however, are not totally unexpected, since as it happened before for the critical conditions for the formation of alternate bars, the theoretical values of parameters like k_{c1} may depend strongly on the resistance and bedload equations employed as closure relationships in the derivation of the theory, and therefore their validity depends on the validity of those closure relationships.

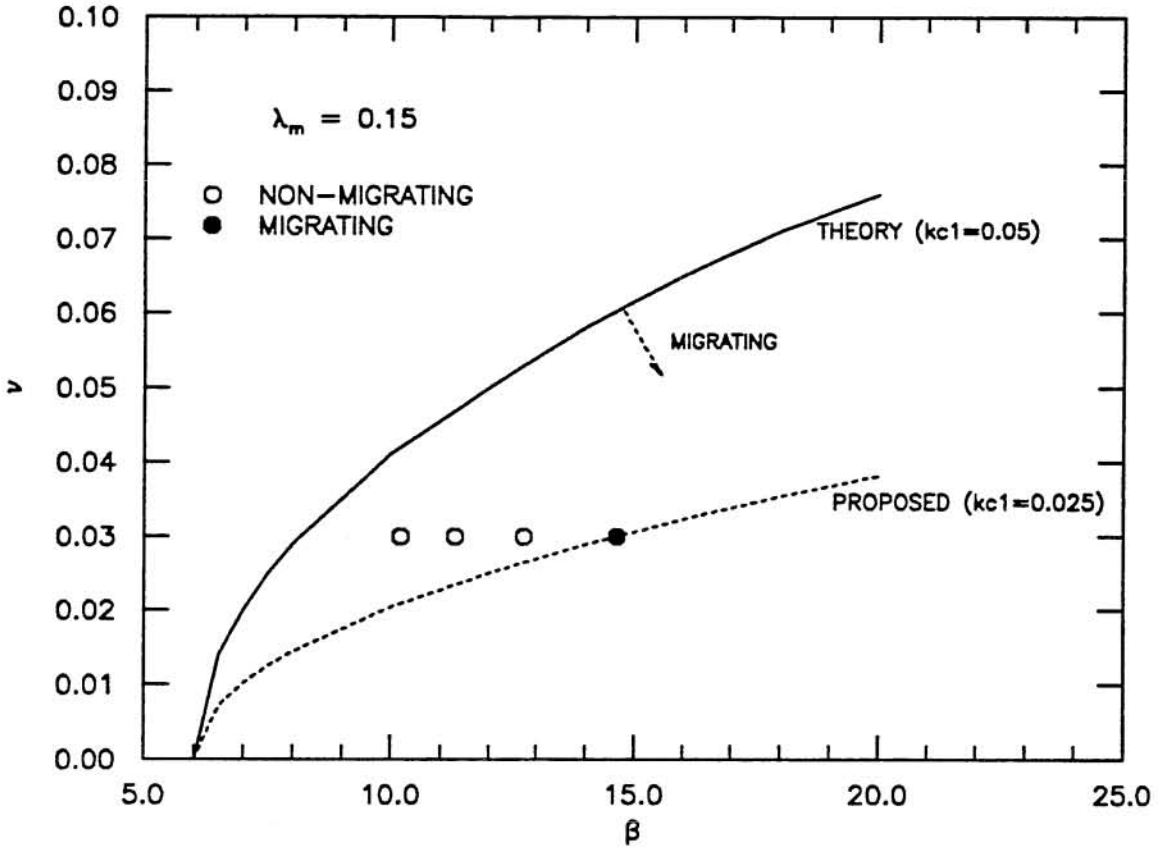

Fig. 6.24 Comparison Between Theoretical and Experimental Conditions for the Suppression of Migrating Bars in Meandering Channels ($\lambda_m = 0.15$).

The resultant curves for ν_c using the calibrated values of k_{c1} are also presented in Figs. 6.23 and 6.24. As it can be observed therein, they seem to predict the observed conditions for the suppression of bars relatively well which appears to validate, at least qualitatively, the theory developed by Tubino and Seminara (1990). Those curves show that the migrating bars tend to be suppressed for much smaller curvatures than those predicted by the original theory, however, the basic character of the theoretical solution appears to be well supported by the present experimental results.

7. CONCLUSIONS

The research work reported herein has covered some different aspects of the alternate bar and river meandering phenomena. The problem has been approached mainly from an experimental point of view, however, an analysis of the linear stability theory of alternate bars and a numerical model for the flow and bed deformation in meandering channels have also been developed, which provided a better insight on the physical meaning of the experimental observations.

As it is pointed out in Chapter 2, some recent analytical theories developed mainly by Professor Seminara's group in Italy and Professor Parker's group at the University of Minnesota, have contributed to attain a consistent level of understanding on the various phenomena involved in the initial process of meander formation. The main contributions to that understanding correspond to the so called 'resonance theory' of river meandering, developed by Blondeaux and Seminara (1985), a finite amplitude theory for alternate bars in straight channels developed by Colombini et al. (1987) and a theory that accounts for the interactions between free and forced bars in meandering channels, developed by Tubino and Seminara (1990). The study of Colombini et al. (1990) was the first attempt to validate the resonance theory through experiments, however, it did not cover some specific aspects of the theory, particularly, the phenomenon of coexistence of free and forced bars in meandering channels and the conditions for the suppression of the former, of which the only experimental precedent available in the literature corresponds to the study of Kinoshita and Miwa (1974). The experimental work reported herein was aimed as to provide experimental evidence to validate some aspects of the analytical models described above, specially those that had not been investigated in previous laboratory studies.

The analysis of the linear stability theory of Blondeaux and Seminara (1985) presented in Chapter 3, showed that the closure relationships for resistance and bedload employed in the analysis have an important influence in the results obtained for the critical conditions for the formation of alternate bars in straight channels. For instance, it was found that the use of the Engelund–Hansen bedload relationship instead of Meyer–Peter and Muller equation leads to a complete different behavior of the critical value of the parameter β. The critical value of the wavenumber λ, however, appeared to be less sensitive to the changes in the closure relationships. The linear stability theory, on the other hand, also allows to derive the resonance conditions for quasi–nonmigrating, quasi–nonamplifying bars. An analysis of those conditions showed that the wavelength of resonant bars appears to be on the order of two or three times larger than that of the bars in straight channels. A comparison with the

resonance conditions derived by Parker and Johannesson (1989), supported the above conclusion, although the resonance wavenumbers predicted by the simplified theory of the latter researchers are slightly larger than those obtained through the complete theory of Blondeaux and Seminara (1985).

A simplified numerical model for the two-dimensional flow and bed deformation in meandering channels was developed in Chapter 4. The model is based on one of the sets of governing equations commonly used in the literature. Although a limited analysis of the results given by the numerical model was made therein, it allowed to get some insight on the principal characteristics of the different physical processes involved in such phenomena. In fact, the model is capable of reproducing some of the main features of the bed deformation, as compared with the present experimental results, however, it appears to predict transversely symmetric bedforms which are not in agreement with experimental observations. Likewise, the numerical model appears to underestimate the experimental values of the bar height. As it is concluded in Chapter 4, it seems that the improvement of these features would require an improvement in the modeling of the magnitude and direction of sediment transport in meandering channels

The dimensional analysis made in Chapter 5, based on the non-dimensionalization of one of the commonly used sets of governing equations for the alternate bar and river meandering phenomena, showed that any parameter characterizing the bed deformation related to such phenomena should be a function of the sediment properties, the geometry of the channel, the slope, the Froude number and the parameter β, the latter characterizing the channel width to flow depth ratio. In particular it was found that once the sediment is selected, the bed deformation is a function mainly of the geometry and slope of the channel and β. It appears that the effect of the Froude number can be neglected, if it can be assumed that this parameter varies in a narrow range for a given set of experiments. The latter assumption seems to be valid for the present experiments, in which the Froude number varied in the range 0.70 to 0.85 approximately. A review of the conditions covered by the experiments of Colombini et al. (1990) and by those analyzed by Ikeda (1984) shows that, in general, the Froude numbers associated with the alternate bar phenomenon appear to be rather large, having values greater than about 0.70 in all cases observed.

A comparison made in Chapter 6 between the experimental data obtained in the straight channel with the empirical relationships of Ikeda (1984) for bar height and bar wavelength showed that the present data fall within the expected limits of scatter defined by Ikeda, suggesting that scale effects were negligible, and therefore the observations should be comparable to other sets of data obtained under similar conditions.

As it is concluded in Chapter 6 from the analysis of the experimental results obtained in the straight channel, two critical limits seem to exist for the parameter β, such that alternate bars do not develop for values of this parameter outside the range defined by those limits. The lower limit, associated with deeper flows, corresponds to the critical condition for the formation of bars, whereas the upper limit, associated with shallower flows, corresponds to the critical condition for sediment motion. It was found that the dimensionless bar height tends to increase as β increases over the lower limit, however it exhibits a sharp decrease as β gets closer to the upper limit. It was also found that the dimensionless bar height increases with the slope of the channel.

A comparison between these results and those predicted by the theory of Colombini et al. (1987) for calibrated values of β_c, showed that the theory works relatively well for values of the parameter $(\beta-\beta_c)/\beta_c$ lower than about 1.7, which gives the theory a wider range of validity than expected. The theory, however is unable to predict the sharp decrease in amplitude of the bars as β gets closer to the critical condition for the sediment motion. An analysis of the calibrated values of β_c showed that in general, they differ from the values predicted by the theoretical relationships derived in Chapter 3 for the critical conditions for the formation of alternate bars. It was found, however that the best predictions are given by the use of the Engelund–Hansen bedload equation and the flat bed Engelund–Hansen resistance relationship, although it seems that more resistance was present than that predicted by such relationship. The analysis of the experimental bedload rates and rating curves showed that, in fact, Engelund–Hansen bedload equation does much better than Meyer–Peter and Muller relation in predicting the observed bedload rates, and also that the alternate bar structure appears to induce more resistance than that predicted by the flat bed Engelund–Hansen resistance equation, which however is lower than that predicted by the dune covered bed Engelund–Hansen resistance equation.

As it is concluded from the results obtained in the experiments in the straight channel, a linear relationship appears to exist between the bar height and the maximum scour associated with the alternate bar structure, such that the latter seems to be about 75% of the former. This result is in agreement with the results analyzed by Ikeda (1984), who also found this value for the coefficient of proportionality.

From the analysis of the wavelength of the alternate bars observed in the straight channel it was concluded that while no clear effect of the slope of the channel on this parameter is apparent, the dimensionless wavelength appears to be a function of β, such that it tends to increase as β increases, approaching a constant value of about 9.4 for values of β larger than 1.5. A comparison between the experimental values of the wavelength and the

theoretical critical values of this parameter showed that, as the bar height, the wavelength seems also to increase from its critical value as β increases over the critical condition for the formation of alternate bars.

The analysis of the migration speed of the alternate bars observed in the straight channel showed that this parameter took, in general, values that are lower than 0.1% of the mean flow velocity. Even though the scattering of the experimental celerity data is larger than in the cases of the bar wavelength and bar height, a tendency appears to exist for the dimensionless bar celerity to decrease as β increases. On the contrary, no clear effect of the slope on the experimental values of this parameter is apparent.

As it was concluded from the two dimensional Fourier analysis of the dimensionless bed deformation observed in the experiments in the straight channel, the most important harmonics of the Fourier decomposition correspond to η_{11} and η_{02}, which denote the fundamental and a harmonic with no oscillation in the axial direction and with a transverse wavelength equivalent to the channel width, respectively. According with the analysis carried out, it was concluded that the dimensionless geometry of the bed deformation appears to be a function of both β and the channel slope, which is reflected in the variation of its principal harmonics η_{11} and η_{02}, with those parameters.

From the analysis of the bar heights observed in the experiments in the meandering channels corresponding to fixed bars or to bars in phase with the channel curvature in the case of migrating bars, it was concluded that the dimensionless values of this parameter appears to increase with the dimensionless curvature of the channel. On the other hand, a not so strong effect of the dimensionless wavenumber over the bar height is apparent. Nevertheless, for the results corresponding to the same curvature $\nu = 0.03$, a tendency seems to exist for the values of the bar height corresponding to $\lambda_m = 0.20$ to be slightly larger than the values corresponding to $\lambda_m = 0.15$. This appears to support the qualitative results predicted by a nonlinear theory of the resonance phenomenon, in that the response of the bed within the resonance range does not appear to present a sharp peak, but to follow a more smoothed trend. Whether a maximum of the bed response really exists for a certain wavenumber of the channel, however, cannot be answered from the present results because they correspond only to two different values of λ_m.

A comparison between these results, corresponding to the curvatures $\nu = 0.015$ and 0.030, and the dimensionless bar heights obtained by Colombini et al. (1990), corresponding to a curvature $\nu = 0.050$, showed that the experimental points of the latter researchers locate consistently above the experimental points corresponding to the present study, defining, as expected for a larger curvature of the channel, larger bar heights.

As it was concluded from the results obtained in the experiments in the meandering channels, the values of the maximum scour induced by the bed deformation appears to behave slightly different than the values of the scour associated with the bars in the straight channel. In fact, a nonlinear relationship seem to exist between the scour and the bar height, such their ratio takes values that are larger than 0.75 for values of the dimensionless bar height larger than about 2.5, and slightly lower than 0.75 for values of this parameter less than 2.5.

The analysis of the lag observed between the zone of maximum scour and the apex of the channel curves in the experiments in the meandering channels with fixed bars, showed that this parameter is a function of the channel wavelength and curvature, and also of the parameter β, such that the dimensionless value of the lag tends to decrease as β increases, the wavelength of the channel increases or the curvature of the channel increases. The latter conclusion, relating the behavior of the lag with the channel curvature, was obtained by means of a comparison with the experimental results of Colombini et al. (1990). The experimental results also showed that negative values of the lag, which indicates that the zone of maximum scour is located upstream the apex of the curve, are likely to occur either for large values of β or large wavelengths of the channel.

As it was described in Chapter 5, migrating bars were observed to develop in some of the present experiments in the meandering channels, in particular in all the experiments corresponding to $\lambda_m = 0.20$ and $\nu = 0.015$ and in one of the experiments corresponding to $\lambda_m = 0.15$ and $\nu = 0.03$. It was concluded from the analysis of those results that even though migrating bedforms are likely to develop in meandering channels for adequate conditions, the curvature of the channel appears to force a bed response whose bar height and migration speed are smaller than the bar height and migration speed of the free bars observed in the straight channel. Likewise, the resulting wavelength of the migrating bedforms appears to be longer than that of the free bars in the straight channel. This behavior demonstrates that in fact the curvature of the channel tends to damp, slow down and eventually suppress those bedforms, which is in agreement with the theoretical findings of Tubino and Seminara (1990).

From the comparison between theoretical and observed rating curves for the experiments in the meandering channels, it seems that in the meandering channels the form resistance due to the bed deformation is less important than the form resistance associated with the channel planform. According to this, it was found that more total resistance occurs for increasing curvature and decreasing wavelength of the channel, mainly because of the variation of the channel shape resistance with those parameters. It was also concluded that the bed deformation in the meandering channels has less resistance associated with it than

the alternate bars observed in the straight channels, which is mainly due to the longer wavelengths and flatter character of the former bedforms.

It was concluded from the two dimensional Fourier analysis of the dimensionless bed deformation observed in the meandering channels, that the most important harmonics of the Fourier decomposition correspond, as for the experiments in the straight channel, to η_{11} and η_{02}. According to the analysis carried on, it was also concluded that the dimensionless geometry of the bed deformation is a function of both the channel geometry and β, which is reflected in the variation of its principal harmonics with those parameters. It is also apparent from the analysis that migrating bars, either in the straight or in the meandering channel, have geometric properties that seem to be relatively different from those of the fixed bars in the meandering channels, which is manifested in the different behavior of the principal harmonics of the bed deformation observed in those cases.

Finally, the experimental results obtained in the meandering channels showed that the conditions for the suppression of migrating bedforms appear to be a function of the geometry of the meandering channel, characterized by λ_m and ν, and also of β. In particular it was found that migrating bars are more likely to be suppressed as the curvature increases, the wavelength decreases or β decreases. A comparison between the present results and the theoretical predictions for the suppression of migrating bars derived by Tubino and Seminara (1990), showed that the theory does not appear to agree with the experimental observations, in that it predicts that migrating bars should have been formed in all of the present experiments, which clearly did not occur. It was found that a calibration of the parameter k_{c1} in the theoretical condition for the suppression of migrating bars improved the theoretical prediction, showing that, at least for the present experiments, migrating bars tend to be suppressed for much smaller curvatures than those predicted by the original theory. This simple correction, however, seems to validate, at least qualitatively, the theory developed by Tubino and Seminara (1990), in that the basic character of the theoretical solution appears to be supported by the present experimental results.

REFERENCES

Anderson, A. G., Parker, G. and Wood, A. (1975). "The Flow and Stability Characteristics of Alluvial River Channels". *St. Anthony Falls Hydraulic Laboratory, University of Minnesota.* Project Report No. 161.

Blondeaux, P. and Seminara, G. (1985). "A Unified Bar–bend Theory of River Meanders". *Journal of Fluid Mechanics*, Vol. 157, pp. 449–470.

Callander, R. A. (1969). "Instability and River Channels". *Journal of Fluid Mechanics,* Vol. 36, pp. 465–480.

Colombini, M., Seminara, G. and Tubino, M. (1987). "Finite–amplitude Alternate Bars". *Journal of Fluid Mechanics,* Vol. 181, pp. 213–232.

Colombini, M., Tubino, M. and Whiting, P. (1990). "Topographic Expression of Bars in Meandering Channels". *Third International Workshop on Gravel–bed Rivers.* Florence, Italy.

Dietrich, W. and Whiting, P. (1989). "Boundary Shear Stress and Sediment Transport in River Meanders of Sand and Gravel". *River Meandering, Water Resources Monograph 12, American Geophysical Union.* Ch. 1 pp. 1–50.

Engelund, F. (1981). "The Motion of Sediment Particles on an Inclined Bed". *Tech. Univ. Denmark ISVA, Prog. Rep.* 53, pp. 15–20.

Engelund, F. and Skovgaard, O. (1973). "On the Origin of Meandering and Braiding in Alluvial Streams". *Journal of Fluid Mechanics,* Vol. 57, pp. 289–302.

Fredsøe, J. (1978). "Meandering and Braiding of Rivers". *Journal of Fluid Mechanics,* Vol. 84, pp. 609–624.

Fujita, Y. and Muramoto, Y. (1982). "Experimental Study on Stream Channel Processes in Alluvial Rivers". *Bulletin of the Disaster Prevention Research Institute, Kyoto University,* Vol. 32, pp. 49–96. Kyoto, Japan.

Fujita, Y. and Muramoto, Y. (1985). "Studies on the Process of Development of Alternate Bars". *Bulletin of the Disaster Prevention Research Institute, Kyoto University,* Vol. 35, pp. 55–86. Kyoto, Japan.

Gottlieb, L. (1976). "Three–dimensional Flow Pattern and Bed Topography in Meandering Channels". *ISVA Tech. Univ. Denmark Series Paper* 11.

Hansen, E. (1967). "On the Formation of Meanders as a Stability Problem". *Hydraul. Lab. Tech. Univ. Denmark Basic Res. Prog. Rep.* 13, pp. 9–13.

Hasewaga, K. (1981). "Research on an Equation of Bank Erosion Considering Non–equilibrium Conditions". *Proc. Japan Society of Civil Engineers,* Vol. 316 (12).

Hayashi, T. (1970). "Formation of Dunes and Antidunes in Open Channels". *Journal of Hydraulic Division, ASCE.* Vol 92 (HY2), pp. 357–366.

Hooke, R. (1975). "Distribution of Sediment Transport and Shear Stress in a Meander Bend". *Journal of Geology,* Vol. 83, pp. 543–565.

Ikeda, H. (1973). "A Study on the Formation of Sand Bars in an Experimental Flume". *Geographical Review of Japan,* Vol. 46, No. 7, pp. 435–450.

Ikeda, S. (1984). "Prediction of Alternate Bar Wavelength and Height". *Journal of Hydraulic Engineering,* Vol. 110, No. 4, pp. 371–386.

Ikeda, S. and Parker, G. eds. (1989). "River Meandering". *Water Resources Monograph 12, American geophysical Union.*

Ikeda, S., Parker, G. and Sawai, K. (1981). "Bend Theory of River Meanders. Part 1. Linear Development". *Journal of Fluid Mechanics,* Vol. 112, pp. 363–377.

Johannesson, H. and Parker, G. (1987). "Theory of River Meanders". *St. Anthony Falls Hydraulic Laboratory, University of Minnesota.* Project Report No. 278.

Johannesson, H. and Parker, G. (1989). "Linear Theory of River Meandering". *River Meandering, Water Resources Monograph 12, American Geophysical Union.* Ch. 7 pp. 181–213.

Kinoshita, R. (1957). "Formation of Dunes on River Bed". *Transactions, Japan Society of Civil Engineers,* No. 42, pp. 1–21.

Kinoshita, R. and Miwa, H. (1974). "River Channel Formation Which Prevents Downstream Translation of Transverse Bars". *Shinsabo,* Vol. 94, pp. 12–17. (In Japanese).

Kuroki, M. and Kishi, T. (1985). "Regime Criteria on Bars and Braids". *Hydraulic Papers, The Research Laboratory of Civil and Environmental Engineering, Hokkaido University.* Sapporo, Japan.

Langbein, W. B. and Leopold, L. B. (1966). "River Meanders – Theory of Minimum Variance". *USGS Professional Paper* 282B, pp. 1–85.

Nelson, J. and Smith, J. D. (1989). "Flow in Meandering Channels with Natural Topography". *River Meandering, Water Resources Monograph 12, American Geophysical Union.* Ch. 3, pp. 69–102.

Parker, G. (1976). "On the Cause and Characteristic Scales of Meandering and Braiding in Rivers". *Journal of Fluid Mechanics,* Vol. 76, pp. 457–480.

Parker, G. (1984). "Lateral Bed Load Transport on Side Slopes". *Journal of Hydraulic Engineering,* Vol. 110, pp. 197–199.

Parker, G. and Johannesson, H. (1989). "Observations on Several Recent Theories of Resonance and Overdeepening in Meandering Channels". *River Meandering, Water Resources Monograph 12, American Geophysical Union.* Ch. 12, pp. 379–415.

Patankar, S. V. (1980). "Numerical Heat Transfer and Fluid Flow". *Mc Graw–Hill, New York.*

Rozovskii, I.L. (1957). "Flow of Water in Bends of Open Channels". *Academy of Sciences of the Ukranian S.S.R.*

Seminara, G. and Tubino, M. (1989a). "Alternate Bars and Meandering: Free, Forced and Mixed Interactions". *River Meandering, Water Resources Monograph 12, American Geophysical Union.* Ch. 10, pp. 267–320.

Seminara, G. and Tubino, M. (1989b). "On the Process of Meander Formation". *Fourth International Symposium on River Sedimentation.* Beijing, China.

Shimizu, Y. and Itakura, T. (1989a). "Calculation of Bed Variation in Alluvial Channels". *Journal of Hydraulic Engineering,* Vol. 115, No. 3, pp. 367–384.

Shimizu, Y. and Itakura, T. (1989b). "River Design". *Report of the Civil Engineering Research Institute, Hokkaido Development Bureau.* Sapporo, Japan. (In Japanese).

Smith, J. D. and McLean, S. R. (1984). "A Model for Flow in Meandering Streams". *Water Resources Research,* Vol. 20, No. 9, pp. 1301–1315.

Struiksma, N., Olesen, K. W., Flokstra, C. and De Vriend, H. J. (1985). "Bed Deformations in Curved Alluvial Channels". *Journal of Hydraulic Research,* Vol. 23(1), pp. 57–79.

Sukekawa, N. (1971). "Study on Meandering of Streams in Straight Channels". *Rep. Bureau of Resources, Dept. Science and Technology,* Japan. pp. 335–363.

Tubino, M. (1991). "Growth of Alternate Bars in Unsteady Flow". *Water Resources Research,* Vol. 27, No. 1, pp. 37–52.

Tubino, M. and Seminara, G. (1990). "Free–forced Interactions in Developing Meanders and Suppression of Free Bars". *Journal of Fluid Mechanics*, Vol. 214, pp. 131–159.